CENTRO DE INVESTIGACIÓN Y DE ESTUDIOS AVANZADOS DEL INSTITUTO POLITÉCNICO NACIONAL

UNIDAD ZACATENCO
DEPARTAMENTO DE INGENERÍA ELÉCTRICA
SECCIÓN ELECTRÓNICA DEL ESTADO SÓLIDO

"Síntesis Mecanoquímica de $Cu(In,Ga)Se_2$: Depósito, Selenización y Caracterización de Películas"

Tesis

Que presenta

ROHINI NEENDOOR MOHAN

Para obtener el grado de

DOCTORA EN CIENCIAS

Director de la Tesis: Dr. Velumani Subramaniam

Ciudad de México Deciembre, 2016

RESUMEN

La calcopirita $Cu(In,Ga)Se_2$ (CIGSe) es un material fotovoltaico de película delgada favorable, y que ha ganado considerable atención debido a sus apropiadas propiedades opto-electrónicas y su alta eficiencia de conversión. Últimamente, ha alcanzado una eficiencia del 22,3%, que es la más alta entre las películas delgadas fotovoltaicas. A pesar de este logro, los procesos basados en vacío empleados para depositar la película de CIGSe en estos dispositivos, crean dificultades tecnológicas para la producción de módulos fotovoltaicos rentables. Como método de procesamiento económico, el método de deposición de película basado en partículas ganó aceptación en los últimos años. Esta estrategia incluye la síntesis de partículas de CIGSe, formulación de tinta con estas partículas, deposición de película por impresión, recubrimiento en pasta o recubrimiento por centrifugación y tratamientos térmicos posteriores a la deposición. Los diferentes enfoques desarrollados para la síntesis de partículas de CIGSe en los años anteriores se han basado principalmente en la síntesis química y solvotérmica. La aplicabilidad de estos métodos a escala industrial está limitada por el alto consumo de tiempo, el requerimiento de sofisticadas etapas de procesamiento y la dificultad para controlar la composición química de las partículas finales de CIGSe. Por el contrario, la síntesis mecanoquímica es una técnica rápida, barata, fácil de escalar que puede sintetizar partículas de aleación con una composición flexible a escala industrial. Por lo tanto, esta tesis presenta un estudio sobre la optimización de la síntesis mecanoquímica para obtener partículas de fase simple de CIGSe, deposición de la película y tratamientos térmicos posteriores a la deposición para lograr la recristalización y el crecimiento del grano.

La primera parte de esta tesis se dedica a: (i) optimizar las variables del proceso mecanoquímico, tales como tiempo de molienda, relación bola a polvillo y velocidad de molienda para sintetizar partículas de fase simple de calcopirita, $Cu(In,Ga)Se_2$ en tiempo de síntesis corto, (ii) formulación de la tinta a base de partículas de $Cu(In,Ga)Se_2$, (iii) deposición de película por la técnica de “Doctor Blade”, (iv) recocido en aire, y (v) recocido a alta temperatura en atmósfera de Se (selenización).

La optimización del proceso mecanoquímico se realizó para sintetizar partículas de $Cu(In_{0.5},Ga_{0.5})Se_2$. Se demostró que a un mayor tiempo de molienda, la relación de bolas a polvo y la velocidad de molienda eran favorables para la formación de partículas de fase simple de $Cu(In_{0,5},Ga_{0,5})Se_2$. Sin embargo, una relación más alta de bola a polvo ayudó a reducir el tiempo de molienda para formar partículas de fase simple de $Cu(In_{0,5},Ga_{0,5})Se_2$. El tamaño de cristal de las partículas sintetizadas varió linealmente con el tiempo de molienda, mientras que mostró una variación no lineal con respecto a la relación de bola a polvo y velocidad de molienda. Se encontró que la morfología de las partículas cambiaba con el tiempo de molienda, la relación de bola a polvo y la velocidad de molienda. Se determinó que los parámetros óptimos para sintetizar partículas de de $Cu(In_{0,5},Ga_{0,5})Se_2$ son: una relación de bola a polvo de 25:1, velocidad de molienda de 400 rpm y tiempo de molienda de 2 h. Además, las partículas de $Cu(In_{0.7},Ga_{0.3})Se_2$ se sintetizaron usando los parámetros optimizados de síntesis mecanoquímica, ya que la relación Ga/(In + Ga) = 0.3 fue la relación óptima utilizada en dispositivos fotovoltaicos de alta eficiencia basados en CIGSe.

La tinta a base de partículas $Cu(In_{0.7},Ga_{0.3})Se_2$ se formuló usando etanol como disolvente y una mezcla de Celulosa de Etilo y mezcla de Terpineol como aditivos orgánicos. Se estudió el papel de la Celulosa de Etilo y del Terpineol en la formulación de tinta y se entendió que la Celulosa de Etilo actuaba como aglutinante mientras que el Terpineol servía como agente dispersante. La película de $Cu(In_{0.7},Ga_{0.3})Se_2$ se depositó sobre el substrato de vidrio por medio de la técnica de Doctor Blade. Se encontró que, aunque la película de $Cu(In_{0.7},Ga_{0.3})Se_2$ depositada tenía una cantidad enorme de aditivos orgánicos, conservaba las propiedades estructurales de las partículas mecanicamente sintetizadas. A continuación, las películas se recocieron a 300 y 400 ˚C en aire durante 1 h para eliminar el contenido de Carbono y se selenizaron a 550 ˚C durante 15 minutos para mejorar las propiedades estructurales y morfológicas. El proceso de recocido y selenización mejoró la calidad cristalina y redujo los aditivos orgánicos en la película depositada. Las películas no mostraron crecimiento de grano incluso después de la selenización presumiblemente debido a la fuerte naturaleza covalente del compuesto CIGSe. La película recocida a 300 ˚C seguida de tratamiento de selenización mostró propiedades estructurales, compositivas y morfológicas superiores y reveló una concentración de portador de

10^{17} cm^{-3}, una movilidad de vacancias de 0.0368 cm^2/Vs y una resistividad de $3.06x10^2$ Ωcm. También exhibió fotoconductividad.

La segunda parte de esta tesis aborda una posible solución para superar la dificultad de obtener el crecimiento del grano durante la selenización de películas basadas en partículas mecánoquimicamente sintetizadas y así mejorar la movilidad y reducir la resistividad de las películas de CIGSe. Aquí presentamos la aparición de la recristalización y el crecimiento de grano en las películas CIGSe depositadas usando tinta basada en partículas sintetizadas de $Cu(In_{0.7},Ga_{0.3})Se_y$,(y = 1,5,1 y 0,5). Hasta donde sabemos, esta es la primera evidencia de recristalización y crecimiento de grano exhibido por las películas de CIGSe al reducir el contenido de Se en las partículas de $Cu(In_{0.7},Ga_{0.3})Se_y$ sintetizadas mecanoquímicamente. Aunque la película de CIGSe obtenida a partir de las partículas $Cu(In_{0.7},Ga_{0.3})Se_{0.5}$ mostró un pronunciado crecimiento de grano, también mostro presencia de una fase adicional de Cu-Se. Además, al reducir el contenido de Cu en las partículas de $Cu(In_{0.7},Ga_{0.3})Se_{O.5}$ sintetizadas mecanoquímicamente a 0.85, se obtuvieron películas de calcopirita de fase simple de $Cu_{0.85}(In_{0.7},Ga_{0.3})Se_2$ con crecimiento de grano mejorado, mayor movilidad, menor resistividad y fotoconductividad.

Finalmente, se exploraron películas CIGSe obtenidas por selenización de película $Cu_{0.85}(In_{0.7},Ga_{0.3})Se_{0.5}$ para aplicaciones fotovoltaicas. Se formó una heterojunción Mo/CIGSe/CdS/Au y exhibió características de diodo bajo la oscuridad. Sin embargo, la estructura de heterojunción no mostró ninguna corriente fotogenerada bajo iluminación, posiblemente debido a la alta resistencia en serie resultante de (i) falta de contacto frontal en capa i-ZnO/Al:ZnO, (ii) interfaces Mo/CIGSe y CIGSe/CdS, y (iv) calidad en la unión deficiente. Sin embargo, al completar la estructura del dispositivo Mo/CIGSe/CdS/i-ZnO/Al:ZnO y con investigaciones adicionales, se podría mejorar el rendimiento del dispositivo.

Palabras clave: sintesis mecanoquímica, peliculas de $Cu(In,Ga)Se_2$,recristalizacíon,crecimiento de grano.

ABSTRACT

Chalcopyrite $Cu(In,Ga)Se_2$ (CIGSe) is a favourable thin film photovoltaic material, and has attained considerable attention due to its appropriate opto-electronic properties and high conversion efficiency. Lately, it achieves efficiency of 22.3 % which is the highest among thin film photovoltaics. Despite this achievement, the vacuum-based processes employed for depositing CIGSe film in these devices creates technological difficulties for the production of cost-effective photovoltaic modules. As an economical processing approach, particle-based film deposition method gained acceptance in the past years. This strategy includes synthesis of CIGSe particles, particulate ink formulation, film deposition by printing, paste coating or spin coating and post-deposition heat treatments. Different approaches developed for synthesize of CIGSe particles in the previous years are mainly based on chemical and solvothermal synthesis. Applicability of these methods in industrial scale is limited by long time consumption,requirement of sophisticated processing steps and difficulty in controlling composition of final CIGSe particles. On the contrary, mechanochemical synthesis is a quick, inexpensive, easy-up scalable technique that can synthesize alloy particles with a flexible composition at an industrial scale. Hence this thesis presents a study on the optimization of mechanochemical synthesize to obtain single phase CIGSe particles, film deposition and post-deposition heat treatments to achieve recrystallization and grain growth.

The first part of this thesis is dedicated to (i) optimization of mechanochemical process variables such as milling time, ball to powder ratio and milling speed to synthesize single chalcopyrite phase $Cu(In,Ga)Se_2$ particles in short synthesis time, (ii) formulation of $Cu(In,Ga)Se_2$ particle-based ink, (iii) film deposition by doctor blade coating, (iv) air annealing, and (v) annealing at high temperature in Se atmosphere (selenization).

The optimization of the mechanochemical process was carried out to synthesize $Cu(In_{0.5},Ga_{0.5})Se_2$ particles. It showed that higher milling time, ball to powder ratio and milling speed were favourable for the formation of single phase $Cu(In_{0.5},Ga_{0.5})Se_2$ particles. However, higher ball to powder ratio assisted to reduce the milling time to form single phase $Cu(In_{0.5},Ga_{0.5})Se_2$ particles. The crystallite size of synthesized

particles varied linearly with milling time while it showed non -linear variation with respect to the ball to powder ratio and milling speed. Morphology of particles was found to change with milling time, ball to powder ratio and milling speed. The optimum parameter to synthesize $Cu(In_{0.5},Ga_{0.5})Se_2$ particles was determined to be a ball to powder ratio of 25:1, milling speed of 400 rpm and milling time of 2 h. Further, $Cu(In_{0.7},Ga_{0.3})Se_2$ particles were synthesized using the optimized mechanochemical synthesis parameters since Ga/(In+Ga) =0.3 was the optimum ratio used in high-efficiency CIGSe-based photovoltaic devices.

$Cu(In_{0.7},Ga_{0.3})Se_2$ particle-based ink was formulated using ethanol as solvent and Ethyl cellulose and Terpineol mixture as organic additives. The role of Ethyl cellulose and Terpineol in ink formulation was studied and understood that Ethyl cellulose acted as binder while Terpineol served as dispersing agent. $Cu(In_{0.7},Ga_{0.3})Se_2$ film was deposited on glass substrate by doctor blade coating of ink. It was found that even though as-deposited $Cu(In_{0.7},Ga_{0.3})Se_2$ film had a huge amount of organic additives, it preserved the structural properties of mechanochemically synthesized particles. Followingly, the films were annealed at 300 and 400 ˚C in air for 1 h to eliminate Carbon content and selenized at 550 ˚C for 15 minutes to improve the structural and morphological properties. Annealing and selenization process improved the crystalline quality and reduced the organic additives in the as-deposited film. Films did not exhibit grain growth even after selenization presumably due to strong covalent nature of CIGSe compound. The film annealed at 300 ˚C succeeded by selenization treatment showed superior structural, compositional and morphological properties and revealed carrier concentration of 10^{17} cm^{-3}, hole mobility of 0.0368 cm^2/Vs and resistivity of 3.06×10^2 Ωcm. Also, it exhibited photoconductivity.

The second part of this thesis addresses a possible solution to overcome the difficulty in obtaining grain growth during selenization of mechanochemically synthesized particle-based films and thus to improve the mobility and reduce the resistivity of CIGSe films. Here we presented the occurance of recrystallization and grain growth in CIGSe films deposited using mechanochemically synthesized $Cu(In_{0.7},Ga_{0.3})Se_y$ particles (y=1.5,1 and 0.5)- based ink. To the best of our knowledge, this is the first evidence of recrystallization and grain growth exhibited by CIGSe films upon reducing Se content in the mechanochemically synthesized $Cu(In_{0.7},Ga_{0.3})Se_y$ particles. Even

though the CIGSe film obtained from $Cu(In_{0.7},Ga_{0.3})Se_{0.5}$ particle exhibited pronounced grain growth, it showed presence of additional Cu-Se phase. Further, by reducing Cu content in the mechanochemically synthesized $Cu(In_{0.7},Ga_{0.3})Se_{0.5}$ particles to 0.85, single chalcopyrite phase $Cu_{0.85}(In_{0.7},Ga_{0.3})Se_2$ films with enhanced grain growth, higher mobility, less resistivity and photoconductivity was obtained.

Eventually, CIGSe films obtained by selenization of $Cu_{0.85}(In_{0.7},Ga_{0.3})Se_{0.5}$ film was explored for photovoltaic application. Mo/CIGSe/CdS/Au heterojunction was formed and it exhibited diode characteristics under dark. However, the heterojunction structure showed no photogenerated current under illumination possibly due to high series resistance arising from (i) lack of proper front contact made of i- ZnO/Al:ZnO window layer, (ii) Mo/CIGSe and CIGSe/CdS interfaces, and (iv) reduced junction quality. Nevertheless, by the completion of Mo/CIGSe/ CdS/ i-ZnO/Al:ZnO device structure and with further investigations, the device performance could be improved.

Keywords: Mechanochemical synthesis, $Cu(In,Ga)Se_2$ films, recrystallization and grain growth.

ACKNOWLEDGEMENT

Completion of this doctoral thesis was possible with the support of several people. I would like to express my sincere gratitude to all of them.

First, I am using this opportunity to express my gratitude to, my advisor, Dr. Velumani Subramaniam for his continuous support and motivation throughout the course of this thesis. I admire all his truthful and illuminating views which made my PhD experience productive.

I express my warm thanks to my thesis committee: Dr. Maria de La Luz Olvera, Dr. Ramón Peña Sierra, Dr. Arturo Alvarez Maldonado and Dr. José Chávez Carvayar for guiding me through all these years. Their insightful comments and encouragements helped me to improve my research work.

I would like to thank Dr. Osvaldo Vigil Galán who provided me the opportunity to work with his team and giving accessibility to use his laboratory facilities. I also thank Dr. Fabián Andrés Pulgarin Agudelo for helping and teaching me to do selenization process as well as chemical bath deposition of CdS during his busy post- doctoral period. Without their help, it would not be possible to complete this research work.

I would like to express my sincere thanks to Dr. Gabriel Romero-Paredes for always being available for clarifying doubts, Dr. Victor Sanchez Resendiz for always offering help in needy occasions, Dr. Alejandro Avila Garcia for teaching and allowing to handle I-V equipment, Dr. Mauricio Ortega Lopez and Dr. Arturo Morales Acevedo for always welcoming for discussing and clarifying my doubts regarding solar cells.

I would like to thank M.in C. Miguel Galván Arellano, M. inC. Adolfo Fuentes Tavira, Marcella Guerrero, J.E. Remero Ibarra, Ing. Miguel Angel Ibarra Avendaño, Ing. Miguel Angel Luna Arias, Ing. Angela Gabriela Lopez Fabian, Ing.Emma Julia Moon Arredondo, and Ing. Araceli Palafox Gomez for their assistance in characterization of samples. I would like to thank Norma Iris González García and Edmundo Rodriguez Ascención for their technical assistance. I would not be finishing this thesis work without all their timely help. I convey my sincere gratitude to Alvaro Guzmán Campuzano and Daniel Benito Ramirez Gonzalez for their comprehensive support

throughout these years. I would like to thank all the secretaries in SEES for their care and help.

My special thanks to Mr. Ivan who took initiative to repair selenization equipments so that my experiments were not delayed and to M.in C. Enrique Valencia Resendiz for helping to perform I-V characterization of p-n junctions. I would like to appreciate his patience and time spent by making plenty of measurements for each sample.

I would like to thank my seniors, especially Dr. Jagadeesh Babu Bellam who helped me from the very first time I arrived in Benito Juarez international airport, he introduced Mexico City, taught me the fundamentals of CIGSe and motivate me until his last day in our group. I also thank Dr. Venkatesan Rajalingam who stood as a friend and welcome me to clarify my doubts.

My sincere thanks to my lab mate and friend Pablo Reyes. He was at a call away to help me during these years. Working with Pablo was always being a wonderful experience. He always tried to share his knowledge whether it is experimental or theoretical. He always motivated, and consoled me when results were not coming as expected. He was always there to discuss the results. I can't even imagine how my work would be without the discussions I had with Pablo.

I thank my dear lab mates victor Israyelu, Latha Marasamy, Aruna devi chettiar, Ravi chandran and Dr. Goldie Oza for their co-operation. My time in Mexico was made pleasant with the company of my friends. I am grateful for the time spent with roommates Maribel Cayateno, Laura, Anais Mecott, Araceli Aldana, Karen, Kareena, Gayathri, Garbi, Tauqueer and Shadhai. I remember the Indian students in CINVESTAV who played the lead in making me feel like home. I am thanking Suresh T, Suresh gadi, Srinivas, Gurusami, Karthik, Ateet, Eshwar, Kalyan, Rasheedha, Selva, Vinoth, Gaurav, Siv, Kem, Neeshu, and Joyce.

Last but not the least; I would like to thank my family for all their love and encouragement. My parents who raised me with love of academics and supported me in all my decisions. My sisters and in-laws' who always stood with me to chase my dreams. I would like to express my special thanks to my life partner Mr. Prasanth Saseendran for faithful support throughout these years which kept me emotionally stable till the end of my research.

CONTENT

LIST OF TABLES

LIST OF FIGURES

CHAPTER - 1
INTRODUCTION

1.1. Importance of Renewable Energy

Energy is an integral part of economic and social development in all countries. The art of the efficient use of available energy enabled humans to enhance the quality of life. The history of the development of energy resources and evolution of energy conversion technologies have contributed towards the cultural advancement of human society. From the era of the industrial revolution (1760-1840), energy from fossil fuels is playing a profound role in nurturing human development.

The important fossil fuels used today by the most industrialized and developing nations are oil, coal and natural gas. This is because of the reasonably low price for converting fossil fuel to energy. Nevertheless, severe environmental issues are arising out of the use of fossil fuels in the current scenario. The main issue is that fossil fuel, a natural resource of energy, is limited and non-renewable. It underlines the impracticability of use of fossil fuel energy as if there is an unlimited amount for much longer time to meet the increasing energy demand. The outlook for energy published in 2015, describes significant variation in the energy demand trend across the world from 2010 to 2040, in relation to change in population and economic growth measured as GDP (the gross domestic product) of developed economies (as defined by the membership in the Organization for Economic Co-operation and Development, OECD), developing economies and rest of the world which is shown in figure 1.1. According to that, global population is projected to hike from 7 billion in 2010 to 9 billion by 2040 in which 40 % of rising is expected to come from India and the 10 key growth countries comprise of Brazil, Mexico, South Africa, Nigeria, Egypt, Turkey, Saudi Arabia, Iran, Thailand, and Indonesia. The increase in population in these countries can lead to its economic growth as the number of the working-age citizen to the total population increases. With an increase in population, the global GDP is expected to rise by 140% as result of economic growth in these countries. Per capita GDP of China, India, and other key growth countries is expected to be higher than 4 times, 3 times and 1-2 times

respectively, by 2040 than it is in 2010. It emphasizes on expected increase in standard of living of billions of people by 2040, which drive increased energy use in improved infrastructure, transportation, electrification, and urbanization. So, a huge increase in demand for energy from 400 to 700 quadrillion British thermal unit (QBTU) (1 QBTU/h= 293.071 $\times 10^3$ GW) from 2010 to 2040, is estimated in which fifty percentage of the rise in global energy demand is expected to be together from two developing economies, India and China and rest of share is presumed from the key growth countries [1.1].

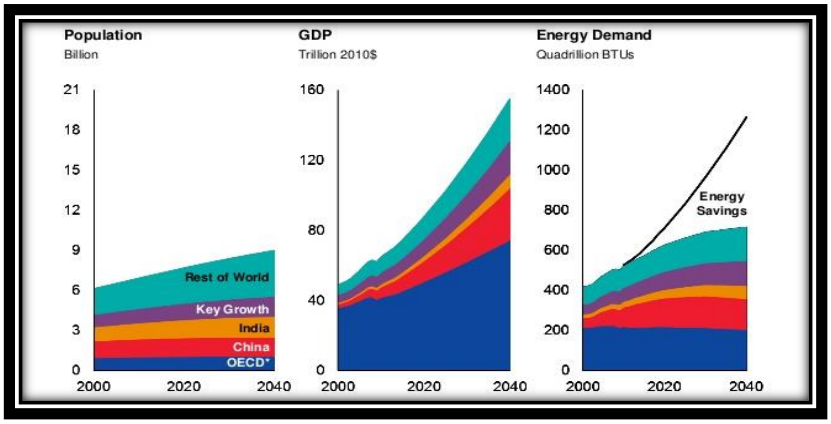

Fig.1.1. Expected increase in population, economy, and energy demand by 2040 [1.1].

The second most important issue is climate change due to global warming, one of the difficult challenges faced by the world in the 21st century [1.2]. Burning of fossil fuels causes emission of long-lived green - house gases (LLGHG) such as CO_2, SO_2 and NO_x, which act to trap heat, radiated from earth's surface and cause an increase in surface temperature of the earth. Observation of the World Meteorological Organization- Global Atmosphere Watch programme on LLGHG is given in table 1.1. It illustrates the atmospheric abundance (2013) and rate of change of most important LLGHG from the pre-industrialization era (1750) to 2012. It shows that CO_2 is the primary LLGHG that contributes 65% to radiative forcing (RF- it expresses a change of energy in the atmosphere due to GHG emissions). In 2013, the global average CO_2 level was 396 ppm, which is 142 % of the pre-industrial level. Besides, there is 2.07 ppm/yr of mean absolute increase in atmospheric CO_2 from 2003 to 2013. The lion's share of this is contributed by the combustion of fossil fuels for energy purposes [1.3].

Hence, the dependence on fossil fuels to meet the increased energy demand could have adverse effects on global climatic changes. In this context, promotion of alternative, environmentally friendly and renewable energy sources, which generate less or no carbon to the environment pay much attention as decarbonising energy is the quickest way to decarbonise the world.

Table 1.1. Global annual mean abundance and trends of key green-house gases [1.3].

LLGHG	Global abundance in 2013	Pre-industrial mole fraction	Present abundance relative to the year 1750	2012-2013 absolute increase	Mean absolute increase during last 10 years	RF
CO_2	396 ppm	278 ppm	142%	2.9 ppm	2.07 ppm/yr	65%
CH_4	1824 ppb	722 ppb	253%	6 ppb	3.8 ppb/yr	17%
N_2O	325.9 ppb	270 ppb	121%	0.8 ppb	0.82 ppb/yr	6%

1.2. Renewable energy sources

Renewable energy resources have pivotal importance in the world's future energy sector. It includes some forms of biomass, hydropower, geothermal, solar, wind, wave and tidal energy [1.4]. These energy sources exist virtually everywhere, in contrast to other energy sources, which are concentrated in a limited number of countries. Based on the report of Renewable Energy Policy Network for the 21st century, renewable resources provided 19 % to global energy consumption and 22 % to electricity generation in 2012 and 2013, respectively. Among these energy consumptions, 9 % comes from traditional biomass, 4.2% as heat energy (non-biomass), 3.8% hydro-electricity and 2% is electricity from the wind, solar, geothermal, and biomass [1.5]. The contribution of renewable energy is expected to increase significantly in the upcoming years. Rapid implementation of renewable energy resources can result in remarkable energy security, climate change mitigation, and economic benefits.

Besides, renewable energy technology has the potential to lift rural and remote areas, developing countries and under developed to new levels of prosperity [1.6].

1.3. The Solar Energy- World's future energy resource

Considering all the renewable energy sources, solar energy is the most abundant and widely distributed energy source. The sun radiates energy at the rate of 3.8×10^{23} kW, of which 1.8×10^{14} kW is intercepted by the earth. It indicates that in one second, the sun gives off more energy than people have used since the beginning of the time [1.7]. Furthermore, solar energy is one of the cleanest sources of energy, creating no harm towards natural resources such as water, air, and soil. It positively addresses the global warming issue (no emission of green- house gases) and does not produce solid or liquid waste materials [1.8]. Other advantages of solar energy that make it the backbone of serious sustainable development programs include restoration of degraded land, reduction of transmission lines from electricity grids, enhancing the quality of water resources, progress of national energy independence, diversification and security of energy supply and steady growth of rural electrification in developing countries [1.9]. Hence, it is often referred as "alternative energy" to conventional fossil fuel energy sources.

1.4. Photovoltaic technology

The human race has developed infinite technologies to harvest solar energy, radiant light and heat from the sun since ancient times. Current practises for utilization of solar energy falls into three categories: (1) thermal applications such as cooking, water heating, crop drying etc, (2) solar thermal electricity power system which generates electricity out of solar radiation through solar thermal conversion and (3) solar photovoltaic system that converts sunlight directly into electrical energy [1.10].

Solar photovoltaic power generation technology is an appealing method to produce electrical energy without any moving parts or emission of toxic substances to the environment during its operation. This elegant technology works under the principle of photovoltaic effect, which was discovered in 1954 when scientists at Bell Laboratories

noticed creation of electric charge in Silicon upon exposure to sunlight. A photovoltaic cell is the primary part of photovoltaic power generation system where the photovoltaic conversion process takes place. The photovoltaic cell is a p-n junction semiconductor device. The photovoltaic conversion process consists of three steps: (1) absorption of solar radiation (photons) by the absorber material in the solar cell, (2) generation of electron-hole pairs and (3) separation of electron-hole pairs to generate electricity. A photovoltaic cell absorbs solar radiation with energy equal to or greater than the bandgap of the absorber material used in it. Upon absorption of solar energy, the electrons in the valance band move to conduction band leaving hole behind it. The separation of generated electron–hole pair is executed by the electric field generated at the p-n junction. Figure 1.2 illustrates isolated p and n-type materials and its band diagram. Electrons are the majority carriers in n-type material, and negative charge of electrons are compensated by positively charged ionized donor atoms. While, a larger concentration of holes in the p-type material is compensated by the negatively charged ionized acceptor atoms.

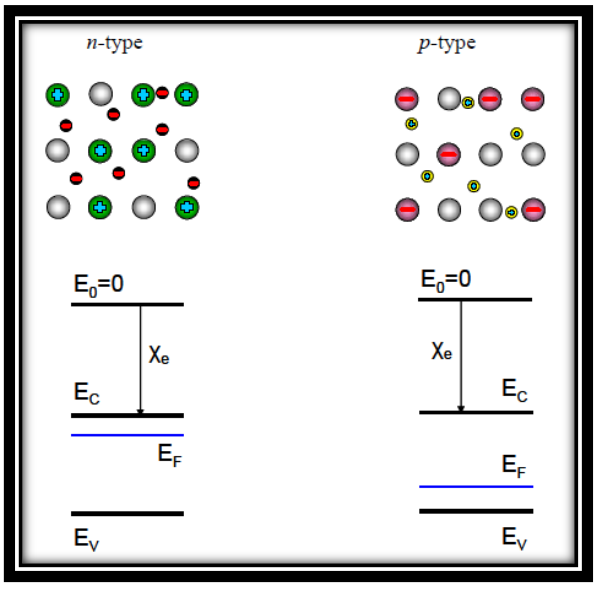

Fig.1.2. Schematic of isolated n-type and p-type semiconductor and their band diagram [1.11].

Figure 1.3 depicts the working principle of a solar cell. Formation of p-n junction by bringing p-and n-type material closer to each other results in the diffusion current of electrons from n-type material into p-type and holes from p-type to n-type material

across the junction due to the large difference in electron concentration existing between n and p-type material. Thus, the region close to p-n junction becomes completely depleted of mobile charge carriers and gives rise to a space charge created by charge of the ionised donor and acceptor atoms. The region of space charge is called as space charge region/ depleted region and constitutes ionised donor and acceptor atoms that are not balanced by the mobile charge carriers. While, the region outside the space charge region is called as quasi-neutral regions in which, the charge neutrality is maintained. The space charge region results in the formation of an internal electric field, which forces the charge carriers to move in a direction opposite to the concentration gradient thereby opposing the diffusion current flow. No net diffusion current flows across the p-n junction when the force by the concentration gradient and the internal electric fields compensate each other. This internal electric field drives the separation of generated electron-hole pair by favouring movement of the photogenerated electron from p- type to n- type and by preventing its movement from n-type to p-type material. The resulting movement of minority carriers across the junction creates a potential difference between the two end of p-n diode and current will flow through the solar cell [1.11].

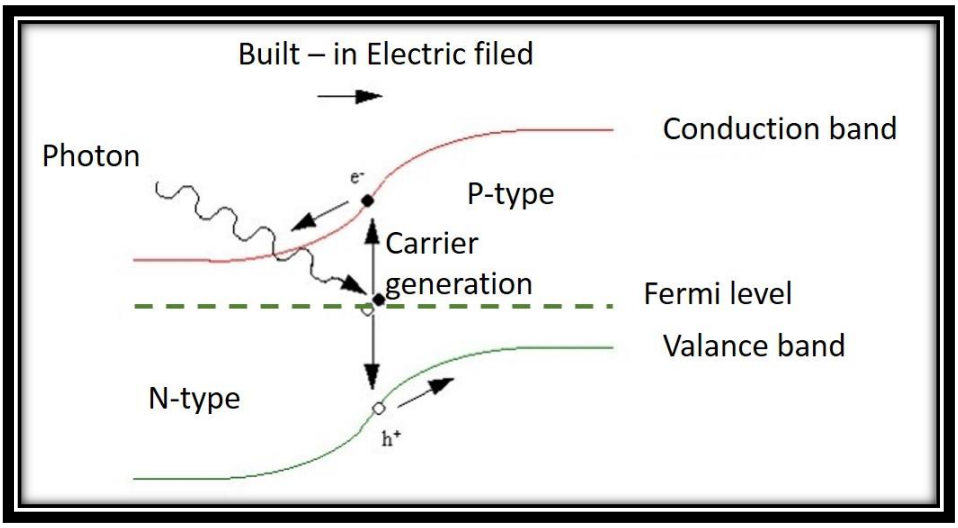

Fig.1.3. Schematic of working principle of a solar cell [1.12].

1.5. Status of photovoltaic (PV) market in the world

PV has made magnificent growth in the past decades. It can play a vital role in global electricity production in the future. Figure 1.4 shows global solar PV capacity from the year 2004 to 2014. It shows that global PV capacity has increased from 138 GW in 2013 to 177 GW in 2014. Thus 2014 is marked as a record year for growth of PV capacity [1.5]. This installed capacity is projected to be beyond 500 GW by 2020 and is foreseen as world's largest source of electricity by 2050 [1.13].

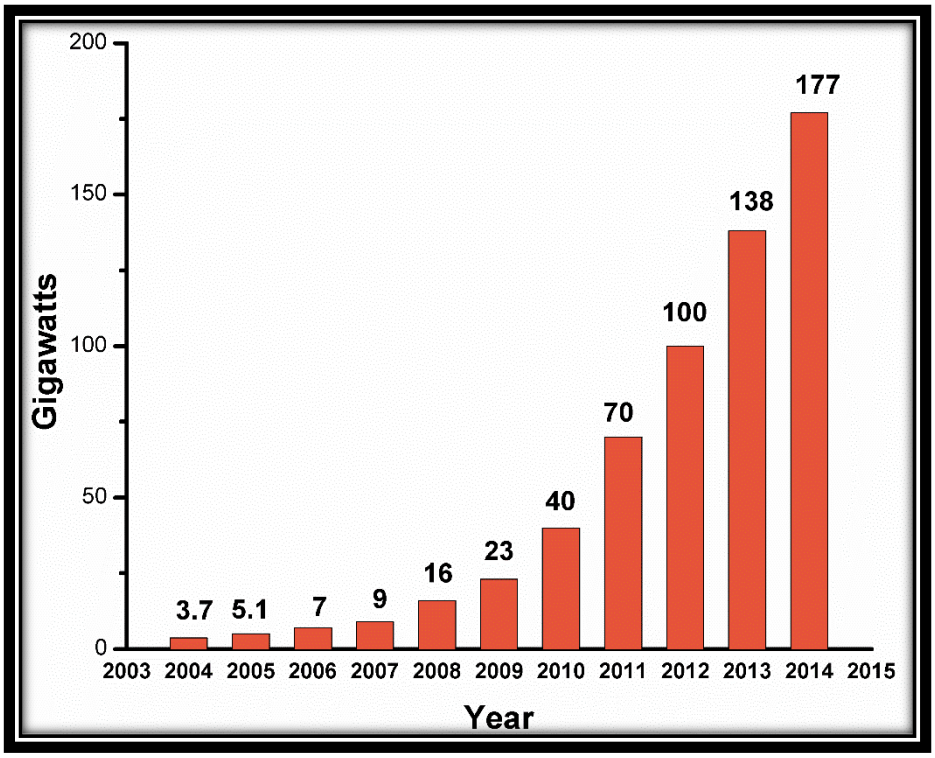

Fig.1.4. Global cumulative PV installed capacity from 2006 to 2014 [1.5].

Presently the top ten PV markets are China, Japan, United States, United Kingdom, Germany, France, Australia, South Korea, South Africa and India. Solar PV capacity and additions by these countries is given in figure 1.5. According to that, China added 10.6 GW in 2014 and increased its PV cumulative capacity to 28 GW. Japan expands PV capacity by adding 9.7 GW and raising total capacity to 23.3 GW. The other large PV markets in Asia are South Korea, India, and Thailand. The PV capacity of India reached 3.2 GW by the end of 2014. While United States installed 6.2 GW and raised

PV capacity to 18.3 GW. The Europe has total regional PV capacity of 87 GW. Within Europe, Germany and United Kingdom are the main PV installers. The United Kingdom installed 2.4 GW for a total of 5.2 GW whilst Germany installed 1.9 GW to achieve 38.2 GW. Australia installed 0.9 GW in 2014 for a total of 4.1 GW. PV market in Latin America has shown a rapid growth. However, growth rate differs from country to country. Among Latin America, Chile is regarded as the country of the clear majority of the region's installations. Chile added 395 MW to its existing 12 MW. Following Chile, Mexico showed considerable growth by increasing PV capacity to 64 MW. In late 2014, Brazil permitted for large- scale solar PV projects to produce 1 GW [1.5].

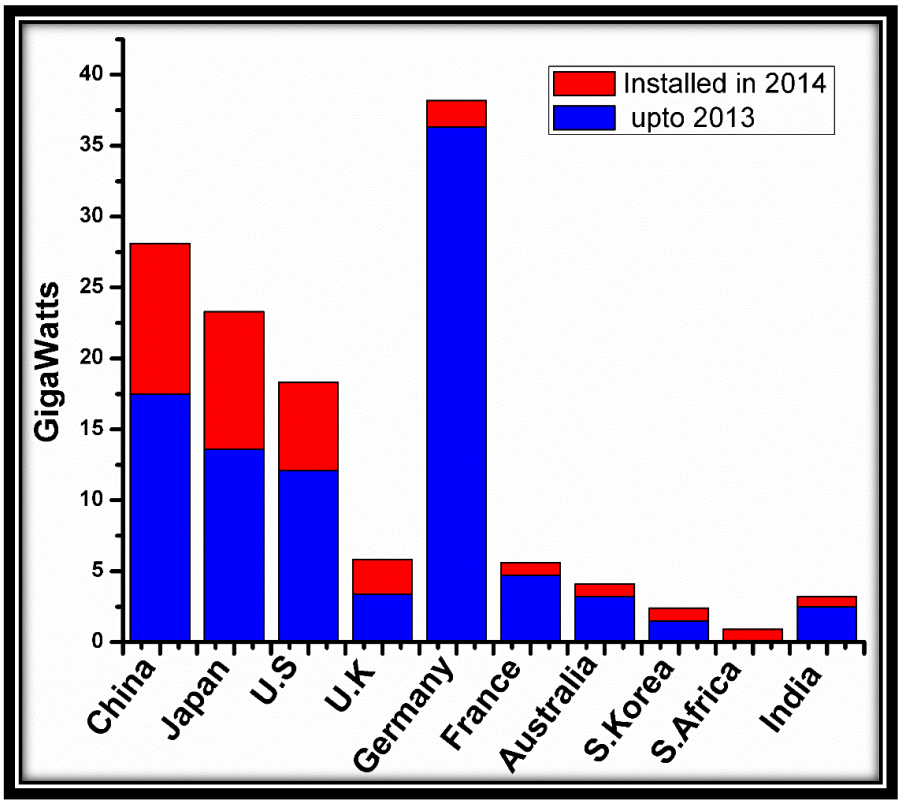

Fig.1.5. Solar PV capacity of top 10 countries based on addition in 2014 [1.5].

1.6. *Photovoltaic materials*

The centre of a solar cell is the light absorbing semiconductor material. There are certain requirements for a material to be used as an absorbing material in a solar cell. They are

(i) band gap between 1.1 and 1.7 eV
(ii) consisting of readily available, non- toxic materials
(iii) easy, reproducible deposition technique, suitable for large area production
(iv) Good photovoltaic conversion efficiency
(v) long-term stability
(vi) control of conduction type and resistivity and
(vii) high carrier lifetime

There are few materials used as the absorber material in solar cells. They are crystalline Si, amorphous Si, $CuInSe_2$ (CISe), $Cu(In,Ga)Se_2$ (CIGSe), CdTe, GaAs, GaInP, InP, organic semiconductors, Cu_2ZnSnS_4 (CZTS), perovskites, TiO_2 etc. [1.14-1.16]

1.7. Different Photovoltaic technologies

There are different PV technologies depending on the type of absorber material as mentioned in section 1.6. Amongst them c-Si-based solar cells has been the dominant part of PV market for the past two decades and this dominance is expected to continue [1.17]. Si becomes the most desirable photovoltaic material due to its attributes such as material abundance, high conversion efficiency (24%), a near-optimum energy gap (1.12 eV), excellent stability, low material cost and environmentally benign [1.18]. Though Si has a near optimum energy band gap to provide good conversion efficiency, it is an indirect bandgap material. Hence it has a low absorption coefficient (100 cm^{-1}) which is detrimental in a material point of view [1.19]. Around 100 μm thick Si is required to absorb 90% of the incident light. Diffusion length of the photogenerated electrons /holes should be twice the thickness of Si for them to be available at the heterostructure. This will be possible by ensuring a high crystalline quality of Si that demands complicated manufacturing process and increasing the cost of the photovoltaics [1.20]. Decrease in cost of Si solar cell can be possible by reducing the thickness of Si wafer and by developing a simpler and cheaper production process. Another solution to eliminate the cost issue of Si solar cell is to develop thin film solar cells in which the consumption of semiconducting material is reduced. The ability to fabricate solar cells on low-cost, large area, rigid or flexible substrate, the capability to

monolithically interconnect the solar cells, fewer processing steps and a higher degree of automation makes thin film photovoltaics favourable [1.21-1.22]. Another promising advantage of thin film solar cells is that only one side of the solar cell needs to be encapsulated as the substrate where the solar cell stack is deposited onto will serve as the other half of the encapsulation [1.23]. This paves a way to second generation solar cells called as “thin film photovoltaics” which is mainly classified into two groups: one based on thin films of amorphous, nanocrystalline and polycrystalline phases of Si and, the other based on polycrystalline chalcogenide semiconducting compounds including Cadmium Telluride (CdTe) and Copper Indium Gallium diselenide ($Cu(In,Ga)Se_2$ or CIGSe). The third generation of solar cells including dye-sensitized nanocrystalline or Gratzel solar cells, organic polymer-based photovoltaics, multi-junction solar cells, hot carrier solar cells, multi-band and thermophotovoltaic solar cells have been emerged with the aim of providing higher efficiency while maintaining the low cost offered by second generation solar cells [1.24].

Table 1.2 gives an overview and comparison of properties of current PV technologies. It shows that multi-junction solar cells with five junctions ((Al)GaInP/ AlGa(In)As/Ga(In)As/GaInPAs/GaIn(P)As) and three junctions (InGaP/GaAs/InGaAs) are currently showing highest efficiencies, 38.8 and 37.9 % respectively. Presently, these cells find application in space for satellites. The high production cost of this complex technology limits its extensive usage for terrestrial applications. While, considering cost effective thin film technology, CIGSe and CdTe based solar cells has attained 21.7 and 21.4 % efficiency in laboratory scale [1.25-1.26], which is equal to the efficiency of polycrystalline Si solar cells. Both, CIGSe and CdTe have temperature resistance higher than Si-based solar cells and have better performance in shades.

However, thin film CIGSe solar cells have a few advantages over CdTe. Primarily, CIGSe is slightly more efficient than CdTe in converting sunlight into usable energy. Secondly, they use less amount of toxic heavy metal Cadmium. CIGSe is suitable for building integrated photovoltaic markets other than ground and rooftop applications [1.28]. Besides, CIGSe has longest range in solar absorption spectrum (Figure 1.6) and high absorption coefficient (10^5/cm) among other thin film solar cells [1.29-1.30].

Table 1.2. Efficiency and solar cell parameters of current PV technologies [1.27]

Classification	Efficiency (%)	Area (cm^2)	V_{oc} (V)	J_{sc} (mA/cm^2)	Fill factor (%)	Description
Silicon						
Crystalline Si	25.6±0.5	143.7	0.740	41.8	82.7	Panasonic HIT
Multicrystalline Si	21.25±0.4	242.7	0.667	39.8	80.0	Trina Solar
Thin film minimodule Si	10.5±0.3	94	0.492	29.7	72.1	CSG solar
III-V cells						
GaAs thin film	28.8±0.9	0.9927	1.122	29.68	86.5	Alta devices
GaAs multicrystalline	18.4±0.5	4.011	0.994	23.2	79.7	RTI
InP crystalline	22.1±0.7	4.02	0.878	29.5	85.4	Spire
Thin film Chalcogenide						
CIGSe (cell)	21.0±0.6	0.9927	0.757	35.70	77.6	Solibro
CIGSe (minimodule)	18.7±0.6	15.892	0.701	35.29	75.6	Solibro
CdTe (cell)	21.0±0.4	1.0623	0.8759	30.25	79.4	First solar
Amorphous/microcrystalline Si						
Si (amorphous)	10.2±0.3	1.001	0.896	16.36	69.8	AIST
Si (microcrystalline)	11.8±0.3	1.044	0.548	29.39	73.1	AIST
Dye sensitised						
Dye	11.9±0.4	1.005	0.744	22.47	71.2	Sharp
Dye minimodule	10.7±0.4	26.55	0.754	20.19	69.9	Sharp
Organic						
Organic thin-film	11.0±0.3	0.993	0.793	19.40	71.4	Toshiba
Organic minimodule	9.7±0.3	26.14	0.806	16.47	73.2	Toshiba
Perovskite						
Perovskite thin film	15.6±0.6	1.020	1.074	19.29	75.1	NIMS
Multijunction						
Five junction cell (bonded)	38.8±1.2	1.021	4.767	9.56	85.2	Spectrolab
InGaP/GaAs/InGaAs	37.9±1.2	1.047	3.065	14.27	86.7	Sharp
GaInP/Si (mech.stack)	29.8±1.5	1.006	1.46	14.1	87.9	NREL
a-Si/nc-Si/nc-Si (thin-film)	13.6±0.4	1.043	1.901	9.92	72.1	AIST
a-Si/nc-Si (thin-film cell)	12.7±0.4	1.000	1.342	13.45	70.2	AIST

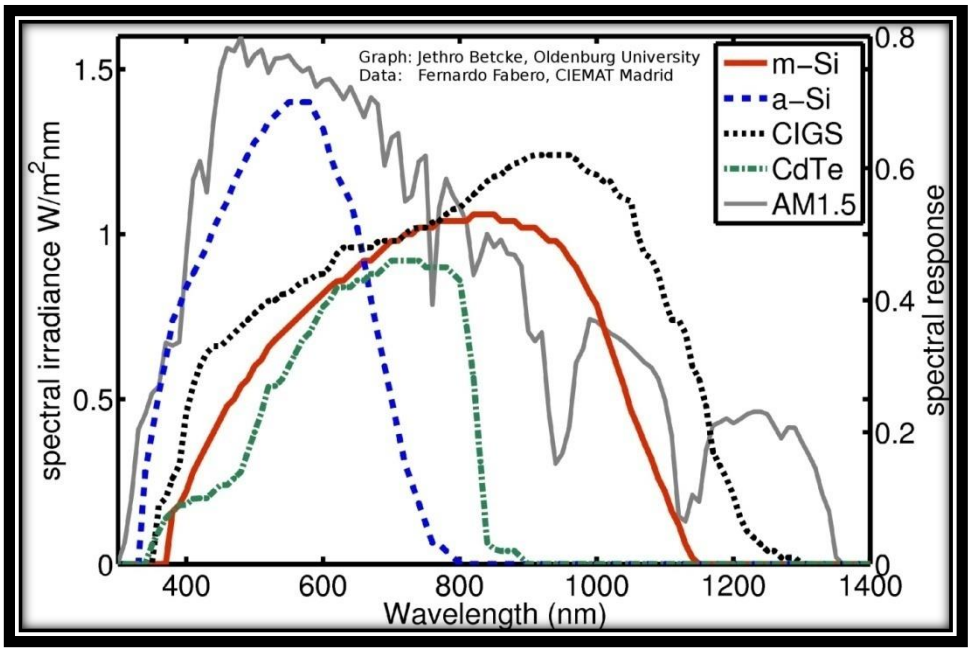

Fig.1.6. Spectral response of different thin film solar cell materials [1.29].

Even though the above-mentioned advantages of CIGSe solar cells do exist, the use of expensive high vacuum technologies such as co-evaporation or sputtering to deposit CIGSe absorber layer in high-efficiency solar cells put a limit on the extraction of the complete low-cost potential of CIGSe. The massive capital investments, difficulties in scaling to high volume production, poor material utilization efficiency and high manufacturing cost limits the commercialization of these approaches [1.31-1.32]. Research is trying to overcome this cost barrier through various approaches such as, i) replacing indium with lower-cost materials [1.33-1.34], ii) using novel materials such as kesterites [1.35] and wide bandgap materials for tandem cells [1.36], iii) material bandgap engineering [1.37], iv) non-vacuum deposition techniques such as electrodeposition, nanoparticle printing [1.38-1.39], and v) use of low cost substrates [1.40-1.41].

1.8. Goals and Objectives

The goals of this thesis are

(i) Synthesis of CIGSe particle by mechanochemical synthesis.

(ii) Study the effect of post-deposition heat treatments on the properties of CIGSe film.
(iii) Study the factors influencing grain growth and recrystallization of CIGSe film.
(iv) Exploration of potential of CIGSe film for photovoltaic application

To achieve these goals, this work is carried out focussing on the following objectives

(i) Optimization of mechanochemical synthesis to obtain single phase quaternary CIGSe particles.
(ii) Deposition of CIGSe film and study of the influence of post-deposition heat treatments on the film properties.
(iii) Effect of composition of CIGSe on grain growth and recrystallization during heat treatments.
(iv) Study of CIGSe absorber film in the Mo/CIGSe/CdS/Au heterojunction structure.

1.9. Structure of thesis

This present thesis is organised into six chapters. Chapter 1 presents the importance of renewable energy, in general, the importance of photovoltaic technology, its status, different photovoltaic materials and technologies, the importance of CIGSe as solar cell and current research to develop CIGSe solar cell at low cost. Chapter 2 describes the materials properties, deposition methods of CIGSe film and the importance of present work. The description of experimental procedures and equipment used for the deposition and characterization of CIGSe absorber is shown in chapter 3. The various techniques used for structural, morphological, compositional and electrical properties of particles and films are explained in detail in this chapter. The important results on the optimization of mechanical synthesis of $Cu(In,Ga)Se_2$ particles, ink formulation, annealing and selenization conditions are discussed in chapter 4. The results and discussion of properties of CIGSe film obtained from $Cu(In,Ga)Se_y$ particles with different Se content are presented in chapter 5. In both the chapter 4 and 5, X-Ray diffraction, EDAX, and FESEM results were given for determining crystal phase, composition and morphology. In addition, electrical properties of selected samples obtained using Hall-effect and I-V measurements are also given. Priliminary results of

Mo/CIGSe/CdS/Au heterojunction is given in chapter 6. Chapter 7 presents conclusion on important results of this study.

References

1.1 The outlook for energy: A view to 2040, (2015) 7-11, www.exxonmobil.com.sg/AP-English/Files/2015_outlook_for_Energy_Highlights.pdf

1.2 I.Yüksel, “Global warming and renewable energy sources for sustainable development in Turkey”, Renewable Energy 33 (2008) 802–812.

1.3 WMO green house gas bulletin, 10 (2014) 1-2, library.wmo.int/pmb_ged/ghg-bulletin_10-climate-summit-edition_en.pdf

1.4 S. Rathore, N.L. Panwar, “Renewable energy sources for sustainable development”, New India Publishing Agency, New Delhi, India (2007)

1.5 Renewables 2015, Global Status Report (2015) http://www/ren21.net/Portals/0/documents/e-paper/GRS2015/index.html#/120

1.6 A.K.N. Reddy, D.K. Subramanian, “The design of rural energy centers”, Indian Academy of Science (1980) 109–30.

1.7 M.Thirugnanasambandam, S. Iniyan, R. Goic, “A review of solar thermal technologies”, Renewable and Sustainable Energy Reviews 14 (2010) 312–22.

1.8 T. Tsoutsos, N. Frantzeskaki, V. Gekas, “Environmental impacts from the solar energy technologies”, Energy Policy 33 (2005) 289–96.

1.9 K.H. Solangi, M.R. Islam, R. Saidur, N.A. Rahim, H. Fayaz, “A review on global solar energy policy”, Renewable and sustainable Energy Reviews 15 (2011) 2149-2163.

1.10 N.L. Panwar, S.C. Kaushik, S. Kothari, “Role of renewable energy sources in environmental protection: A review”, Renewable and Sustainable energy reviews 15 (2011) 1513-1524.

1.11 https://ocw.tudelft.nl/wp-content/uploads/Solar-Cells-R4-CH4_Solar_cell_operational_principle.pdf

1.12 https://www.liverpool.ac.uk/renewable-energy/people-stephenson-institute-for-renewable-energy/ken-durose/

1.13 Technology Road Map-Solar Photovoltaic Energy, International Energy Agency (2014), www.iea.org/publications/freepublications/publication/TechnologyRoadmapSolarPhotovoltaicEnergy_2014edition.pdf

1.14 E. Ahmed, “Growth and characterization of CIGSe thin film for solar cell applications”, Dissertation (1995).

1.15 M.A. Green, “Thin-film solar cells: review of materials, technologies and commercial status”, Journal of Material Science: Materials in Electronics 18 (2007) S15-S19.

1.16 M. Habibi, F. Zabihi, M.R.A. Yazdi, M. Eslamian, “Progress in emerging solution-processed thin film solar cells Part II: Perovskite solar cells”, Renewable and Sustainable Energy Reviews 62 (2016) 1012-1031.

1.17 T.M. Razykov, C.S. Ferekides, D. Morel, E. Stefanakos, H.S. Ullal, H.M. Upadhyaya, “Solar photovoltaic electricity: Current status and future prospects”, Solar Energy 85 (2011) 1580–1608.

1.18 S.K. Deb, “Frontiers in photovoltaic materials and devices”, Current Opinion in Solid State & Materials Science 3 (1998) 51-59.

1.19 R.W. Miles, K.M. Hynes, I. Forbes, “Photovoltaic solar cells: An overview of state-of-the-art cell development and environmental issues”, Progress in Crystal Growth and Characterization of Materials 51 (2005) 1-42.

1.20 A. Goetzberger, C. Hebling, “Photovoltaic materials, past, present, future”, Solar Energy Materials & Solar Cells 62 (2000) 1-19.

1.21 A.G. Aberle, “Thin film solar cells”, Thin Solid Films,517, (2009),4706-4710.

1.22 P. Jayarama Reddy, “Solar Power generation: technology, new concepts & policy”, (2012).

1.23 S.R. Seyrling, “Advanced concepts for Cu(In,Ga)Se_2 solar cells”, Dissertation-ETH ZURICH (2011), http://e-collection.library.ethz.ch/eserv/eth:5222/eth-5222-02.pdf

1.24 D.M. Bagnall, M. Boreland, “Photovoltaic technologies”, Energy Policy 36 (2008) 4390-4396.

1.25 P. Jackson, D. Hariskos, R. Wuerz, O. Kiowski, A. Bauer, T.M. Friedlmeier, M. Powalla, “Properties of Cu(In,Ga)Se_2 solar cells with new record efficiencies up to 21.7%”, Physica Status Solidi (RRL) 9 (2015) 28-31.

1.26 First solar press release,http://www.pv-magazine.com/news/details/beitrag/first-solar-raises-bar-for-cdte-with-215-efficiency-record_100018069/#axzz3yxui6H3r

1.27 M.A. Green, K. Emery, Y. Hishikawa, W. Warta, E.D. Dunlop, “Solar cell efficiency tables version 47”,Progress in Photovoltaics: Research and Applications 24 (2016) 3-11.

1.28 A.A. Marcus, “Innovations in sustainability fuel and food”,(2015) DOI:10.1017/CB09781139680820.

1.29 J. Betcke, T. Behrendt, J. Kuehnert, A. Hammer, E. Lorenz, D. Heinemann, “Spectrally resolved solar irradiance derived from meteosat cloud information-methods and validation”, In: Proceedings of 2010 EUMETSAT Meteorological Satellite Conference, Cordoba (2010).

1.30 B. Vidhya, S. Velumani, A. Jesus, A. Alatorre, A.M. Acevedo, R. Asomoza, J.A.C. Caravayar, “Structural studies of mechanochemically synthesized $CuIn_{1-x}Ga_xSe_2$ nanoparticles”, Material Science Engineering B 174 (2010) 216–222.

1.31 D. Lee, K. Yong,” Non-vacuum deposition of CIGS absorber films for low cost thin film solar cells”, Korean Journal of Chemical Engineering 30 (2013)1347-1348.

1.32 M. Xue, J. Liu, Y. Huang, K. Han, J. Hu, K. Cheng, S. Wu and Z. Du, “A promising strategy to fabricate composition-adjustable chalcogenides by post-selenization of co-sputtered Cu/Ga/In precursors”, Material letters, 152 (2015) 240-243.

1.33 C. Colombara, L.M. Peter, K.D. Rogers, J.D. Painter, S. Roncallo, “Formation of $CuSbS_2$ and $CuSbSe_2$ thin film via chalcogenisation of Sb-Cu metal precursors”, Thin Solid Films 519 (2011) 7438-7443.

1.34 M. Kumar, C. Persson, “$CuSbS_2$ and $CuBiS_2$as potential absorber materials for thin-film solar cells”, Journal of Renewable Sustainable Energy 5 (2013) 031616-1-031616-6.

1.35 X. Liu, Y. Feng, H. Cui, F. Liu, X. Hao, G. Conibeer, D.B. Mitzi, M. Green, “The current status and future prospects of kesterite solar cells: a brief review”, Progress in Photovoltaics: Research and Applications 24 (2016) 879-898.

1.36 S. Seyrling, S. Calnan, S. Buecheler, A.N. Tiwari, “$CuIn_{1-x}Ga_xSe_2$photovoltaic devices for tandem solar cell application”, Thin Solid Films 517 (2009) 2411-2414.

1.37 S. Kang, R. Sharma, J.K. Sim, C.R. Lee, “Band gap engineering of tandem structured CIGS compound absorption layer fabricated by sputtering and selenization”, Journal of Alloys and Compounds 563 (2013) 207-215.

1.38 L. Ribeaucourt, G. Savidand, D. Lincot, E. Chassaing, “Electrochemical study of one-step electrodeposition of copper–indium–gallium alloys in acidic conditions as precursor layers for $Cu(In,Ga)Se_2$ thin film solar cells”, Electrochimica Acta 56 (2011) 6628-6637.

1.39 T. Wada, Y. Matsuo, S. Nomura, Y. Nakamura, A. Miyamura, Y. Chiba, A. Yamada, M. Konagai, “Fabrication of $Cu(In,Ga)Se_2$ thin films by a combination of mechanochemical and screen-printing/sintering processes”, Physica Status Solidi A 203 (2006) 2593-2597.

1.40 C.A. Kaufmann, A. Neisser, R. Klenk, R. Scheer, “Transfer of Cu(In,Ga)Se_2 thin film solar cells to flexible substrates using an in situ process control”, Thin Solid Films 480-481 (2005) 515-519.

1.41 R. Caballero, C.A. Kaufmann, T. Eisenbarth, T. Unold, R. Klenk, H.W. Schock, “High efficiency low temperature grown Cu(In,Ga)Se_2 thin film solar cells on flexible substrates using NaF precursor layers”, Progress in Photovoltaics: Research and Applications 19 (2011) 547-551.

CHAPTER - 2
MATERIAL PROPERTIES AND DEPOSITION METHODS OF $Cu(In,Ga)Se_2$ THIN FILM

2.1. History of Copper Indium Gallium Diselenide solar cells

Historically, Cu_xS/CdS thin film solar cells may be the origin for the development of Copper Indium Gallium Diselenide ($Cu(In,Ga)Se_2$ or CIGSe) solar cells [2.1]. As Cu_xS is an unstable compound and suffers degradation over time due to diffusion of Copper (Cu), Indium (In) is incorporated within it to improve the stability by forming strong covalent bonded compound $CuInS_2$.The bandgap of $CuInS_2$ is around 1.5 eV which is optimal to absorb maximum solar spectrum [2.2]. However, photovoltaic performance of $CuInS_2$ was inferior to its symmetrical compound $CuInSe_2$ (CISe), a compound semiconductor with lower bandgap (1.1 eV). Later, the bandgap of (CISe) was increased by adding Ga leading to the beginning of CIGSe semiconductor, which currently occupies mainstream market as next generation thin film solar cell.

2.2. Material properties of Copper Indium Gallium Diselenide

2.2.1. Structural properties

CIGSe is a quaternary semiconductor material. It belongs to group I-III-VI_2 of chalcopyrite family [2.3]. It is a solid solution of CISe and CGSe which crystallises in tetragonal chalcopyrite crystal system coming under I42d space group [2.4]. The chalcopyrite structure of CIGSe crystal is shown in figure 2.1.a. It can be obtained by stacking two unit cells of cubic zinc blend structure along c-axis (figure 2.1.b). In the chalcopyrite structure, each atom of group I (Cu) and group III (In/Ga) coordinate tetrahedrally to four atoms of group VI (Se). While, each atom of group VI is tetrahedrally coordinated to 2 atoms of group I and III in an ordered manner. From group I and III metallic atoms are denoted as cations while group VI atoms are denoted as anions [2.5]. Due to the difference in bond strength between group I-VI and group III-VI atoms, the ratio of lattice constants ‘c’ and ‘a’ (c/a) is not equal to 2, where 2 is

c/a of undisturbed crystal structure [2.6]. There is a distortion in the lattice structure which is known as tetragonal distortion (Δ) and is defined as Δ =2-c/a. Δ present linear dependence on the Ga content, x, in the $Cu(In_{(1-x)},Ga_x)Se_2$. Δ is negative for x < 0.23 and positive for x > 0.23. It could be due to change in electronegativities of In and Ga [2.7].

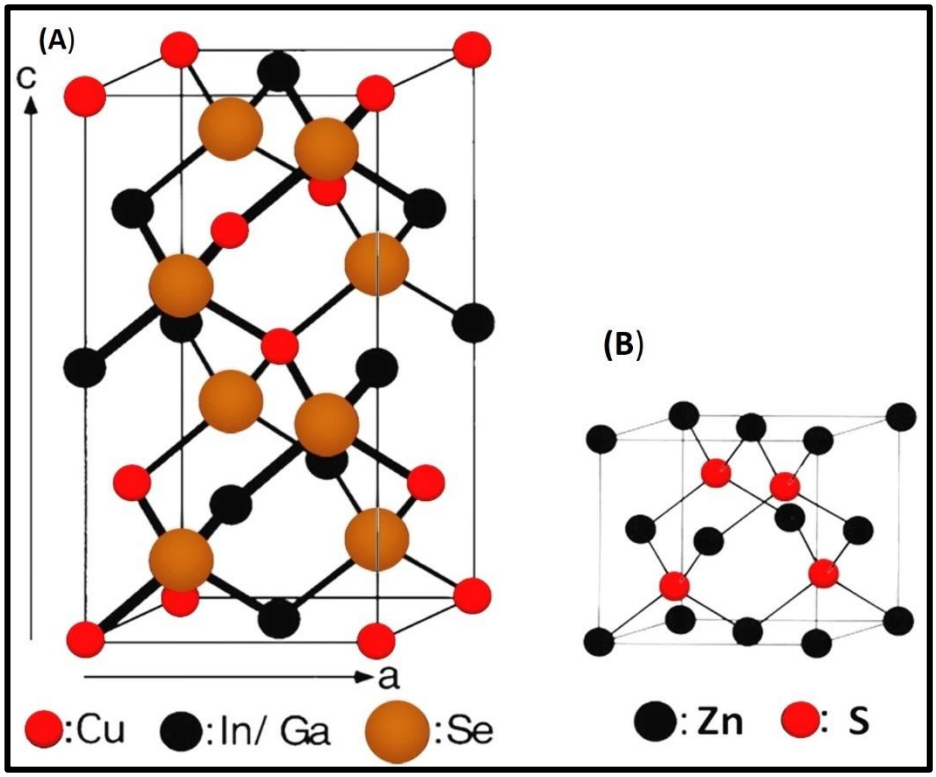

Fig.2.1. Comparison of (A) CIGSe chalcopyrite structure and (B) Zinc blend structure [2.8].

2.2.1.1 The phase diagram of CIGSe

The phase diagram is a graphical representation of all the equilibrium phases as a function of parameters of a system such as temperature, pressure and composition. Phase diagram of a multinary chalcopyrite system is complex. A phase diagram gives information on the phases that are present, transformations of phases and fractions of phases with the system parameters. Figure 2.2 shows ternary elemental composition diagram of Cu, In and Se [2.9]. It shows that chalcopyrite CISe phase lies on or near the Cu_2Se-In_2Se_3 tie line. The ordered defect compound (ODC) phases such as $CuIn_3Se_5$, $Cu_2In_4Se_7$, $Cu_3In_5Se_9$ lie on the same tie line. ODC phases are formed due to the regular arrangement of point defects in the chalcopyrite crystal structure.

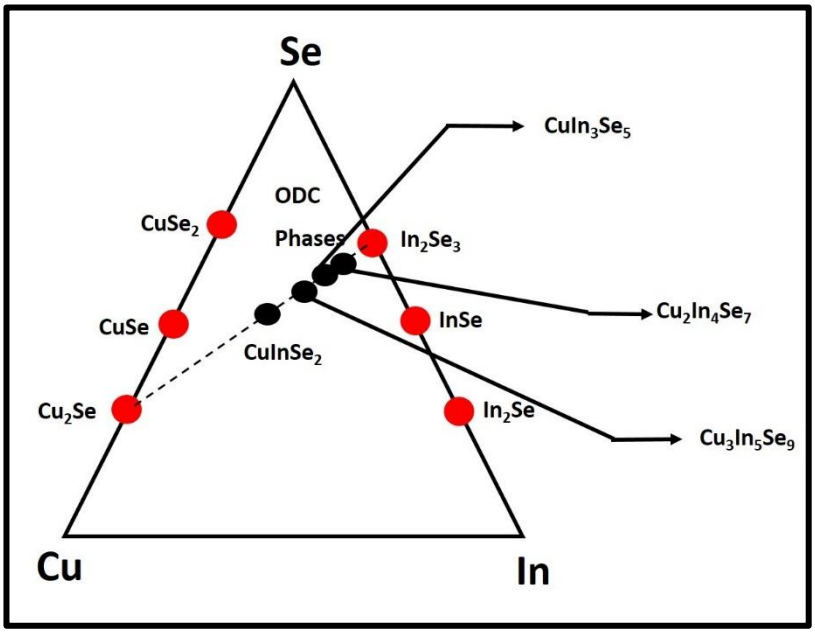

Fig.2.2. Ternary elemental composition diagram of CISe [2.9]

Pseudo binary phase diagram of CISe as a function of temperature and composition along Cu_2Se - In_2Se_3 tie line is shown in figure 2.3 [2.4]. According to the phase diagram, there exist α, β, and γ–phases of CISe. The α-phase of CISe has chalcopyrite crystal structure, and it exists in a very narrow range of Cu content (24 to 24.5%) at room temperature and at higher temperature up to 740 ºC. On the Cu-rich side, α-CISe phase exist with CuSe phase. On the Cu-poor side, CISe exists with β-$CuIn_3Se_5$ ODC phases. This ODC phase is formed by the ordered arrangement of Cu vacancies (V_{cu}) and In on Copper anti sites (In_{Cu}) defect pair. This defect pair has low formation energy. The delta phase of CISe, which has sphalarite crystal structure exists at high temperature and is unstable at room temperature (figure 2.3).

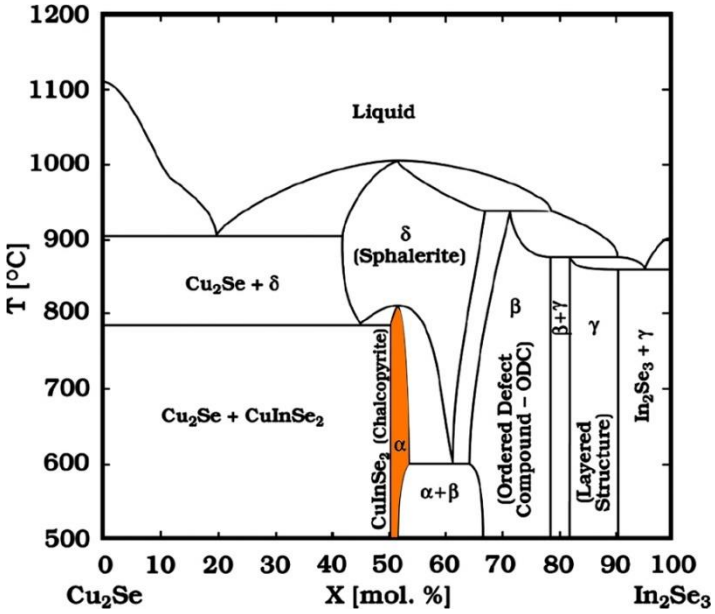

Fig.2.3. Pseudo binary phase diagram of CISe [2.4].

A congruent solid-solid phase transition occurs at 810 ˚C between the disordered δ-phase and the ordered chalcopyrite α-phase. The sphalarite phase differs from the chalcopyrite phase in the random distribution of Cu and In atoms. The introduction of Ga into CISe system widens the chalcopyrite region towards the lower concentration of Cu content (20.7%) [2.10]. This is believed to be due to the higher formation energy of V_{Cu}+Ga_{Cu} defect pair than V_{Cu}+In_{Cu} pair [2.11].

2.2.2. Optical properties

CIGSe is a direct band gap material. The bandgap of $Cu(In_{1-x},Ga_x)Se_2$ film can vary from 1.04 (x=0) to 1.67 eV (x=1) with increasing Ga content [2.12]. The variation in bandgap with respect to x, Ga/(In+Ga), is given by

$$E_g = (1-x)E_g\,(CISe) + xE_g\,(CGSe) + b.x(x-1) \qquad \text{(Eq : 2.1)}$$

Where, b is optical bowing coefficient. It is reported that the value of b can vary from 0.11- 0.24 [2.13]. Optical bowing coefficient results from the difference of volume deformation potential of the constituent elements and coupling of folded states through

the perturbation potential, the difference between the potential of CIGSe alloy and the average potential of the constituents, ΔV. Perturbation potential is affected by the chemical difference between In and Ga atoms and by the mismatch in the size of In and Ga atoms. The theoretical studies carried out by S.H.Wei [2.13] has shown that the increase in bandgap upon addition of Ga is due to the upward movement of conduction band minimum resulting from the ΔV induced interband coupling within the conduction band and valance band.

According to theoretical calculations, the bandgap of CIGSe for achieving highest efficiency should be 1.4 eV as spectral energy distribution of solar light is maximum at this value [2.14]. CIGSe attains this bandgap when Ga/(In+Ga) =0.6 [2.15]. However, the maximum experimental efficiency of CIGSe solar cell reported so far uses Ga/(In+Ga) =0.3 corresponding to the bandgap of 1.1 eV. The efficiency of CIGSe solar cells reduces when Ga/(In+Ga) > 0.3 [2.16]. The discrepancy between theoretical and experimental Ga/(In+Ga) values is not completely explained so far.

2.2.3. Electrical Properties

Electrical properties of CIGSe film plays a major role in controlling efficiency of solar cells. CIGSe film with p-type conductivity is needed for CIGSe solar cell application. Electrical properties of CIGSe film strongly depends on its composition and crystalline quality. The conductivity (ρ) of CISe can be either p-type or n-type depending on the concentration of Cu/In and Se/(Cu+In) ratio. Cu-poor and Se- rich CISe shows p-type conductivity as Cu vacancy (V_{cu}) act as acceptors. While Cu- rich and Se- poor films shows N-type conductivity as Se vacancies act as donor [2.17]. Wei et al [2.11] theoretically shown that addition of Ga to CISe improves the p-type nature since Ga_{Cu} antisite donor level is deeper than In_{Cu} donor level thus reducing the n-type nature. Carrier type, carrier concentration(p), resistivity and mobility (μ) of CIGSe film deposited by vacuum and non-vacuum methods are given in table 2.1.

Table 2.1 Effect of deposition methods on electrical properties of CIGSe film.

No	Composition of CIGSe film	Deposition method	Carrier type	p (cm^{-3})	ρ (Ωcm)	μ (cm^2/Vs)	Ref.
1	$Cu(In_{0.7},Ga_{0.3})Se_2$	3-stage evaporation	P	11×10^{17}	0.66	130	[2.18]
2	$Cu_{0.94}(In_{0.7},Ga_{0.3})Se_2$	3-stage evaporation	P	2.1×10^{15}	29.3	-	[2.19]
3	$Cu_{0.85}(In_{0.7},Ga_{0.3})Se_2$	3-stage evaporation	P	7.2×10^{14}	29.3	-	[2.19]
4	$Cu(In_{0.7},Ga_{0.3})Se_2$	Pulsed laser deposition (at room temperature)	P	10^{16}	100	20	[2.20]
5	$Cu(In_{0.7},Ga_{0.3})Se_2$	Pulsed laser deposition (at 500 ˚C)	P	10^{18}	0.1	9	[2.20]
6	$Cu(In_{0.7},Ga_{0.3})Se_2$	Selenization of In/(CuGa+In) layer	P	2.5×10^{21}	0.0005	27.29	[2.21]
7	$Cu(In_{0.7},Ga_{0.3})Se_2$	Selenization of CuGa/In layer	P	2.4×10^{20}	0.0006	41.96	[2.21]
8	$CuInSe_2$	Nanoplate-ink coating	P	1.4×10^{19}	0.9055	0.479	[2.22]
9	$Cu(In_{0.7},Ga_{0.3})Se_2$	CIGSe particle -ink coating	P	7.4×10^{14}	1000	1.9	[2.23]

The resistivity of films is 0.66 Ωcm and carrier density is in the order of 10^{17} cm^{-3} for the films deposited by co-evaporation technique [2.18]. However, lower value of carrier concentration in the order of 10^{14} cm^{-3} and higher value of resistivity in the order of 1 kΩ cm is reported for films deposited by particle-based techniques [2.23]. It is mainly attributed to the poor crystalline quality of films and high density of grain boundaries

[2.23]. The high carrier concentration of 2.5×10^{21} cm^{-3} reported by is assigned to the presence of metal like $Cu_{2-x}Se$ phase present in the Cu-rich CIGSe film [2.21]. It has been reported that optimum hole concentration and mobility for the photovoltaic application is in the range of 10^{15}-10^{17} cm^{-3} and 20-200 cm^2/VS respectively [2.24]. Minority carrier diffusion length in good quality CIGSe film is reported to be vary from 0.5 to 1µm [2.25]. Whereas majority carrier diffusion length of 110 nm is reported by Nichterwitz et.al [2.26].

2.3. Methods for deposition of CIGSe film

CIGSe thin film deposition process is the most critical process in the fabrication of CIGSe thin film solar cell. Film deposition parameters have a profound influence in determining the overall production cost and device performance. Many methods are developed for CIGSe thin film deposition. Among different deposition approaches, selection of thin film deposition technique should be implemented with utmost care due to an interplay between the power conversion efficiency, cost, and reliability [2.27].

In general, deposition methods for commercial manufacture of modules can be classified into two approaches. The first approach is vacuum co-evaporation process, in which CIGSe film formation takes place in a single growth process. The second approach is a two-step process, in which CIGSe film is deposited first using vacuum/non-vacuum method followed by annealing in Se atmosphere (selenization).

2.3.1. Co-evaporation process

Vacuum co-evaporation is the most successful process to deposit CIGSe absorber layers for high-efficiency cells [2.28]. It involves simultaneous evaporation of constituent elements Cu, In, Ga, and Se from multiple sources (either Knudsen type effusion cells or open boat sources) onto substrates, which are heated to 400-600 ºC. As the sticking coefficient of elements Cu, In and Ga are unity and of Se is less than 1, surplus Se is supplied throughout the deposition process. Film composition and growth rate of the process are controlled by the flux distribution and effusion rate from each source [2.28]. Depending on the variation in elemental fluxes, four types of co-evaporation sequences have been investigated which results in high-efficiency cells. They are, (i) stationary process in which the flux rate and deposition temperatures are constant throughout the process [2.29], (ii) Boeing process or bilayer process which

involves Cu-rich stage during the growth and end up with In- rich overall composition [2.30], (iii) three-stage process including deposition of $(InGa)_2Se_3$ at lower temperature followed by deposition of Cu and Se at elevated temperature and (iv) in-line process where, substrate is moving sequentially over the Cu, In and Ga sources to achieve flux distribution [2.31]. The bilayer process provides films with larger grain size than with stationary process whereas 3-stage process yields smoother film morphology than bilayer process. The highest efficiency of 21.7% is obtained by the film deposited using 3-stage co-evaporation process [2.32]. It can be due to high quality of co-evaporated CIGSe films such as smooth surface, high absorption efficiency and better carrier collection [2.33]. However, this technique adapts complicated procedure and requires precise temperature control to regulate the individual elemental fluxes during deposition, which demands complex equipment [2.27]. Another disadvantage is the material wastage during deposition. Additionally, this method has difficulties in scaling–up for a large manufacturing system such as roll-to-roll industrial process owing to its poor scaling uniformity, hurdles in continuous processing and low throughput [2.34].

2.3.2. Sequential Approach- Selenization of precursor material

The sequential approach is an attractive way for the deposition of CIGSe films. This method is suitable for large area deposition with good control over composition and thickness. Furthermore, it is a simple method with good control over material utilization, which was one of the drawbacks of co-evaporation approach. This is a two-step process where the first step is deposition of precursor material in metallic or alloy form and the second step is thermal annealing in an inert atmosphere to form CIGSe compound through chalcogenization reaction.Precursor layers can be deposited either by vacuum (evaporation, sputtering) or non-vacuum methods.

2.3.2.1. Vacuum approaches

Sputtering is an alternative industrially compatible method, which has developed rapidly over last decades. CIGSe film deposition by sputtering typically involves deposition of Cu-In-Ga precursor stack layers from pure metal or alloy targets and post deposition selenization. Solar Frontier has reported 20.9 % efficient CIGSe solar cells using this approach [2.35]. Previous reports have shown studies on CIGSe film formation from various multiple stack layers such as In/CuGa, In/CuGa/In/CuGa,

CuGa/In/CuGa and In/CuGa/In using co-sputtering or sequential sputtering from multiple targets [2.36-2.38]. However, the selenization process, which carries out at 450-550 ºC, involves many complicated phase formations and transformations. The main difficulty arises from the selenization process is loss of Indium from the precursor layer for its low melting point (140 ˚C) which in turn results in the rough surface morphology of films. Further, it leads to accumulation of Ga at the back side of films causing Ga deficiency on the surface of CIGSe film which is detrimental to open circuit voltage and thus to efficiency [2.39-2.41]. To overcome these issues, many are working on new strategies such as, (i) sputtering using single quaternary target, (ii) optimization of stacking sequence and (iii) making use of planetary rotation during the deposition of Cu-In-Ga precursor layer [2.42-2.45]. A conversion efficiency of 11.04 % is reported recently by optimizing the stacking sequence while an efficiency of 14.4% is reported availing planetary rotation during the precursor layer deposition [2.44, 2.45]. Still, the relatively lower efficiency is assumed to be due to inefficient diffusion of elements in the CIGSe during selenization owing to the multilayer structure. Evaporation is another vacuum approach mainly used for the formation of Cu-In-Ga precursor layer [2.46, 2.47].

2.3.2.2. Non-vacuum approaches

Non-vacuum film deposition processes are highly recommended and appealing alternative to vacuum-based processes. Non-vacuum processes utilize simple and inexpensive equipment such as screen printer, dip coater, spray deposition unit, spin coater, etc. for film deposition [2.48, 2.49]. It expedites development of industrial-scale, fast, continuous roll-to-roll production methods of CIGSe film. One major advantage of the non-vacuum process lies in the efficient usage of scarce, costly and highly demandable elements In and Ga. Thus, it could reduce the material cost [2.27, 2.50]. Furthermore, in many cases, non-vacuum processes can reach up to the coating quality of vacuum based process while providing significant benefits in capital costs, operating costs, functional complexity and competitive scale. The combination of low capital cost, low competitive scale and effective material usage helps to reduce the financial risk of thin-film PV manufacturing and thus to prevail the obstacles for commercialization. However, the lack of high purity vacuum environment during the film deposition should be compensated with careful choice of precursor material and

additives to reduce contamination [2.48,2.49]. There are two different approaches in the non-vacuum based deposition of CIGSe films: Electrodeposition and solution/ink based approaches.

2.3.2.2.1. Electrodeposition

Electrodeposition is a superior technology for the deposition of complex metallic layers. It is scalable at low cost as compared to technologies requiring high vacuum hence become apparent in the photovoltaics field where cost effective production is an important consideration [2.51]. Electrodeposition for CIGSe films has to take care of electrochemical behaviour of the four elements Cu, In, Ga and Se. Each of these elements presents distinct electrochemical properties causing the overall system very complex. (Electrodeposition potentials of Cu, Se, In, and Ga are 0.75, 0.34, -0.34 and -0.53 V, respectively, with respect to NHE (Normal Hydrogen Electrode)) [2.52]. There exist different routes for the electrodepositing CISe layer. One route involves deposition of a single elemental layer from single elemental bath solution and elemental stack layer is prepared by changing the bath solution. Kapur et.al [2.53] used this approach to prepare CISe films by selenising electrodeposited Cu/In bilayer. Another approach is to use a solution of two elements such as Cu and In simultaneously. Herrero et al. [2.54] first reported the electrodeposition of CISe film using this approach. Third and the simplest approach is deposition of CISe film from single bath solution containing three elements. This method is known as one-step electrodeposition and is initiated by Battacharya [2.55]. One-step electrodeposition of CISe film led to record photovoltaic conversion efficiency of 11.3%. However, one-step electrodeposition of CIGSe is found to be difficult due to the difficulty in insertion of Ga in the standard electrochemical potential domain resulting from the negative shift in the redox potential of Ga compared to In [2.52]. Though a record efficiency of 15.9% [2.56] is reported recently from electrodeposited CIGSe films, the hurdles concerned with the incorporation of Ga is yet to be overcome [2.57]. In addition to this, the stability of the chemical solution, large area, uniformity and high deposition rates are challenges to overcome [2.49].

2.3.2.2.2. Solution/ Ink- based Approaches

In ink-based approaches, films are deposited from solvent dispersions. The first step in this approach is the preparation of ink with suitable viscosity and precursor concentration. The thin film can be deposited by paste coating, printing, spraying, spin coating, etc. The viscosity of ink varies with mode of film deposition. A following drying step is necessary to burn out the organic content, which came from solvents and additives. The choice of solvent is crucial to obtain crack free films [2.58].

The ink-based approaches are mainly classified into molecular/ionic precursor and particle-based approaches. These two methods mainly differ in the mode of ink preparation. The molecular and ionic precursor ink is prepared by mixing metal salts in organic solvents or binders. On the other hand, particle- based ink is formulated by dispersing synthesized chalcopyrite CIGSe or binary selenide particles in organic solvents. Metal salt-based precursors and hydrazine-based precursors are the most widely used molecular-based precursor ink.

CIGSe film deposition by chemical spray pyrolysis of metal salt based precursor is one of the best investigated non-vacuum techniques. The process uses metal chlorides and chalcogenide such as N, N-dimethyl selenourea as precursor materials. This process involves decomposition and reaction of premixed precursor solution on a heated substrate [2.59, 2.60]. Though this technique is well investigated, the efficiency obtained is 5% for a small area cell [2.61]. The main drawbacks of this technique involve the presence of impurity phases, reaction by-products, and small grain size. Krunks et.al [2.62] and Marsillac et.al [2.63] reported that annealing in a controlled atmosphere can improve the crystalline quality and reduce the impurity concentration.

The hydrazine-based approach is a simple and high-throughput solution process for the preparation of high-efficiency PV devices [2.64]. The development of hydrazine-based methods for preparation of CIGSe thin film photovoltaic device with photoconversion efficiency of 10.3 % was reported by Mitzi et.al in 2008 [2.65]. Since then hydrazine-based process is considered as the most victorious solution based route to obtain high quality CIGSe films. Hydrazine is an organic solvent containing two amine groups (N_2H_4). It is highly volatile so that it can be easily removed from the films under heat treatment [2.27]. In addition, contrary to the conventional organic solvents, metal chalcogenides have preferable solubility in hydrazine. The hydrazine-

based deposition route involves three steps, (i) dissolution of metal chalcogenides in a hydrazine-based solution at room temperature such that solution consists of metal chalcogenide anions separated by hydrazinium ($N_2H_5^+$) cations, (ii) deposition of precursor solution into thin film form, and (iii) heat treatment of films in an inert atmosphere to yield CIGSe films. The prime characteristic of this route is that it excludes the post-annealing of film in selenium atmosphere. It provides films without impurities as hydrazine does not include extra elements such as oxygen and carbon [2.60]. Moreover, hydrazine–based process can easily incorporate Ga and other favourable impurities such as Na [2.64]. Even so, hydrazine is a highly reactive and toxic solvent. Therefore, use of hydrazine raise many environmental and safety concerns. The precursor preparation and film deposition processes must be carried out in an inert atmosphere and large-scale industrial production of CIGSe solar cells using this method requires strict operational regulations and safety precautions [2.64,2.27, 2.67].

Particle-based approach is considered as highly efficient method for CIGSe deposition. The possibility to have good control over film composition by synthesising particle with desired composition and crystal phase makes this approach distinct. Moreover, it enables free substrate choice, large area and high- throughput manufacturing. Figure 2.4 shows schematic of particle-based approach [2.27]. This approach involves synthesis of particles, formulation of ink and coating of substrate with particle ink or slurry. Generally, a drying process follows deposition to immobilize the particles on the substrate. This soft annealing is followed by high temperature annealing (selenization) to achieve dense, non- porous and continuous device quality films.

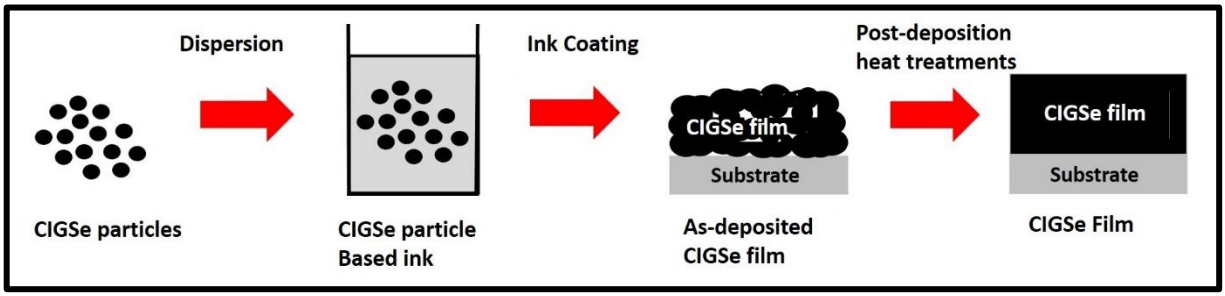

Fig.2.4. Schematic of particle-based approach for CIGSe film deposition [2.27].

There is plenty of chemical methods to synthesize CIGSe particles. One of the method includes synthesis of CIGSe particle by open-air solvothermal reaction of metal salts and Se in organic solvents. But the synthetic cycle is long and involves the use of organic solvents which are harmful to the environment [2.68,2.69]. Synthesis of CIGSe particles with uniform size distribution in the range of 5-20 nm by the colloidal process starting from metal halides and organic solvents such as Pyridine, Ethylenediamine, and Olylamine as solvents has reported by many. In addition to the long synthetic duration and use of organic solvent, colloidal process employs the use of highly toxic Na_2Se as Se source [2.70-2.72]. Mechanochemical synthesis of CIGSe particle is simple and time-saving route as compared to conventional particle synthesis methods. It is an environmental friendly process as the use of solvent is not essential for the particle synthesis. Mechanical alloying of CIGSe particles was first reported in 1998 by Suryanarayana et.al [2.73]. They synthesized CIGSe particles from elemental powders of Cu and Se and fine granules of Ga and In by milling at the ball to powder ratio (BPR) of 20:1 at 300 rpm for 20 minutes [2.73]. Eventually, many researchers have studied the importance of milling parameters such as milling speed and milling time on the formation of CIGSe particles [2.5,2.74,2.75]. Ying et.al [2.70] mechanically alloyed CIGSe particles from metal selenides and film were deposited by spin coating. A solar cell with photoconversion efficiency of 2.7% was fabricated by Wada et.al [2.77] using screen printing of mechanically alloyed CIGSe particles.

As mentioned in the second paragraph of this section, the particle-based ink formulation requires the use of organic additives such as Ethyl cellulose, Terpineol, Polyethylene glycol, etc. to improve its dispersibility [2.78,2.79]. These additives are long aliphatic hydrocarbonate chains. Since these organic additives have electrical insulating character, it may deteriorate the electronic properties of CIGSe films and thereby affect the solar cell performance [2.80]. A heat treatment at a moderate temperature (250-300 ºC) is commonlly provided to films for removing the organic additives. Another issue related to film deposition using particle-based ink is smaller grain size and porosity. The smaller grains and the resulting high amount of grain boundaries lower the efficiency of a solar cell since grain boundaries act as non-radiative centers where the charge carriers recombine without releasing photons. This process lowers the light generation efficiency of the film and enhances heat loss. For this reason, conversion of smaller grains to larger grain is essential to improve the

solar cell efficiency by suppressing the above-mentioned effect. The densification of the porous film, recrystallization and grain growth can be achieved by selenizing at high temperature (500-600 ºC) for 15- 30 min in a controlled atmosphere. The supply of selenium is to compensate the loss of Se from the film during annealing at 500-600 ºC as Se evaporates at 350 ºC.

However, many have reported little densification and grain growth from selenization of films deposited using stoichiometric CIGSe particles [2.81, 2.82, 2.79, 2.83]. It could be due to the dependence of grain growth and recrystallization on the chemical composition and structural properties of precursor films as chalcopyrite CIGSe compound has high covalent bonding character that results in high a melting point (1000 ºC) and low atomic diffusions [2.84,2.85]. Researchers have investigated different approaches for promoting grain growth and densification of CIGSe precursors. Chalcogen exchange during sintering [2.86], doping of impurities such as Na and Sb [2.87-2.91], the addition of CuSe as fluxing agent during sintering [2.92] are common among them. Even though CuSe assisted sintering is a successful method to enhance recrystallization and grain growth, the extra CuSe will remain as secondary phase in the final film even after selenization. CuSe has high electrical conductivity and creates shunt path in the absorber thereby deteriorate solar cell performance. Hence, CuSe should be removed from the film by etching using KCN which is highly poisonous. Instead of adding CuSe to CISe film, A.E. Zaghi et.al [2.93] has recently reported enhancement in grain growth and recrystallization in films deposited by mechanically alloyed CISe particles by reducing the Se content in the initial CISe powder.

In this study, we investigate the properties of CIGSe films obtained by doctor blade deposition of mechanochemically synthesised $Cu(In,Ga)Se_2$ particle. To address the issue of difficulty in the conversion of smaller grains to larger grains, we extended the work carried out by Zaghi et. al [2.87] to CIGSe system and the effect of Se content in the initial $Cu(In,Ga)Se_2$ particle to enhance the recrystallization and grain growth of mechanochemically synthesized CIGSe particle-based precursor films is investigated.

References

2.1. D.C. Reynolds, G. Leies, L.L. Antes R.E. Marburger, “Photovoltaic effect in Cadmium Sulfide”, Physical Review Letters 96 (1954) 533-534.

2.2. Yoshino, K. Ikari, T. Shirakata, S. Miyake, H. Hiramatsu, K. Sharp, “Band edge photoluminescence of high purity $CuInS_2$ single crystals”, Applied physics letters 78 (2001) 742-744.

2.3. L. Shay, J. Wernick, TernarL. Shay, J. Wernick, “Ternary Chalcopyrite semiconductors”, Pergamon, Oxford, 1975.

2.4. B. J. Stanbery, “Copper Indium Selenide and Related Materials for Photovoltaic Devices” Critical Reviews in Solid State and Materials Sciences 27 (2002) 73-117.

2.5. B. Rehani, J.R. Ray, C.J. Panchal, H. Master, R.R. Desai, P.B. Patel, “Mechanochemically Synthesized CIGS nanocrystalline powder for solar cell application”, Journal of nano and electronic physics 5 (2013) 02007-1-02007-4.

2.6. S. C. Abrahams, J. L. Bernstein, “Piezoelectric nonlinear optic $CuGaSe_2$ and $CdGeAs_2$: Crystal structure, chalcopyrite micro hardness, and sub lattice distortion”, The Journal of Chemical Physics 61 (1974) 1140-1146.

2.7. D. Abou-Ras, R. Caballero, C. A. Kaufmann, M. Nichterwitz, K. Sakurai, S. Schorr, T. Unold, H. W. Schock, “Impact of the Ga concentration on the microstructure of $CuIn_{1-x}Ga_xSe_2$”, Physica Status Solidi (RRL) 2 (2008) 135-137.

2.8. F.J. Fan, L. Wu, S.H.Yu, “Energetic I-III-VI_2 and I_2-II-VI_4 nanocrystals: synthesis, photovoltaic and thermoelectric applications”, Energy Environmental Science 7 (2014) 190-208.

2.9. W.N. Shafarman and L. Stolt, “Cu(InGa)Se_2 Solar Cells”, in Handbook of Photovoltaic Science and Engineering, Hoboken, NJ:Wiley (2003).

2.10. D. Rudmann, G. Bilger, M. Kaslin, F.J. Haug, and H. Zogg, “Effects of NaF co-evaporation on structural properties of Cu (In,Ga)Se_2 thin films”, Thin Solid Films 431 (2003) 37-40.

2.11. S.H. Wei, S.B. Zhang, A. Zunger, “Effect of Ga addition to $CuInSe_2$ on its electronic, structural and defect properties”, Applied Physics letters 72 (1998)3199-3201.

2.12. M. Gloeckler, J.R. Sites, “Band-gap grading in Cu(In,Ga)Se_2 solar cells”, Journal of Physics and Chemistry of Solids 66 (2005) 1891–1894.

2.13. S.H. Wei, A. Zunger, “Band offsets and optical bowings of chalcopyrites and zinc based II-VI alloys”, Journal of applied physics 78(1995) 3846- 3856.

2.14. C.J. Chen, “Nature of Solar Radiation”, in Physics of Solar Energy, Hoboken, NJ: Wiley (2011).

2.15. M.A. Contreras, L.M. Mansfield, B. Egaas, “Improved energy conversion efficiency in wide bandgap Cu (In,Ga)Se_2 solar cells, 37th IEEE photovoltaic specialists conference (PVSC 37) Seattle, Washigton, June (2011) 19-24.

2.16. I. Repins, M.A. Contreras, B. Egaas, “19.9 % efficient ZnO/CdS/CIGSe solar cells with 81.2% fill factor. Progress in photovoltaics: Research and applications 16 (2008) 235-239.

2.17. S.B. Zhang, S.H. Wei, A. Zunger, H.K. Yoshida, “Defect physics of the CISe chalcopyrite semiconductor”, Physical Review B57 (1998) 9642-9656.

2.18. F. Mesa, C. Calderon, G. Gordillo, “Study of electrical properties of CIGS thin films prepared by multistage processes”, Thin Solid Films 518 (2010) 1764-1766.

2.19. L. Zhang, F.F. Liu, F.Y. Li, Q. He, B.Z. Li, C.J. Li, “Structural,optical and electrical properties of low-temperature deposition Cu(In_xGa_{1-x})Se_2 thin films”, Solar Energy Materials and Solar Cells 99 (2012) 356-361.

2.20. Y.H. Jo, B.C. Mohanty, Y.S. Cho, “Enhanced electrical properties of pulsed laser-deposited $CuIn_{0.7}Ga_{0.3}Se_2$ thin films via processing control”, Solar Energy 84 (2010) 2213-2218.

2.21. S.U. Park, R. Sharma, K. Ashok, S. Kang, J.K. Sim, C.R. Lee, “A study on composition, structure and optical properties of Cu-poor CIGSe thin film deposited by sequential sputtering of CuGa/In and In/(CuGa+In) precursors”, Journal of Crystal Growth 359 (2012)1-10.

2.22. H.L. Liu, Z. Jin, W. Wang, J.Li, “Monodispersed sphalerite $CuInSe_2$ nanoplates and highly (112) oriented chalcopyrite thin films by nanoplate ink coating”, Crystal Engineering Communication 13 (2011) 7198- 7201.

2.23. B. Vidhya, “Preparation and characterization of nanostructured $CuInGaSe_2$ and CdZnS thin films for photovoltaic applications” Dissertation, CINVESTAV (2010).

2.24. M. Beres, K.M. Yu, J. Syzdek, S.S. Mao, “Improvement in the electronic quality of pulsed laser deposited $CuIn_{0.7}Ga_{0.3}Se_2$ thin films via post-deposition elemental sulfur annealing process”, Thin Solid Films 608 (2016) 50-56.

2.25. G. Brown, V. Faifer, A. Pudov, S. Anikeev, E. Bykov, M. Contreras, J. Wu, “Determination of the minority carrier diffusion length in compositionally graded Cu(In,Ga)Se_2 solar cells using electron beam induced current”, Applied Physics Letters 96 (2010) 022104-1-3.

2.26. M. Nichterwitz, “Charge carrier transport in Cu(In,Ga)Se_2 thin-film solar-cells studied by electron beam induced current and temperature and illumination dependent current voltage analyses”, Dissertation, Berlin (2012).

2.27. D. Lee, K. Yong,” Non-vacuum deposition of CIGS absorber films for low cost thin film solar cells”, Korean Journal of Chemical Engineering 30 (2013)1347-1348.

2.28. U.P. Singh, S.P. Patra, “Progress in polycrystalline thin film Cu(In,Ga)Se_2 solar cells” International journal of photoenergy, 2010 (2010) 1-20.

2.29. W. N. Shafarman, J. Zhu, “Effect of substrate temperature and deposition profile on evaporated Cu (In,Ga)Se_2 films and devices,” Thin Solid Films 361 (2000) 473–477.

2.30. R. A. Mickelsen, W. S. Chen, “High photocurrent polycrystalline thin-film CdS/CuInSe2 solar cells,” Applied Physics Letters 36 (1980) 371-373.

2.31. G. M. Hanket, P. D. Paulson, U. Singh, S.T. Junker, R.W. Birkmire, F.J. Doyle, E. Eser, W.N. Shafarman, “Fabrication of graded Cu(InGa)Se_2 films by inline evaporation,” in Proceedings of the IEEE Photovoltaic Specialists Conference (PVSC ’2000) 499-504.

2.32. Solar Frontier achieves world record thin film solar cell efficiency: 22.3%, http://www.solar-frontier.com/eng/news/2015/C051171.html

2.33. P. Jackson, D. Hariskos, R. Wuerz, O. Kiowski, A. Bauer, T.M. Friedlmeier, M. Powalla, “Properties of Cu(In,Ga)Se_2 solar cells with new record efficiencies up to 21.7%”,physica status solidi(RRL) 9 (2015) 28-31.

2.34. M. Xue, J. Liu, Y. Huang, K. Han, J. Hu, K. Cheng, S. Wu, Z. Du, “A promising strategy to fabricate composition-adjustable chalcogenides by post-selenization of co-sputtered Cu/Ga/In precursors”, Material letters, 152 (2015) 240-243.

2.35. Solar Frontier, 2014. Solar Frontier sets thin-film PV world record with 20.9% CIS cell. <http://www.solar-frontier.com/eng/news/2014/C031367.html> (accessed 01.10.15).

2.36. N.B. Raghu, “CIGS-based solar cells prepared from electrodeposited stacked Cu/In/Ga layers” Solar Energy Materials and Solar cells 113 (2013) 96-99.

2.37. S. Park, J. Kim, “Structural analysis of Cu(In,Ga)Se_2 films fabricated by using sputtering and post -selenization”, Current Applied Physics 13 (2013) 1046-1049.

2.38. W. Li, Y. Sun, W. Liu, L. Zhou, “Fabrication of Cu(In,Ga)Se_2 thin films solar cell by selenization process with Se vapor”, Solar Energy 80 (2006) 191-195.

2.39. H. Liang, U. Avachat, W. Liu, J.V. Duren, M. Le “CIGS formation by high temperature selenization of metal precursors in H_2Se atmosphere”, Solid-State Electron 76 (2012) 95–100.

2.40. O. Lundberg, M. Bodegard, J. Malmstrom, L. Stolt, “Influence of the Cu(In,Ga)Se_2 thickness and Ga grading on solar cell performance”, Progress in photovoltaics: Research and applications 11 (2003) 77-88.

2.41. Z.S. Bhaji, Z. Labadi, Gy. Molnar, B. Pecz, A.L Toth, J. Toth, A. Csik, I. Barsony, “Post selenization of stacked precursor layers for CIGS”, Vacuum 92 (2013) 44-51.

2.42. L. Ouyang, M. Zhao, D. Zhuang, J. Han, Z. Gao, L. Guo, X. Li, R. Sun, M. Cao, “Annealing treatment of Cu(In,Ga)Se_2 absorbers prepared by sputtering a quaternary target for 13.5% conversion efficiency device”, Solar Energy 118 (2015) 735-383.

2.43. J.H. Shi, Z.Q. Li, D.W. Zhang, Q.Q. Liu, Z. Sun, S.M. Huang, “Fabrication of Cu(In, Ga)Se_2 thin films by sputtering from a single quaternary chalcogenide target”. Progress in Photovoltaic Research and Applications 19 (2011) 160-164.

2.44. T.T. Wu, J.H. Huang, F. Hu, C.H. Chang, W.L. Liu, T.H. Wang, C.H. Shen, J.M. Shieh, Y.L. Chueh, “Toward high efficiency and panel size 30×40 cm^2 Cu(In,Ga)Se_2 solar cell: Investigation of modified stacking sequences of metallic precursors and pre-annealing process without Se vapor at low temperature”, NanoEnergy 10 (2014) 28-36.

2.45. K. Kim, H. Park, G.M. Hanket, W.K. Kim, W.N. Shafarman, “Composition and bandgap control in Cu(In,Ga)Se_2 – based absorbers formed by reaction of metal precursors”, Progress in Photovoltaics Research and Applications 23 (2015) 765-772.

2.46. F.B. Dejene, “The structural and material properties of $CuInSe_2$ and Cu(In,Ga)Se_2 prepared by selenization of stacks of metal and compound precursors by Se vapour for solar cell applications”, Solar energy and solar cells 93 (2009) 577-582.

2.47. Z.H. Li, E.S. Cho, S.J. Kwon, “Crystal growth of Cu(In,Ga)Se_2 film by RTP annealing of the stacked elemental layers formed by E-beam evaporation”, Journal of Crystal Growth 387 (2014) 117-123.

2.48. C. Eberspacher, C. Fredric, K. Pauls, J. Serra, “Thin-film CIS alloy PV materials fabricated using non-vacuum particle –based techniques”, Thin solid films 387 (2001) 18-22.

2.49. M. Kaelin, D. Rudmann, A.N. Tiwari, “Low cost processing of CIGS thin film solar cells”, Solar Energy 77 (2004) 749-756.

2.50. P.W. Li, W.H. Zhou, Z.L. Hou, S.X. Wu, “Synthesis of $CuIn_xGa_{1-x}Se_2$ nanocrystals for potential thin film potential application under air condition”, Materials Letters 78 (2012) 131-134.

2.51. L. Ribeaucourt, G. Savidand, D. Lincot, E. Chassaing, “Electrochemical study of one-step electrodeposition of copper–indium–gallium alloys in acidic conditions as precursor layers for $Cu(In,Ga)Se_2$ thin film solar cells”, Electrochimica Acta 56 (2011) 6628-6637.

2.52. D. Lincot, J.F. Guillemoles, S. Taunier, D. Guimard, J. Sicx-Kurdi, A. Chaumont, O. Roussel, O. Ramdani, C. Hubert, J.P. Fauvarque, N. Bodereau, L. Parissi, P. Panheleux, P. Fanouillere, N. Naghavi, P.P. Grand, M. Benfarah, P. Mogensen, O. Kerrec, “Chalcopyrite thin film solar cells by electrodeposition”, Solar energy 77 (2004) 725-737.

2.53. V.J. Kapur, B.M. Basol, E.S. Tseng, “Preparation of thin films of chalcopyrites for photovoltaics”. In: Hwang, H.L., et.al. (Eds.), Proceedings Seventh International Conf. Ternary and Multinary Compounds, (1987) 219–224.

2.54. J. Herrero, J. Ortega, “Electrodeposition of Cu–In alloys for preparing $CuInS_2$ thin films”, Solar Energy Materials 20 (1990) 53–65.

2.55. R.N. Bhattacharya, “Solution growth and electrodeposited $CuInSe_2$ thin films”, Journal of the Electrochemical Society130 (1983) 2040–2042.

2.56. V. Bermudez, “Current status at NEXCIS, towards industrial phase”, 5th International Workshop on CIGS Solar Cell Technology, Berlin, Germany, 2014.

2.57. J.C. Malaquias, M. Steichen, P.J. Dale, “One-step Electrodeposition of metal precursors from a deep eutectic solvent for $Cu(In,Ga)Se_2$ thin film solar cells”, Electrochimica Acta 151 (2015) 150-156.

2.58. A. Carrete, “Solution -processing of chalcogenide nanoparticles and thin films for photovoltaic applications” Dissertation, Barcelona (2015).

2.59. B. Pamplin, R.S. Feigelson, “Spray pyrolysis of $CuInSe_2$ and related ternary semiconducting compounds”, Thin Solid Films 60 (1979) 141–146.

2.60. B.J. Brown, C.W. Bates, “Similarities in the chemical mechanisms of CuInSe2 and CdS thin-film formation by chemical spray pyrolysis”, Thin Solid Films 188 (1990) 301–305.

2.61. S. Duchemin, J. Bougnot, A. El Ghzizal, K. Belghit, “Studies on the improvement of sprayed CdS–$CuInSe_2$ solar cells”. In: Palz, W., Wrixon, G.T., Helm, P. (Eds.), Proceedings of the 9th EPVSEC, Freiburg, Germany, (1989) 476–479.

2.62. M. Krunks, O. Kijatkina, H. Rebane, I. Oja, V. Mikli, A. Mere, “Composition of CuInS2 thin films prepared by spray pyrolysis”, Thin Solid Films 403 (2002) 71–75.

2.63. S. Marsillac, M.C. Zouaghi, J.C. Bernede, T. Ben Nasrallah, S. Belgacem, “Evolution of the properties of spray deposited $CuInS_2$ thin films with post-annealing treatment”, Solar Energy Materials and Solar Cells 76 (2003) 125–134.

2.64. C. J. Hibberd, E. Chassaing, W. Liu, D.B. Mitzi, D. Lincot, A.N. Tiwari, “Non-vacuum methods for formation of Cu(In, Ga)(Se, $S)_2$ thin film photovoltaic absorbers”, Progress in Photovoltaics: Research and Applications 18 (2010) 434–452.

2.65. D.B. Mitzi, M. Yuan, W. Liu, A.J. Kellock, S.J. Chey, V. Deline, A.G. Schrott, “A High-Efficiency Solution-Deposited Thin-Film Photovoltaic Device”, Advanced Materilas 20 (2008) 3657–3662.

2.66. W. Liu, D.B. Mitzi, M. Yuan, A.J. Kellocks, S.J. Chey, O. Gunawan, “12% Efficiency $CuIn(Se,S)_2$ Photovoltaic Device Prepared Using a Hydrazine Solution Process”, Chemistry of Materials 22 (2010) 1010–1014.

2.67. D. Zhao, Q. Tian, Z. Zhou, G. Wang, Y. Meng, D. Kou, W. Zhou, D. Pan, S. Wu, “Solution-deposited pure selenide CIGSe solar cells from elemental Cu, In, Ga, and Se”, Journal of Materials Chemistry A 3 (2015) 19263-19267.

2.68. K.H. Kim, Y.G. Chun, B.O. Park, K.H. Yoon, “Synthesis of $CuInSe_2$ and CIGSe nanoparticles by solvothermal route”, Materials Science Forum, 449-452 (2004) 273-276.

2.69. Y.G. Chun, K.H. Kim, K.H Yoon, “Synthesis of CIGSe nanoparticles by solvothermal route”, Thin Solid Films 480–481 (2005) 46–49.

2.70. S.H. Mousavi, T.S. Müller, P.W. de Oliveira, “Synthesis of colloidal nanoscaled copper–indium–gallium–selenide (CIGS) particles for photovoltaic applications”, Journal of Colloid and Interface Science 382 (2012) 48–52.

2.71. K.H. Kim, Y. G. Chun, K.H. Yoon, “Synthesis of CIGSe nanoparticles by low temperature colloidal route” Journal of Mechanical Science and Technology 19 (2005) 2085-2090.

2.72. X. Cui, D. Yun, C. Zhong, W. Chen, Q. Cheng, J. Feng, F. Zhang, “A facile route for synthesis of $CuIn_xGa_{1-x}Se_2$ nanocrystals with tunable composition for photovoltaic application, Journal of Sol-Gel Science and Technology 76 (2015) 469-475.

2.73. C. Suryanarayana, E. Ivanov, R. Noufi, M.A. Contreras, J.J Moore, “Phase selection in a mechanically alloyed Cu-In-Ga-Se powder mixture” Journal of Material Research,14 (1999) 377-383.

2.74. B. Vidhya, S. Velumani, R. Asomoza, “Effect of milling time and heat treatment on the composition of $CuIn_{0.75}Ga_{0.25}Se_2$ nanoparticle precursors and films”, Journal of Nanoparticle Research 13 (2011) 3033-3042.

2.75. L. Fu, Y.Q. Guo, S. Zheng, “X-Ray diffraction studies on the effect of ball-milling speed on the structure of $Cu(In,Ga)Se_2$ nanoparticles”, Powder Diffraction 28 (2013) S 28-S 31.

2.76. L. Ying, K. Deyi, “Preparation of $Cu(In,Ga)Se_2$ thin film by non-vacuum mechanochemical and spin-coating process”, IEEE- Asia-Pacific Power and Energy Engineering Conference (2011) 1-4.

2.77. T. Wada, Y. Matsuo, S. Nomura, Y. Nakamura, A. Miyamura, Y. Chiba, A. Yamada, M. Konagai, “Fabrication of $Cu(In,Ga)Se_2$ thin films by a combination of mechanochemical and screen-printing/sintering processes”, Physica Status Solidi A 203 (2006) 2593-2597.

2.78. Y. Yin, A.P. Alivisatos, “Colloidal nanocrystal synthesis and the organic-inorganic interface”, Nature 437 (2005) 664-670.

2.79. C.P. Liu, C.L. Chuang, “Fabrication of CIGS nanoparticle-ink using ball milling technology for applied in CIGS thin films solar cell”, Powder Technology 229 (2012) 78-83.

2.80. M.V. Kovalenko, M. Scheele, D.V. Talapin, “Colloidal nanocrystals with molecular metal chalcogenide surface ligands”, Science 324 (2009) 1417-1420.

2.81. S. Ahn, K. Kim, K. Yoon, “Cu (In, Ga) Se_2 thin film solar cells from nanoparticle precursors”, Current Applied Physics 8 (2008) 766-769.

2.82. J.H. Chung, S.J. Kim, “Colloidal precursors from ball-milling in liquid medium process for $CuInSe_2$ thin film”, Bulletin of Korean Chemical Society 31 (2010) 2695-2697.

2.83. Y. Liu, D. Kong, H. You, C. Zhao, J. Li, J. Brugger, “Fabrication of Cu(In, Ga)Se_2 thin films from nanoparticles by non- vacuum mechanochemical method and rapid thermal annealing process”, ECS Solid State Letters. (2012) 26-28.

2.84. H. Matsushita, T. Takizawa, “Phase diagram of the CuIn–2Se system for $CuInSe_2$ crystal growth by controlling Se contents”, Journal of Crystal Growth 179 (1997) 503-509.

2.85. J. Shen, W.K. Kim, S. Shang, M. CHU, S. CAO, T.J. Anderson, “Thermodynamic description of the ternary compounds in the Cu–In–Se system”, Rare Metals 25 (2006) 481-487.

2.86. Q. Guo, G.M. Ford, H.W. Hillhouse, R. Agrawal, “Sulfide nanocrystal inks for dense $Cu(In_{1-x}Ga_x)(S_{1-y}Se_y)_2$ absorber films and their photovoltaic performance”, Nano Letters 9 (2009) 3060-3065.

2.87. F. Hergert, S. Jost, R. Hock, M. Purwins, J. Palm, “Formation reactions of chalcopyrite compounds and the role of sodium doping”, Thin Solid Films 515 (2007) 5843-5847.

2.88. Y. Xiang, X. Zhang, S. Zhang, “Insight into the mechanism of Sb promoted $Cu(In,Ga)Se_2$ formation”, Journal of Solid State Chemistry 204 (2013) 278-282.

2.89. M. Yuan, D.B. Mitzi, W. Liu, A.J. kellock, S. Jay chey and Vaughn R Deline, “Optimization of CIGS-based PV device through Antimony doping” Chemistry of Materials 22 (2010), 285-287.

2.90. M. Yuan, D.B. Mitzi, W. Liu, A.J. Kellock, S.J. Chey, V.R. Deline, “Antimony assisted low temperature processing of CIGSeS solar cells” Thin Solid films 519 (2010) 852-856.

2.91. F.S. Chen, J.S. Ma, J.C. Sung, C.H. Lu, “Bismuth –ion doped $Cu(InGa)Se_2$ thin films: Preparation, microstructures and electrical properties”, solar energy materials and solar cells, 124 (2014) 166-171.

2.92. B. Walker, R. Agrawal, “Grain growth enhancement of selenide CIGSe nanoparticles to densified films using copper selenides”, Photovoltaic Specialists Conference (PVSC), 38 th IEEE (2012) 002654-002657.

2.93. A.E. Zaghi, M. Buffiere, J. Koo, G. Brammertz, M. Batuk, C. Verbist, J. Hadermann, W. K. Kim, M. Meuris, J. Poortmans, J. Vleugels, “Effect of selenium content of $CuInSe_x$ alloy nanopowder precursors on recrystallization of printed $CuInSe_2$ absorber layers during selenization heat treatment”, Thin Solid Films 582 (2015) 11-17.

CHAPTER - 3

EXPERIMENTAL AND CHARACTERIZATION TECHNIQUES

This chapter describes the detailed explanation of experimental methods and characterizations used in the execution of the present research work. The chapter content starts with preparation of CIGSe powder, ink formulation, film deposition, post deposition heat treatment of the film and formation of CIGSe-based Mo/CIGSe/CdS/Au heterojunction structure. Later, the physical principle behind the basic characterization techniques used in this study is described. Theory of photovoltaic device including efficiency calculations is mentioned at the end.

As referred to in section 2.3.2.2.3, CIGSe film preparation using particle-based method involves four steps: (i) Synthesize of CIGSe particles, (ii) formulation of ink using CIGSe particle, (iii) deposition of CIGSe film, and (iv) post-deposition heat treatment of the film.

3.1 Synthesis of CIGSe powder

As mentioned in the section 2.3.2.2.3, in this work, CIGSe particles are synthesized by the mechanochemical process. A brief description about the mechanochemical process and important process variables are discussed below.

3.1.1 Mechanochemical Synthesis

Mechanical alloying is a solid-state powder processing technique developed by John Benjamin and his colleagues at the Paul D.Merica Research Laboratory of the International Nickel Company (INCO) during 1966 [3.1]. It is a high-energy ball milling technique that involves repeated welding, fracturing, and rewelding of powder particles [3.2]. Plenty of scientifically relevant materials has been produced using this method. The formation of an amorphous phase in Y-Co intermetallic compound by metallic grinding and in the Ni-Nb system by ball milling of powder mixture gave mechanical alloying the recognition of ‘potential non-equilibrium processing technique’ [3.2, 3.3]. The recognition of the possibility of mechanically induced chemical reaction in powder

mixture made this process more interesting. Mechanochemical synthesis is a general term given to the mechanical alloying process in which chemical reaction takes place during milling of metal powders. The important attributes of mechanochemical synthesis process are:

1) Production of fine dispersion of second phase (usually oxide) particles
2) Extension of solid solubility limits
3) Refinement of grain sizes down to nanometer range
4) Synthesis of novel crystalline and quasicrystalline phases
5) Combustion reactions
6) Refining of metals
7) Possibility of alloying of difficult to alloy elements
8) Inducement of chemical (displacement) reactions at low temperatures
9) Scalable process [3.2]

3.1.1.1 The process of Mechanochemical synthesis

Mechanochemical synthesis initiates with the loading of powder mix of constituent elements in the required proportion into the milling vial along with the grinding medium. Then the mix is milled until a steady state is reached. The steady state here refers to when the composition of every powder particle is the same as the proportion of the elements in the initial powder mix. Hence the principal components of the mechanochemical process are raw materials, type of mill and process variables. It includes milling speed, milling time, ball to powder ratio, milling container, type of mill, the size of the grinding medium, the extent of milling, milling atmosphere, temperature of milling and process control agent. Raw materials used for this process could be pure metals, alloys, pre- alloyed powders and refractory compounds. The particle size of the precursors is not very important unless it is smaller than the size of grinding media (grinding balls) as the raw material powder size will decrease exponentially with milling time and reaches a few microns within a few minutes of milling. The material used for milling container is significant because the powder may get contaminated with the material driven out from the inner walls of the container due to the collision of milling media during the milling process. Commonly used materials for grinding vessels are hardened steel, hardened chromium steel, tempered steel, stainless steel,

WC-Co, WC-lined steel and bearing steel. The material used for grinding medium is also important. The typical material used for grinding medium are hardened steel, tool steel, hardened chromium steel, tempered steel, stainless steel, WC-Co, and bearing steel. There are different types of milling equipment with differing in capacity, the efficiency of milling and arrangements for cooling and heating. A few of different milling models for the mechanochemical process are SPEX shaker mills, planetary ball mills, attritor mills, etc [3.2]. Type of Mill has to be chosen carefully according to the application. The mechanism of a planetary ball mill is given in detail below.

Planetary ball mill is one among the popular mill to carry out mechanochemical process. The name planetary ball mill comes due to planet like a movement of its vials. It consists of jars arranged on a rotating support disk (figure 3.1 (A)). During milling, the rotating disk will rotate around its axis due to unique driving mechanism. The centrifugal force produced by both the rotational motion of vials around its own axis and the rotational motion of support disk act on the vial content (i.e. loaded material to be grounded and the grinding balls). The direction of centrifugal force changes alternatively as the vials and supporting disc rotate in the opposite direction. This makes the grinding balls run down inside the wall of the vial (friction effect) followed by the material being ground and grinding balls lifting off and travelling freely through the inner chamber of the vial and colliding against the opposing inside wall (the impact effect) [3.2]. The schematic of ball motion inside the ball mill is shown in figure 3.1(B).

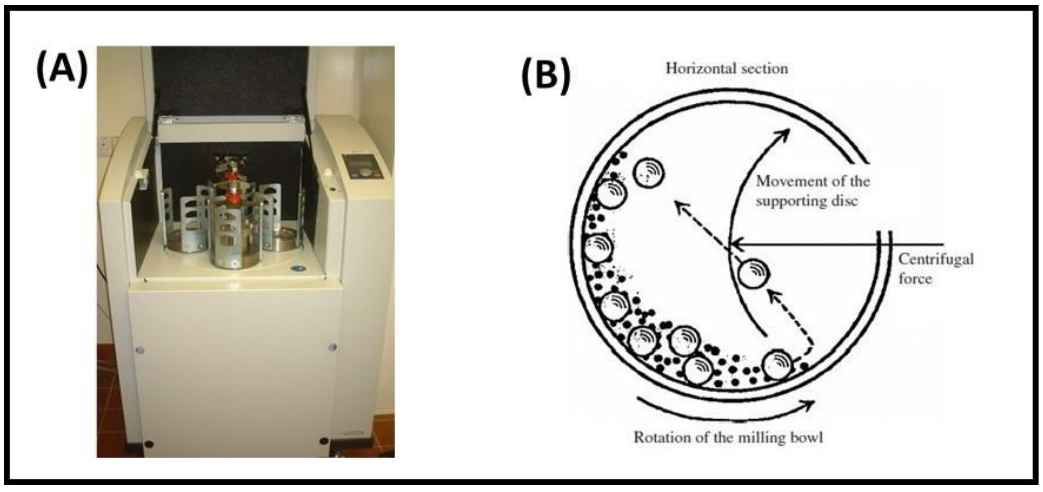

Fig.3.1. (A) Fritsch pulversite planetary mill (B) schematic representation of ball motion inside the ball mill [3.2].

3.1.1.2 The mechanism of mechanochemical synthesis

The particles loaded to the vial are repeatedly flattened, cold welded, fractured and rewelded during high-energy milling. When two balls collide each other, it traps some amount of powder in between them as shown in figure 3.2. As force of impact plastically deforms the powder particle, eventually it gets works hardened and fractured. The newly formed surfaces facilitate the particles to weld together which in turn leads to increase in particle size. At this stage, the milled particles have a broad range of particle size with a layered structure consisting of different combinations of the starting materials.

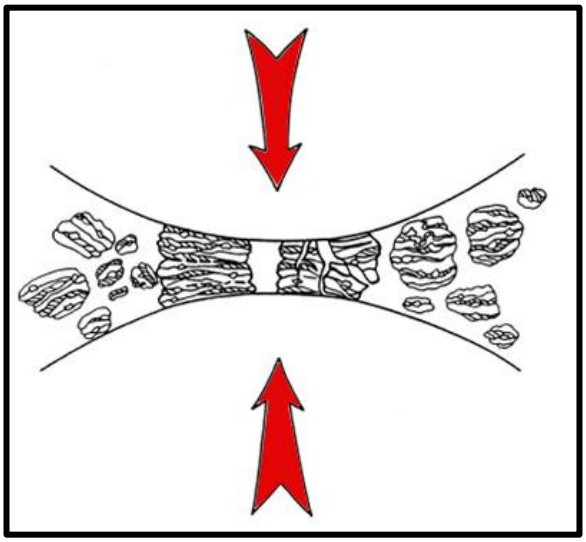

Fig.3.2. Ball- powder-ball collision during mechanochemical process [3.2].

As the milling proceeds, the deformation process continues. Thus, the particles get work hardened and fractured due to fatigue failure mechanism or by fragmentation of flakes. The formed fragments may continue to decrease in size in the lack of agglomerating forces. At this stage, the tendency to fracture prevails over cold welding. The structure of particles is steadily refined because of a continued impact of grinding balls, even though there is no significant reduction in particle size. Therefore, it results in a decrease in the interlayer spacing and increase in the number of layers. As the milling time progresses, a steady–state equilibrium is reached where as a balance is obtained between the rate of welding and the rate of fracturing. At this stage, each particle consists of the constituent elements in the starting proportion. The

particles attained saturation hardness owing to the accumulation of strain energy. The particle size distribution gets narrower as particles larger than average size reduces their size at the same rate as the smaller fragments grow by agglomeration.

During the mechanochemical process, deformation is introduced into the particles through crystal defects such as dislocations, vacancies, stacking faults and increased number of grain boundaries. This defect structure aids for proper alloying by enhancing the diffusivity of the elements into the matrix. Also, the properties of refined microstructure particles are such that it decreases the diffusion distance. Moreover, a small increase in temperature of the vial during milling assists the diffusion behaviour. Thus, constituent elements alloy properly [3.2, 3.4, 3.5].

3.1.2 Experimental details of the mechanochemical synthesis of CIGSe powder

In our case, the CIGSe powder was synthesized by a Retsch PM 400 planetary ball milling equipment shown in figure 3.1 (a). Elemental Copper (> 99.90 pure, Aldrich), Indium (>99.99 pure, Aldrich), Gallium (>99.99 pure, Aldrich) and Selenium (>99.99 pure, Aldrich) were used as precursor materials. Tungsten Carbide vial is used as the container and 10 mm diameter Tungsten Carbide balls weighing 7.738 g are used as milling media.

At first, $Cu(In_{0.5},Ga_{0.5})Se_2$ powder is synthesized and milling parameters (ball to powder ratio (BPR), milling speed and milling time) are optimized to obtain a single phase $Cu(In_{0.5},Ga_{0.5})Se_2$ powder. The reaction underwent in mechanochemical process to form $Cu(In_{0.5},Ga_{0.5})Se_2$ is as follows:

$$Cu + 0.5\,In + 0.5\,Ga + 2\,Se \xrightarrow{BPR,Milling\ speed,Milling\ time} Cu(In_{0.5}, Ga_{0.5})Se_2 \qquad \text{(Eq. : 3.1)}$$

Milling parameters are varied systematically to optimize the milling conditions and are given in table 3.1. To start with, a BPR of 15:1 and milling speed of 400 rpm (revolutions per minute) are selected while milling time is varied from 0.5 to 6 h.

Eventually, BPR is increased to 20:1 and further to 25:1 to find out BPR for synthesizing single phase $Cu(In_{0.5},Ga_{0.5})Se_2$ in minimum milling duration. Subsequently, the effect of milling speed on structural, morphological and compositional properties is studied by varying the speed from 200 to 400 rpm with an interval of 50 rpm.

Table 3.1. Experimental design to optimize ball milling parameters.

Trial	Ball to powder ratio (BPR)	Milling time (h)	Milling speed (rpm)
1	15:1	0.5	400
2	15:1	1	400
3	15:1	1.5	400
4	15:1	2	400
5	15:1	4	400
6	15:1	6	400
7	20:1	1	400
8	25:1	1	400
9	20:1	2	400
10	25:1	2	400
11	25:1	2	350
12	25:1	2	300
13	25:1	2	250
14	25:1	2	200

Later, the optimum milling condition is used to synthesize $Cu(In_{0.5},Ga_{0.5})Se_2$ powder as $Ga/(In+Ga) \leq 0.3$ is experimentally proved as optimum for good photovoltaic conversion efficiency [3.6]. Then, to study the effect of Se content in the CIGSe powder on the morphological properties of the film, $Cu(In,Ga)Se_{1.5}$, $Cu(In,Ga)Se_1$ and $Cu(In,Ga)Se_{0.5}$, powders are also synthesized using the optimum ball milling parameters.

3.2. CIGSe particle-based ink formulation

Particle-based ink is formulated using mechanochemically synthesized CIGSe particles to deposit the films over the substrate. Ink formulation process involves dispersion of particles in a solvent with the aid of suitable organic binders and dispersing agents. In this work, CIGSe ink is formulated by dispersing the particles in Ethanol (anhydrous, Aldrich) with the addition of Ethyl Cellulose (Ethoxy content 48 %, Aldrich) and Terpineol (anhydrous, Aldrich). Ethyl cellulose and Terpineol are chosen as the binder and dispersing agent. The different steps followed to formulate CIGSe ink are

1. Dispersing 1.5 g of CIGSe particle in 45 ml of ethanol by ultrasonication for 1h (Solution 1).
2. Dissolving ethyl cellulose and terpineol in 11 ml of ethanol at 190 rpm and 160 ˚C (Solution 2).
3. Mix solution 1 and 2 and ultrasonicated for 1h.

The content of Ethyl Cellulose and Terpineol in ink are varied from 0 to 4 wt% and 0 to 40 wt% for the better understanding of their role on the stability of ink.

3.3. *CIGSe film deposition*

3.3.1. Substrate

The important properties of a substrate material include chemical stability, temperature stability, and thermal expansion coefficient. Chemical stability of substrate is important to prevent interdiffusion of material between film and substrate. Temperature stability is necessary to carry out deposition process at high temperature. A small mismatch in thermal expansion coefficient between substrate and film is needed to the thermal stress of deposited films. Soda- lime glass (SLG) is the standard substrate used in high-efficiency CIGSe solar cells. Soda lime glass is chemically stable, relatively economical, and relatively hard and exhibits smooth surface. It has sufficient glass transition temperature (Tg) of 563 ˚C and thermal expansion coefficient of 9.5 ppm/K.

Another advantage of using SLG as the substrate is that Na from SLG diffuse to CIGSe during the deposition process and improves the electrical properties [3.7].

3.3.2. *Cleaning of substrate*

The condition of the substrate before film deposition is very necessary for proper film adhesion. Also, substrate cleaning has significant role on film growth characteristics [3.8].

The substrate cleaning process involves several steps which are as follows.

1. Initially, substrates are cleaned ultrasonically with soap solution for 5 min.
2. Ultrasonically agitated in distilled water for 10 min. Shock waves created in the solvent rendered the possible removal of residues.
3. Thoroughly rinsed with Ethyl alcohol in an ultrasonic bath for 10 min, which is followed by ultrasonic agitation in distilled water for 5 min.
4. Subjected to ultrasonic agitation in acetone for 10 min to remove any other dirt followed by ultrasonic agitation in distilled water for 5 min.
5. Surface treatment of the cleaned substrates is carried out in a solution of H_2SO_4 (> 95%, Aldrich) and H_2O_2 (50%, Botica Moderna) (2:1) for 2 to 3 min.
6. Finally, the substrates are dried using nitrogen gas.

3.3.3. *CIGSe film deposition by "doctor blade" technique*

Before the coating of ink, the viscosity of the ink is adjusted by evaporating ethanol to make it suitable for doctor blade deposition. Before the deposition of ink onto the substrate, the substrate is covered with a stainless-steel mask of 3 μm thick. The mask acts as a spacer and film is deposited by dripping a single drop of ink on the free space of substrate and whipping the ink over the substrate by a knife (figure 3.3). Besides, the mask acts as a thickness controller. Films are dried at 90 ˚C on a hot plate soon after deposition previous to post-deposition annealing treatments.

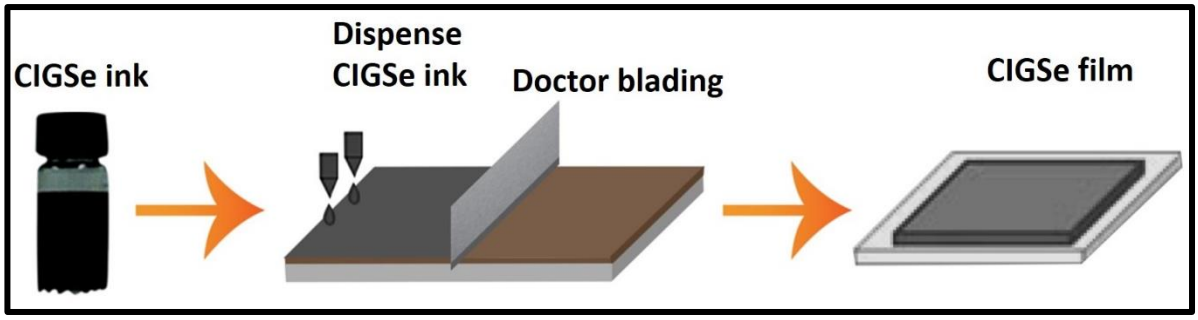

Fig.3.3. Schematic of CIGSe film deposition by doctor- blade technique.

3.4. *Annealing of CIGSe film*

As-deposited films are subjected to post-deposition heat treatments in two steps. (i) Annealing at low temperature and (ii) annealing at high temperature in Se atmosphere (selenizaiton). Low-temperature annealing of the films are carried out in an ambient atmosphere at different temperatures 300 and 400 ˚C for 1 h. The furnace used for air annealing is shown in figure 3.4. The furnace consists of a quartz tube to place the sample, a resistive heater and a temperature controller.

Fig.3.4. Home-made furnace used for air annealing.

High-temperature annealing process was carried out in selenium atmosphere using partially closed graphite box. The Se powder (50 mg) was introduced into the graphite box along with sample and loaded into the furnace. Figure 3.5 shows the photograph of furnace (3.5 (A)) and graphite box (3.5 (B)). A two- step selenization process was carried out in Ar atmosphere. The process includes annealing the sample to 400 ºC for 30 minutes at 1.6 torr and then to 550 ˚C for 15 minutes at 760 torr. The first step facilitates incorporation of Se to the CIGSe layer at 400 ˚C whereas the second step

involves selenization and recrystallization process. The ramp of temperature was 20 ˚C/min.

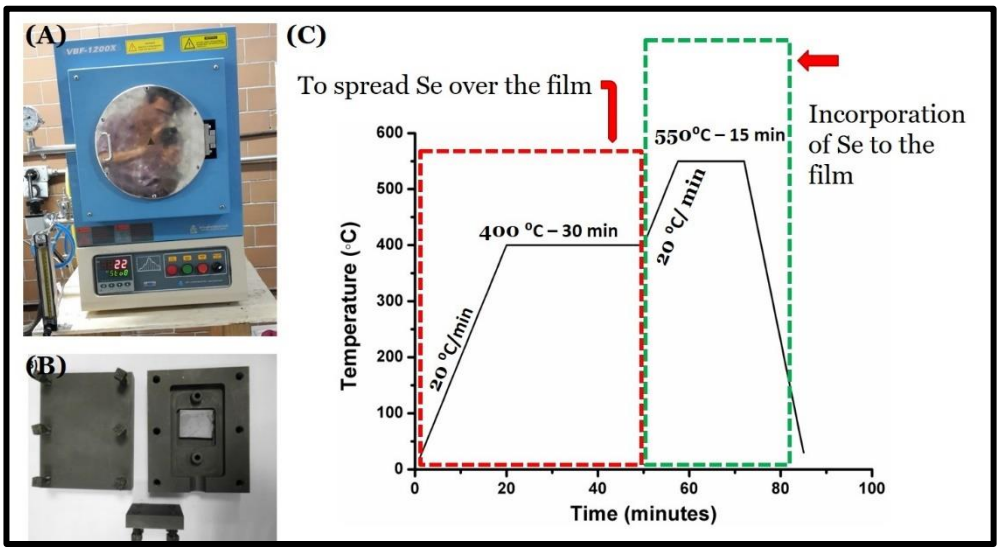

Fig.3.5. Photograph of (A) furnace (B) graphite box and (c) temperature profile of selenization.

3.5. *Fabrication of SLG/Mo/CIGSe/CdS/Au Heterojunction structure (2×2 cm^2)*

A CIGSe-based solar cell is a heterojunction system consisting of Molybdenum (Mo) back contact, p-type CIGSe absorber layer, CdS buffer layer, an intrinsic ZnO layer (iZnO), and Al: ZnO transparent front contact. A typical CIGSe thin film solar cell structure in substrate configuration is given in figure 3.6. A heterojunction is formed between CIGSe and CdS/iZnO/Al: ZnO layers. Metalic Ni/Al contact grids are used to complete the cell [3.9].

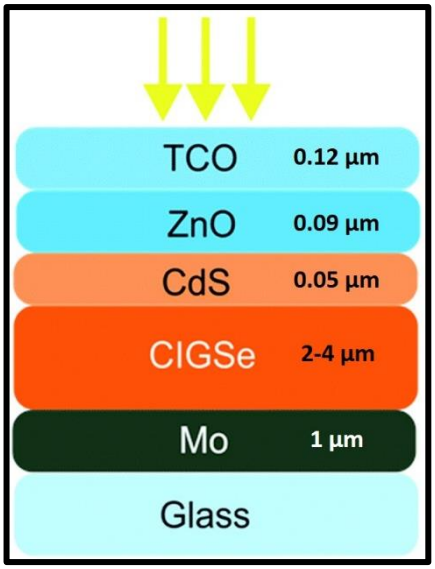

Fig.3.6. Schematic of typical CIGSe-based solar cell structure deposited over Mo coated SLG glass substrate [3.9].

The band diagram of CIGSe-based solar cell is shown in figure 3.7. ZnO and CdS has wider bandgap and allows photons to be absorbed in the narrow bandgap CIGSe layer. Photogenerated electron-hole pairs generated in CIGSe layer are separated by the built-in potential developed in the heterojunction and contribute to the photocurrent. A discontinuity in conduction band ΔEc is developed at the CIGSe/CdS heterojunction interface due to the difference in electron affinity between CIGSe and CdS [3.10].

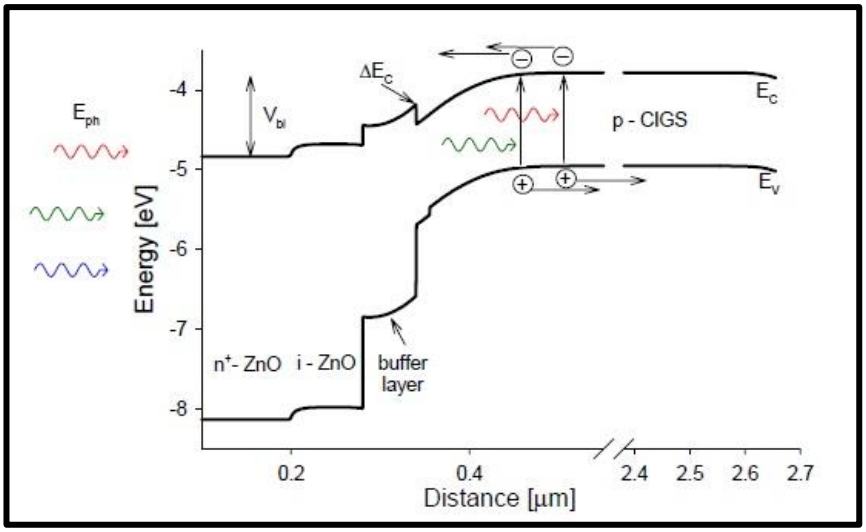

Fig.3.7. Schematic of band diagram of CIGSe-based thin film solar cell [3.10].

However, in the present work, SLG/Mo/CIGSe/CdS/Au structure is fabricated (figure 3.8) to explore the photovoltaic application of the prepared CIGSe films. This structure is used in this study following the work of Jagadeesh [3.11].

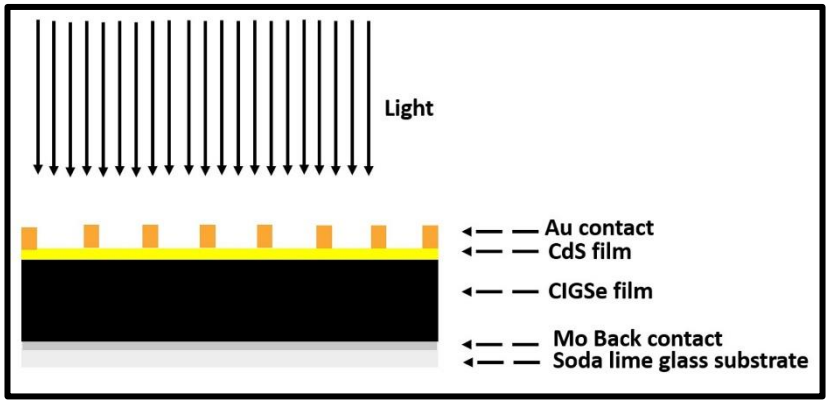

Fig.3.8. Schematic of fabricated SLG/Mo/CIGSe/CdS/Au heterojunction structure [3.11].

The details of deposition methods used for deposition of CdS thin film, Mo, and Au contacts are described below.

a) Deposition of Mo layer

In this work, we use SLG/Mo substrate obtained from CINVESTAV, Merida. The Molybdenum back contact layer is deposited on the soda-lime glass substrate using d.c. sputtering technique. The Mo deposition is performed in CINVESTAV-Merida. Mo layer acts as the back contact and reflects most of the unabsorbed light back to the CIGSe absorber layer [3.12]. The thickness of Mo layer is 777 nm which in the range (500-900 nm) used in high-efficiency solar cells [3.13]. The sheet resistance of Mo film is 0.35 Ω/square which is higher than the required sheet resistance (< 0.24 Ω/square) as reported by Repins et .al [3.14].

***b)* Deposition of CIGSe film**

CIGSe film is deposited over SLG/ Mo layer by doctor blade coating of ink as explained in section 3.1 to 3.4.

c) Deposition of CdS film

CdS has n-type conductivity. It serves as the buffer layer in CIGSe solar cells [3.14]. CdS film of approximately 50 nm thick was deposited using chemical bath deposition (CBD) method. The experimental process of CdS deposition is carried out in ESFM - IPN using the reagents and deposition conditions reported by Fabian [3.15].

Cadmium Chloride and Thiourea were used as sources of Cd and S respectively. Ammonium Chloride is used as a buffer, and Ammonium Hydroxide is used as the complexing agent. Deionized water is used as the solvent.

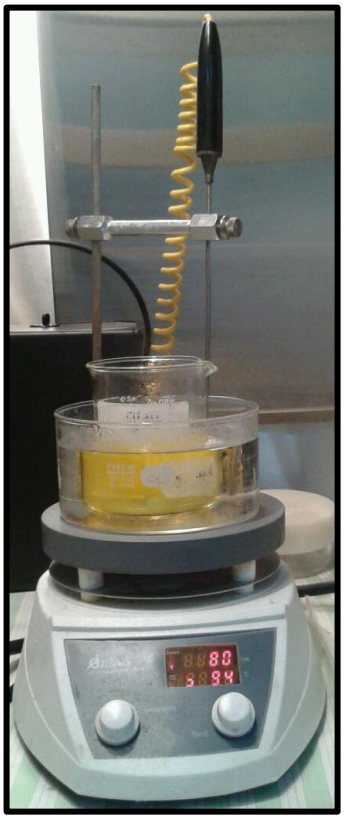

Fig.3.9. Photograph of chemical bath deposition of CdS thin film.

Figure 3.9 shows experimental set up of CBD. It consists of two beakers. The larger beaker contains tap water, and smaller beaker contains chemical bath. Large beaker is placed on the stirrer and heated at 94 ˚C. 5 ml of 0.12 M $CdSO_4$, 10 ml of 0.2 M NH_4Cl,20 ml of 28% NH_4OH solutions are added to 45 ml of deionized water taken in the smaller beaker. Later, the small beaker is kept in the water bath, and CIGSe film is immersed in the chemical bath. Chemical bath solution is stirred throughout the experiment for homogenizing the mixture. Later, 10 ml 0.3 M Thiourea solution is added to the small beaker. Then, Cd^{2+} and S^{2-} ions will release slowly from the solution and condenses on an ion-ion basis on the substrate.

National Renewable Energy Laboratory (NREL) performed a study on thickness of CdS layer versus CIGSe solar cell performance. It shows that solar cell efficiency

increases with increasing CdS thickness upto 40-50 nm and then decreases as absorption in CdS increases [3.16]. Hence we optimised the thickness of CdS layer on glass substrate by varying deposition time from 5 min to 12.5 min. The thickness of CdS layer as a function of deposition time is shown in figure 3.10. 68 nm thick CdS film is obtained with deposition time of 5 min. It should be noted that, thickness of CdS film will be reducing while depositing on CIGSe by10-15 nm. Hence, duration of chemical bath deposition is fixed as 7.5 min for deposition of CdS over CIGSe film.

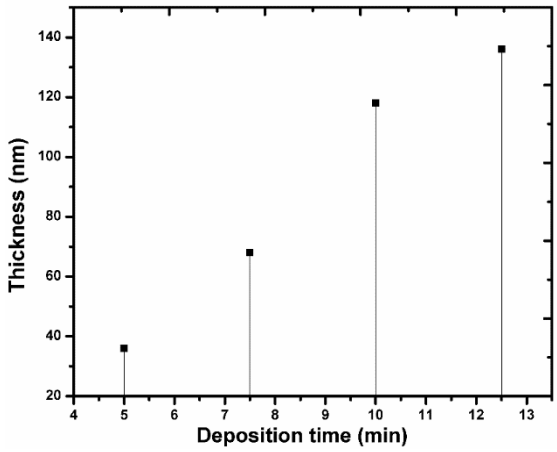

Fig.3.10. Variation in thickness of CdS film as a function of deposition time.

UV-Visible transmittance spectrum of CdS film deposited for 7.5 min is shown in figure 3.11 (A). It shows 50% transmittance for wavelength more than 450 nm and more than 75% of transmittance for wavelength above 550 nm. Tauc method is used to determine the optical bandgap of CdS film. The extrapolation of linear portion of the curve in figure 3.8 (B) to $(\alpha h\nu)^2=0$ gives estimated value of bandgap as 2.42 eV. This is in match with the previously reported bandgap values [3.17,3.18].

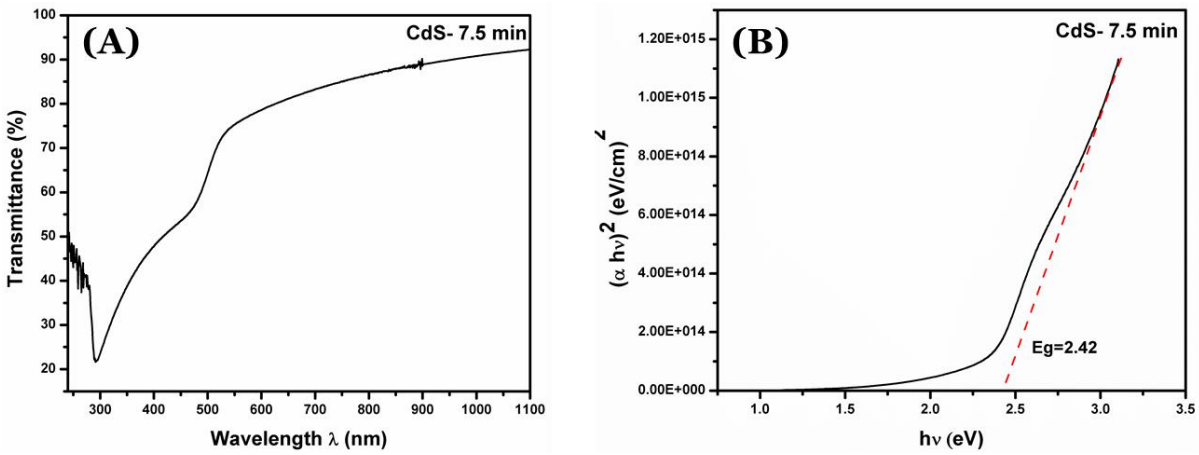

Fig.3.11. (A) Transmittance spectrum and (B) bandgap of CdS thin film deposited for 7.5 minutes.

d) Deposition of Au contact

Finger shaped Gold (Au) contact of area 0.105 cm^2 and thickness of 500 nm is deposited on SLG/Mo/CIGSe/CdS structure of 0.5 cm^2 by evaporation process.

3.6. Characterization techniques:

3.6.1. X-Ray Diffraction Analysis (XRD)

XRD is a powerful rapid non-destructive analytical technique primarily for characterizing crystalline materials. XRD of sample is obtained using X-ray diffractometer. Schematic of X-ray measurement system is shown in figure 3.12(a). X-ray diffractometer primarily consists of three parts namely X-ray tube, sample holder and X-ray detector. X-rays are generated in a cathode ray tube due to the impact of accelerated electrons produced by heating filaments on the target (generally Mo target). These X- rays are filtered by foils or crystal monochromators to produce monochromatic X rays required for diffraction. The monochromatic X-rays are then collimated and directed towards the sample. When the interaction of incident X-ray with the sample satisfies Braggs law, $n\lambda = 2dsin\theta$ (where n, λ, d and θ are order of diffraction, wavelength of incident X ray, interplanar distance and angle of incidence respectively) constructive interference occurs. The diffracted X-rays are recorded, processed and converted into count rate by detector which is then given to computer monitor. XRD pattern consist of diffraction peaks based on constructive interference of a monochromatic beam of x-rays scattered from specific angles from each set of

lattice planes in a sample. So, XRD pattern is the finger print of atomic arrangements in a given crystal material [3.19].

Crysallite size of CIGSe powder is calculated from X-ray diffraction spectra using Scherrer formula

$$D = \frac{0.94\lambda}{\beta \cos\theta} \qquad \text{(Eq. : 3.2)}$$

Where, β is the full width at half maximum (FWHM) of intensity of diffracted peak at the Bragg's angle θ and λ is the wavelength of X-ray.

In present work, CIGSe powder and films are analysed using Xpert-Pro Pananalytical X-ray Diffractometer from SEES which is shown in figure 3.12(b). XRD analysis is performed with CuKα (λ=1.54 Å) in the θ-2θ mode with step size of 0.039.

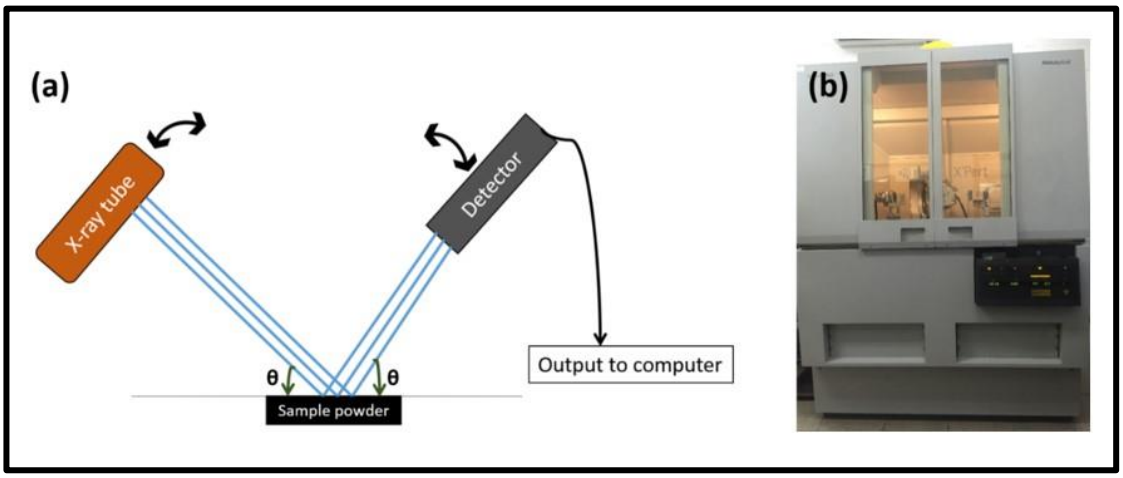

Fig.3.12. (a) Schematic of XRD measurement system [3.11] and (b) photograph of Xpert-Pro Pananalytical X-ray diffractometer.

3.6.2. Raman Scattering

Raman scattering is a powerful, convenient and non-destructive tool to characterize crystalline, polycrystalline and amorphous materials which applies Raman Effect. It is a second order inelastic scattering process. A laser source is used as light source. The monochromatic light from the laser is focused on to the sample through a confocal microscope. The laser beam interacts with sample and originates a scattered light. Much of the scattered light has frequency equal to incident laser beam and known as Reyleigh scattering. A small fraction of scattered radiation has frequency different from

the incident laser beam and constitutes Raman scattering. The scattered light is collected and directed to the spectrograph to generate Raman spectrum. When frequency of incident radiation is higher than the frequency of scattered light stockes lines appear in the Raman spectrum. Whereas, if the frequency of incident laser beam is lower than the frequency of scattered light anti-stockes lines appear in Raman spectrum. Raman spectrum of the material is presented as a plot of scattering light intensity versus shift of frequency of incident light. Raman spectrum is strongly dependent on the material to be analysed and its crystalline phases and it is independent of frequency of incident radiation. Hence it gives information on crystalline phases and composition of the material [3.20].

Tetragonal chalcopyrite structure of $CuInSe_2$ has 3 acoustic and 21 optical phonon modes. The phonon modes are represented by $\Gamma_{ac} = 1B_2 + 1E$ for acoustic modes and $\Gamma_{opt} = 1A_1 + 2A_2 + 3B_1 + 3B_2 + 6E$ for optical modes. Among optical modes, A_1, B_1, B_2 and E modes are Raman active. B_2 and E modes are infrared active if the incident radiation is polarised parallel and perpendicular to the tetragonal C-axis of the crystal. A_2 phonon modes are inactive. Different modes of $CuInSe_2$ (CISe) and $CuGaSe_2$ (CGSe) are tabulated in table 3.2. Optical modes of CIGSe lies between that of CISe and CGSe depending on Ga/(In+Ga).

Table 3.2. Different optical phonon modes of CISe and CGSe.

Modes	CISe [3.21]	CGSe [3.22]
A_1	169	180
B_1^3	81	90
B_1^2	149	108
B_1^1	206	128
B_2^3	67/68	81/102
B_2^2	173/182	200/202
B_2^1	197/210	259/261
E^6	60/60	62.5/73
E^5	69/69	80.5/83.5
E^4	132/132	117/121
E^3	171/174	141/142
E^2	193/197	183/193
E^1	199/211	252/277

In the present work, Raman dispersion studies were made in Horiba–Jobin Yvon-LabRAM HR800 equipment from SEES as shown in figure 3.13, with He-Ne laser operated at 632 nm of 20 mW. To avoid heating of the sample and to filter plasma frequencies a D0.6 filter was employed which reduces power to 5 mW.

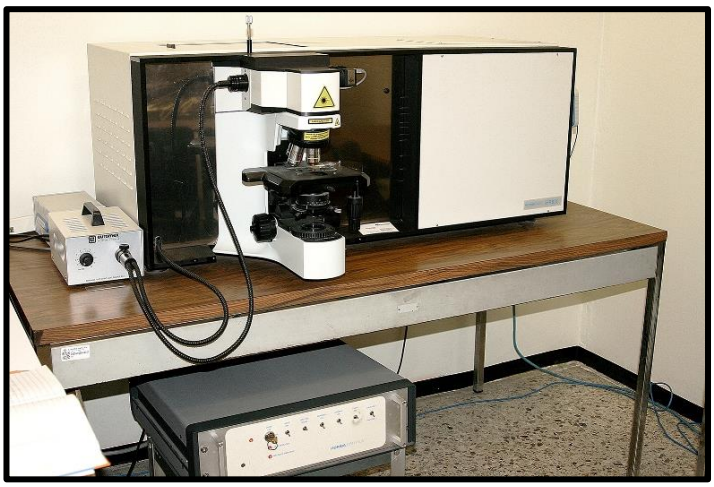

Fig.3.13. Horiba Jobin-Yuvan Raman spectrometer.

3.6.3. Field Emission Scanning Electron microscopy

Field Emission Scanning Electron Microscopy (FESEM) is the most versatile instrument available for the examination of microstructural characteristics of solid objects. The basic components of FESEM are the lens system, electron gun, electron collector, visual and recording cathode ray tubes and the electronics associated with them. Electron gun in FESEM is a field emission gun. Field emission gun consists of emitter (cathode) and anode. Cathode is several kilovolts negative with respect to anode. The high potential gradient at the emitter surface cause for field electron emission. The emitted electron beam is focussed by the electromagnetic lens system and apertures to a small spot on the object. The interaction of electron beam with the specimen can result in liberation of secondary electrons, backscattered electrons, auger electrons, X-rays and cathodoluminescence. Among this, energy of secondary electron is around 5 eV. Hence, secondary electrons from the surface of specimen can only be detected. The angle and velocity of emitted secondary electron depends on the surface of the specimen. These secondary electrons are detected by a detector and produces electronic signal which can be amplified and transformed to scan the image [3.23].

In this study, Carl Zeiss HRSEM-AURIGA microscope (figure 3.14) from LANE is used for analysing morphology of CIGSe powder and films.

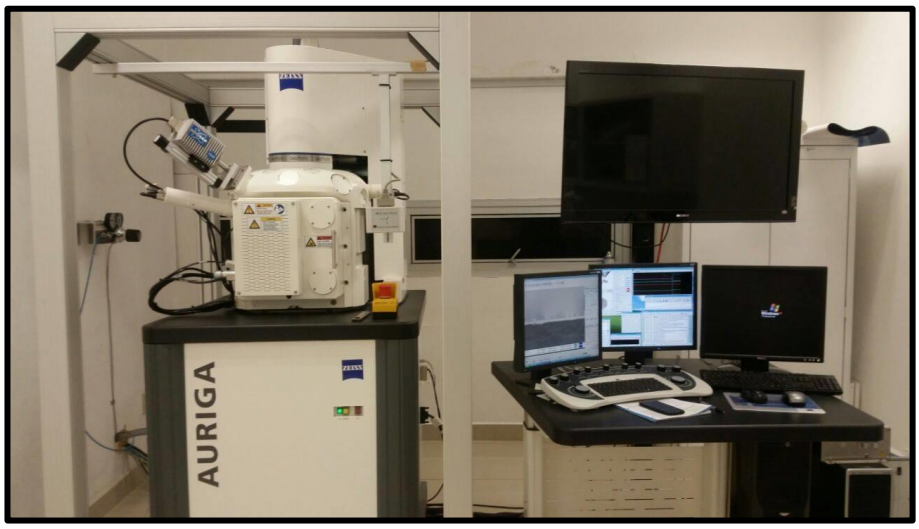

Fig.3.14. Carl Zeiss Auriga FESEM microscope.

3.6.4. Energy dispersive analysis of X -Rays

Energy dispersive X-Ray spectroscopy is a powerful chemical analysis technique. It normally uses in conjunction with FESEM. When beam of electron bombard with the sample, x-rays will be emitted from the sample whose energy is characteristic of the material from which it is emitted. EDAX X-ray detector measures the relative abundance of X-rays versus its energy. Detector is normally a Li-drifted Si, solid state device. The Detector creates charge pulse proportional to the energy of emitted X-rays which is then converts to voltage signal by a charge sensitive preamplifier. Later, it is sent to multichannel analyser where it is sorted by voltage. EDAX spectrum of X-ray energy versus counts is quantitatively evaluated to determine the elemental composition of the sample. In principle, EDAX can identify all elements from atomic number 4 to 92.

In this study, the composition of CIGSe powder and films are obtained using Bruker Ser 5010 X flash EDAX detector used with Carls Zeiss HRSEM Auriga microscope from LANE. The EDAX analysis of CIGSe powder and films are carried out at operating voltage of 20 kV.

3.6.5. Atomic Force Microscopy

Atomic force microscope (AFM) is a useful tool to analyse the surface topography of metals, semiconductors and insulating materials in real space on an atomic scale. A typical AFM system consists of a sharp probing tip, cantilever probe, piezoelectric (PZT) actuator and a photodetector. Cantilever and probe are mounted to PZT actuator. Photodetector receives laser beam reflected off the end -point of the beam and provides cantilever deflection feedback.

When the probing tip scans the surface of sample, it moves up and down in accordance with the sample surface and laser beam deflecting from the cantilever delivers the difference in light intensities between the upper and lower photodetectors. Feedback from the photodetector signal permits the tip to maintain either a constant force or constant height from the sample.

AFM normally operates in either of three modes (1) contact mode, (2) non-contact mode and (3) tapping mode. In the contact mode, cantilever tip remains in contact with sample surface and topographical properties of sample is obtained by monitoring the interaction forces between tip and sample surface. While in non-contact mode, cantilever is slightly away from the sample surface and oscillates at or near its resonant frequency. Natural resonant frequency of cantilever changes due to the attractive interaction with sample surfaces. PZT element attached to the cantilever monitors shift and topographical information about the sample is extracted. The tapping mode of operation combines the features of both contact and non-contact mode. In tapping mode, cantilever tip oscillates at or near its natural frequency while tip is allowed to contact the sample surface for a short time [3.24].

In this work, a JSPM 5200 environmental scanning probe microscope from LANE as shown in figure 3.15, in tapping mode is used to analyse the dispersion of particles in ink with change in Terpineol content.

Fig.3.15. JSPM 5200 Scanning Probe Microscope.

3.6.6. U-V visible/NIR spectroscopy analysis

UV-Vis/NIR spectroscopy analysis is a non- destructive and fast optical characterization technique. This technique investigates the material property through its interaction with light (100-2500 nm) by measuring the intensity of light transmitted, reflected or absorbed by the material using spectrophotometer. A UV-Vis/NIR spectrophotometer consists of couple of light sources, diffraction grating based monochromator, sample chamber and one or two detectors. Light from the source first passes through the diffraction grating where it gets separated into component wavelength. Now, the monochromatic beam passes through the slit to the sample and get reflected by the mirror and reaches the detector. Detector converts the light into current signal that is readable by a computer [3.25].

UV-Visible/NIR spectrum of a sample gives a plot of wavelength of incident light versus intensity of transmitted, reflected or absorbed light. UV-Vis/NIR transmittance spectrum is useful to obtain absorption coefficient, extinction coefficient, thickness, refractive index and bandgap of material.

From the transmittance spectrum of a film, absorbance coefficient is calculated using the following expression,

Absorption coefficient α = 1/t ln 1/T (Eq. : 3.3)

Where, t is the thickness of the film and T is the transmittance.

The type of bandgap of material is determined from the transition probability given by

$$\alpha h\vartheta^{p} = A\,(h\vartheta - E_g) \quad \text{(Eq. : 3.4)}$$

Where A is a constant and p is a variable

If, p=2, the transition between the bands are allowed direct band gap transitions.
If p =2/3, the transition is prohibited direct band gap.
If p=1/2, the transition is allowed indirect band gap.
If p=1/3, the transition is prohibited indirect band gap.

To find bandgap of a direct bandgap semiconductor material, a graph of hυ over $(\alpha h\upsilon)^2$ has to be plotted and then a straight line to this is fitted. The constant of this equation is Eg. But in the case of indirect bandgap material a graph of hυ over $(\alpha h\upsilon)^{1/2}$ has to be plotted and do the same to get Eg.

In the present work, UV-visible absorption spectra of CIGSe powder is analysed as a function of wavelength 400-1800 nm and UV-visible transmittance spectra of CdS film is analysed as a function of wavelength from 200-1100 nm using JASCO V-670 UV-Vis- NIR spectrophotometer from SEES as shown in figure 3.16. Spectral distributions of transmittance are determined at room temperature. Substrate absorption was corrected by introducing an uncoated clean glass in the reference beam.

Fig.3.16. JASCO V-670 UV-VIS-NIR Spectrophotometer.

3.6.7. Van der Pauw Method and Hall studies

Van der Pauw method is employed to measure the resistivity of samples. It is one of the most widely used technique to determine average resistivity of thin films. It can be used to measure samples of arbitrary shape if thickness of sample is uniform, point contacts are placed on the edges of the sample and sample is homogenous [3.26,3.27]. A schematic of sample with contacts 1, 2, 3 and 4 in Van der Pauw configuration is shown in figure 3.17. Van der Pauw showed a relation to find sheet resistance of the sample using two characteristic resistances R_A and R_B.

$$e^{\left(\frac{-\pi R_A}{R_S}\right)} + e^{\left(\frac{-\pi R_B}{R_S}\right)} = 1 \qquad \text{(Eq. :3.5)}$$

Where, Rs denotes the sheet resistance.

To determine R_A, a current I is forced through the sample between two neighbouring contacts, 1 and 2 as in figure 3.17 and the voltage is measured between the other two contacts 3 and 4. Then the measurement is repeated for other pairs of contacts to find R_B.

$$R_A = \frac{V_{43}}{I_{12}} \text{ and } R_A = \frac{V_{14}}{I_{23}} \qquad \text{(Eq. : 3.6)}$$

Resistivity (ρ) is obtained from the sheet resistance and thickness (t) of the sample using the relation,

$$\rho = R_s t \qquad \text{(Eq. : 3.7)}$$

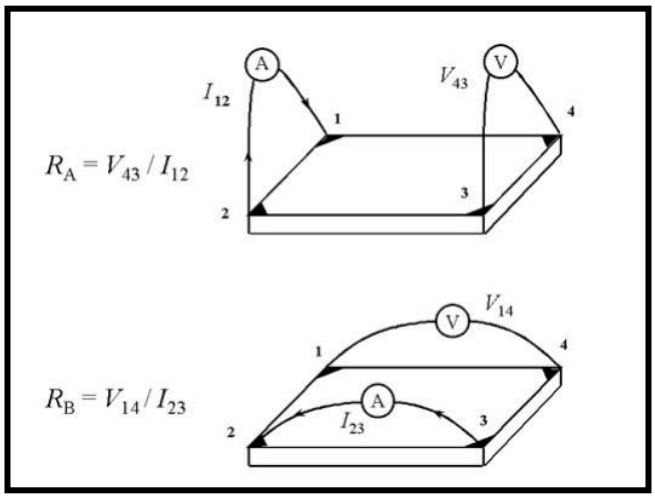

Fig.3.17. Schematic diagram of a Van der Pauw configuration used in the determination of the two characteristic resistances R_A and R_B [3.28].

Hall effect is used to find out the carrier concentration, carrier mobility and type of conductivity of a semiconductor material.

According to Hall effect, if the current density j_x passes through two non-neighbouring contacts 1 and 3 in presence of magnetic induction B_z, and an electric field E_y, the Hall coefficient R_H is defined by the equation

$$R_H = \frac{E_y}{j_x B_z} j_x B_z \qquad \text{(Eq. : 3.8)}$$

The sign of R_H depends on the type of conductivity of material. If R_H is negative, it indicates that Ey is along -y direction and electric current carriers are electrons. If R_H is positive, it indicates that Ey is along +y direction and electric current carriers are holes.

According to Drude model, R_H can be expressed as

$$R_H = \frac{1}{ne} \qquad \text{(Eq. : 3.9)}$$

Where, e is the electric charge and n is the concentration of charge carriers.

Mobility of charge carriers can determine if n and resistivity values are known [3.27].

$$\mu = \frac{1}{en\rho} \qquad \text{(Eq. : 3.10)}$$

Hall measurement system Lakeshore 8407 from SEES with an applied magnetic field of 15 KG at room temperature has been used to analyse conductivity type, carrier concentration, mobility of carrier and resistivity of selenized films (figure 3.18). To measure Hall effect, 100 nm thick circular gold contacts are deposited on the CIGSe film by evaporation method.

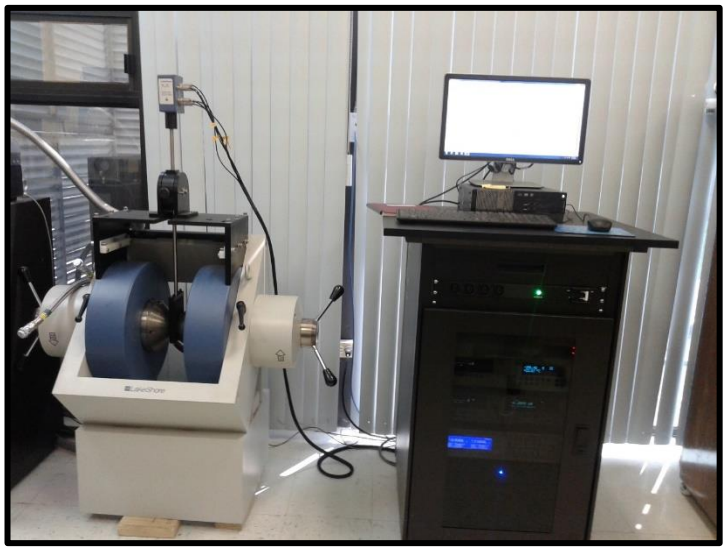

Fig.3.18. Lakeshore 8407 Hall measurement system.

3.6.8. Current-voltage (I-V) characteristics

I-V characteristics of CIGSe films under dark and illumination are obtained using Keithley 4200-SCS semiconductor characterization system (figure 3.19) from SEES by applying voltage from -10 to 10V. To perform I-V measurement, 100 nm thick Au contacts are made on the film by evaporation technique. The sample is placed on the sample holder and contacts were made to connect to two probes. Photocurrent is measured by illuminating the films using a light source of 300 W.

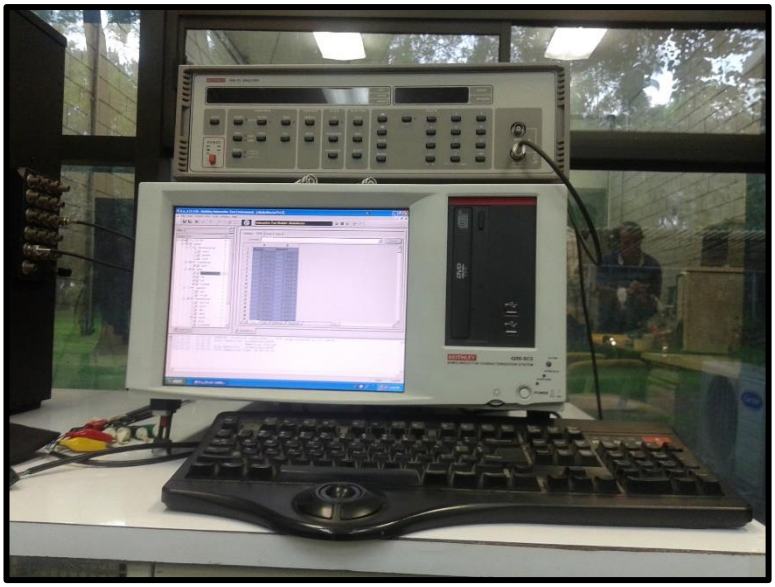

Fig.3.19. Keithley 4200-SCS semiconductor characterization system.

3.7. Characterization of Solar cell [3.30-3.33]

Electrically, an ideal solar cell is modelled by a current source in parallel with a diode. The relation between current and voltage in an ideal solar cell must be studied under dark and under illumination to evaluate its functionality.

3.7.1. Ideal solar cell conditions under dark

The dark I-V characteristic of an ideal solar cell is expressed in terms of diode law.

$$I = I_0 \left[\exp\left(\frac{qV}{mkT}\right) - 1\right] \qquad \text{(Eq. : 3.11)}$$

Where, I is the current flowing through the junction when a voltage V is applied. I_0 is the saturation current density. K is the Boltzman constant, T is the temperature of the diode, q is the charge of electron and m is the diode ideality factor. In terms of current density (current /unit area), J, J-V diode equation can be expressed as

$$J = J_0 \left[\exp\left(\frac{qV}{mkT}\right) - 1\right] \qquad \text{(Eq. : 3.12)}$$

The ideality factor m can be obtained from the equation given below.

$$\frac{1}{m} = \frac{kT}{q}\frac{d\ \ln J_{dark}}{dV} \qquad \text{(Eq. : 3.13)}$$

For an ideal diode, m=1 since it is assumed that all the recombination is taking place via band to band in the device and no recombination of charge carriers occurs at the junction. But, in the case of a non-ideal solar cell, m can have different values [3.30].

3.7.1.1. Conditions under dark for a heterojunction solar cell

In this work, the fabricated structure is a heterojunction system. Considering diffusion current and depletion layer recombination-generation component of reverse saturation current density, the equation 3.12 becomes,

$$J = J_0\ \left[exp\left(\frac{qV}{kT}\right) - 1\right] + J_1\ \left[exp\left(\frac{qV}{2kT}\right) - 1\right] \qquad \text{(Eq. : 3.14)}$$

Where J_0 is the diffusion component and J_1 is the depletion layer recombination - generation component of the reverse saturation current density. The diode ideality factor m =2 for the depletion layer recombination-generation component of reverse saturation current density. The J_0 and J_1 are defined by

$$J_0 = q\left(\frac{N_D D_n exp\left[-q\frac{(V_D-\Delta E_e)}{kT}\right]}{L_n \tan h\left(\frac{d}{L_n}\right)} + (\frac{N_A D_p \exp\left[\frac{-q(V_D+\triangle E_v)}{kT}\right]}{L_p \cot h\left(\frac{t_1}{L_p}+\phi\right)}\right) \qquad \text{(Eq.: 3.15)}$$

$$J_1 = q(\frac{n_1 l_1}{2K_1\tau_1} + \frac{n_2 l_2}{2K_2\tau_2})\frac{1}{\frac{q\,[V_D(V_D-V)]^{\frac{1}{2}}}{kT}} \qquad \text{(Eq.: 3.16)}$$

Here,

N_D is the concentration of donors in the n-type semiconductor

N_A is the concentration of acceptors in the p-type semiconductor

V_D is the built-in potential of the diode

ΔE_c is the discontinuity in the conduction band in volts

ΔE_p is the discontinuity in the valance band in volts

L_n is the diffusion length of electron in the p-type semiconductor

L_p is the diffusion length of hole in the n-type semiconductor

t_1 is the thickness of the n-type semiconductor (surface layer)

d is the thickness of the p-type semiconductor

τ_1 and τ_2 are the life time of minority carriers in the depletion region on both sides of the junction

n_1 and n_2 are the concentration of intrinsic carriers in the p- and n- type semiconductors

l_1 and l_2 are the width of the depletion layer in both the p- and n-type semiconductors at zero bias

$K_1 = \left(1 + \frac{N_1\varepsilon_1}{N_2\varepsilon_2}\right)^{-1}$ and $K_2 = 1 - K_1$, where, N_1 and N_2 are the concentration of impurities, and ε_1 and ε_2 are the dielectric constants of the p- and n-type semiconductors

$\phi = \frac{SL_p}{D_p}$, where, S is the surface recombination velocity in the n-type semiconductor and D_p is the diffusion constant of hole.

It is important to note that, according to equation 3.16, the current due to recombination at the depletion region (J_1) is depending on the applied voltage, V. Because, width of the depletion region and strength of electric field in this region is depend on the applied voltage [3.31].

In addition to the diffusion current and depletion layer recombination-generation current, the mechanism of charge carrier transport in a heterojunction system includes emission, emission -recombination, tunnelling and tunnelling-recombination models. The expressions for as-mentioned mechanisms are given below.

1. Emission mechanism

According to emission model, the analytical expression of the I-V characteristics for a p-n heterjunction (neglecting the generation-recombination within the space charge region) is given by

$$I = \frac{I_s\left[\exp\left(\frac{qV}{KT}\right)-1\right]}{\left(1+\frac{I_s}{I_d}\right)} \qquad \text{(Eq. : 3.17)}$$

Where, I_s is the electron saturation current and I_d is the emission limited current.

$$I_d = \frac{1}{2} aqX_m N_{D2} \nu_{xe2} \exp\left[-\frac{q}{kT}(V_F + V)\right] \quad \text{(Eq. : 3.18)}$$

Where, a is the junction area, N_{D1} and N_{D2} are the equilibrium donor concentration in p- and n-type semiconductor. ν_{xe2} is the x component of average speed of the electron in n-type material, $\nu_{xe2} = \left(\frac{2kT}{\pi m_n^*}\right)^{\frac{1}{2}}$, with m_n^* is the effective mass of electron in the n-type material. V_F is the forward barrier, D_{n1} and τ_{n1} are the diffusion constant and life time of electrons in the p-type material and X_m is the transmission coefficient.

2. Emission-recombination mechanism

The I-V characteristic of p-n heterojunction exhibiting emission-recombination mechanism can expressed as

$$I = I_s\left[exp\left(\frac{qV}{\beta kT}\right) - 1\right] \quad \text{(Eq. : 3.19)}$$

with $I_s = Bexp\left(-\frac{qV_D}{\beta kT}\right)$

where B is weakly temperature-dependent. Value of β depends on the ratio of densities of imperfections in the p- and n-type semiconductors. V_D is the total built-in voltage due to the difference in work function of p- and n-type semiconductors.

3. Tunneling mechanism

Using WKB approximation, probability for tunnelling of an electron at the bottom of the band under forward bias, T, is given by

$$T = \exp\left[-2\int_{x_1}^{x_2} \frac{[2m_n^*\{E_b(x) - q\propto V\}]^{\frac{1}{2}}}{\hbar}\, dx\right] \quad \text{(Eq. : 3.20)}$$

Where, $E_b(x)$ is the barrier height at any point x above the bottom of the conduction band, αV is the fraction of the applied voltage V.

The product of tunnelling probability and the incident electron flux gives tunnelling current. The I-V characteristics under forward bias for a heterostructure in which

tunnelling through the barrier exceeds thermal emission over the barrier can be expressed as

$$I = I_s(T) \exp\left(\frac{V}{V_0}\right) \qquad \text{(Eq. : 3.21)}$$

Where V_0 is a constant and I_s(T) is a weakly increasing function of temperature.

4. Tunnelling -recombination mechanism

Band-to-band tunnelling coupled with recombination process is one possible mechanism to occur in p-n heterojunction. In this, either electrons tunnel from the n-type material to empty interband in the p-type material and then recombine with holes, or holes tunnel from p-type material to the occupied states in the n-type material and recombine with the electrons. Forward current due to the tunnelling from the bottom of the conduction or top of the valance band can expressed as

$$I = B \exp[-\alpha(V_D - V)] \qquad \text{(Eq. : 3.22)}$$

Where, B is a weak function of voltage and temperature and V_D is the diffusion voltage. $\alpha = \frac{4}{3\hbar}\left(\frac{m_n^* \epsilon_2}{N_{D2}}\right)^{\frac{1}{2}}$, where ε_2 is the dielectric constant of the n-type semiconductor.

To include these mechanisms, current density due to the above mentioned mechanisms must be added to equation 3.14, assuming that the distinct mechanisms are independent.

3.7.2. Solar cell under illumination

The I-V characteristic of solar cell under illumination is given by

$$I = I_0\left(e^{\frac{qV}{mkT}} - 1\right) - I_L \quad \text{or}$$

$$J = J_0\left(e^{\frac{qV}{mkT}} - 1\right) - J_L \qquad \text{(Eq. : 3.23)}$$

Where, I_L is the light generated current. I_L has the value

$$I_L = qAG\ (L_e + W + L_h)$$
$$J_L = qG\ (L_e + W + L_h) \qquad \text{(Eq. : 3.24)}$$

Where, G is the net current generation rate due to illumination, L_e and L_h are the diffusion length of electrons and holes and W is the width of depletion region. This expression implies that light generated current density, J_L, constitutes the total photo generated current due to the carriers in the depletion region of the diode and within the minority carrier diffusion length on both P and N side of the diode. Hence, the depletion region and the region lying within the diffusion length of P and N side of the diode is called as “active” collection region of a solar cell.

The J-V characteristic of p-n diode in dark and under illumination is shown in figure 3.20. The illuminated I-V characteristics of p-n diode are the dark characteristics shifted down by the current J_L. This downward shift of the I-V characteristics gives a region in the fourth quadrant of the plot signifying that power can be extracted from the diode.

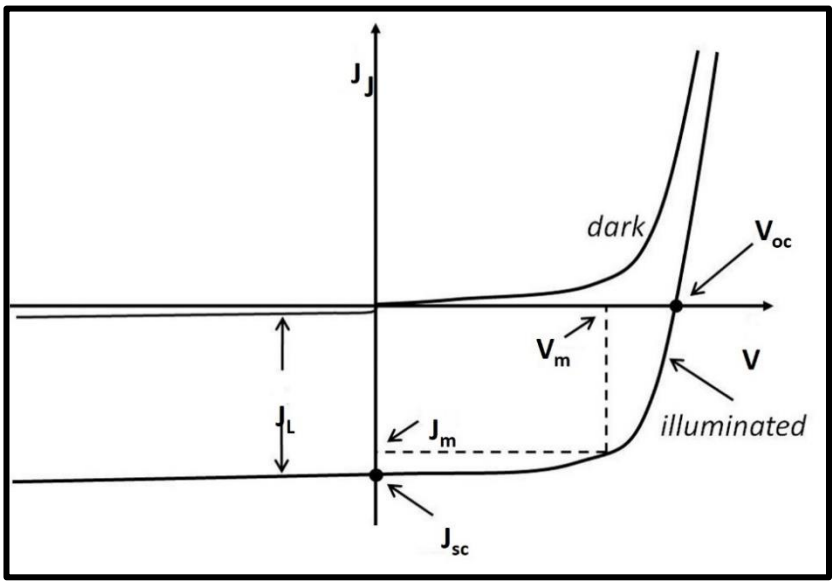

Fig.3.20. I-V characteristics of p-n diode under dark and illumination [3.30].

3.7.3. Performance characteristics of a solar cell

Short circuit current density (J_{sc}): Short circuit current density is the current density through the solar cell when the voltage across the solar cell is zero. For an ideal solar cell J_{sc} is equal to J_L.

Open circuit voltage (V_{oc}): Open circuit voltage is the maximum voltage available from the solar cell when no current flows through it.

$$V_{oc} = \frac{kT}{q} \ln\left(\frac{J_{sc}}{J_0} + 1\right) \quad \text{(Eq. : 3.25)}$$

Fill factor (FF): Fill factor is defined as the ratio between the product of current density (J_m) and voltage(V_m) values corresponding to maximum power point of solar cell to the product of J_{sc} and V_{oc}.

$$FF = \frac{J_m V_m}{J_{sc} V_{oc}} \quad \text{(Eq. : 3.26)}$$

Efficiency (η): Efficiency of a solar cell is defined as the ratio of power delivered at operating point to the power of incident light (P_s).

$$\eta = \frac{J_m V_m}{P_s} \quad \text{(Eq. : 3.27)}$$

Effect of parasitic resistances:

In the practical solar cells, power is dissipated through the contact resistance and through leakage current. These effects are equivalent to two resistances, one in series (series resistance, R_s) and other in parallel (shunt resistance, R_{sh}) with the solar cell. The series resistance (R_s) can arise from (i) the bulk resistance of the semiconductor material in the solar cell, (ii) the bulk resistance of metallic contact with the interconnections and (iii) the contact resistance between the metallic contact and the semiconductor. The shunt resistance (R_{sh}) is mainly because of the leakage current at the junction due to crystal defects and presence of foreign impurities. Both R_s and R_{sh}

are known as parasitic resistances [3.30,3.33]. The equivalent circuit of a solar cell is shown in figure 3.21.

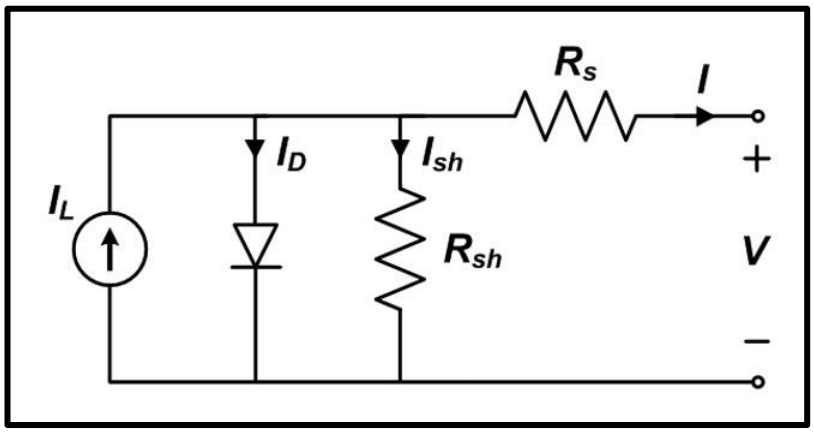

Fig.3.21. The equivalent circuit of a solar cell [3.33].

Considering parasitic resistances, the diode equation under illumination changes to

$$J = J_{sc} - J_0\left(e^{q(\frac{V+JAR_S}{kT})} - 1\right) - \frac{V+JAR_S}{R_{sh}} \qquad \text{(Eq. : 3.28)}$$

Figure 3.22 shows the variation in I-V curve of solar cell with changes in R_s and R_{sh}.

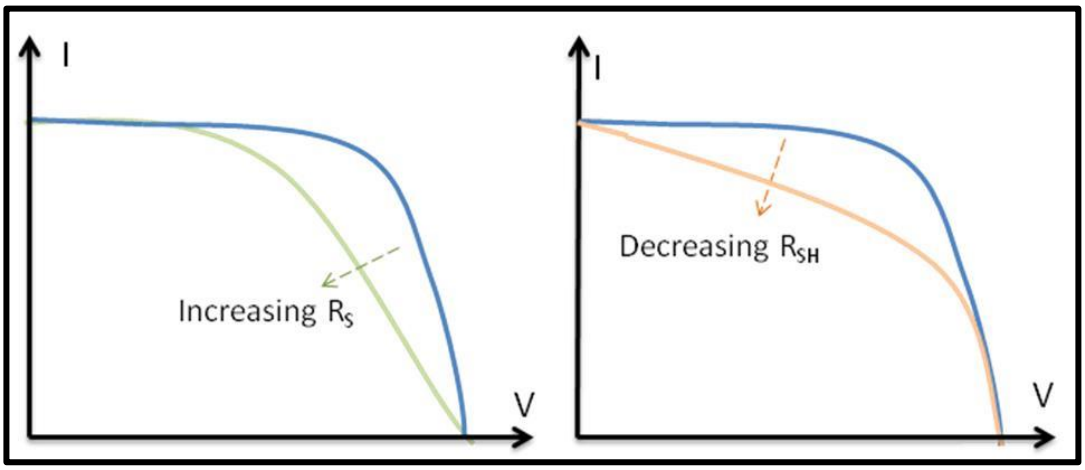

Fig.3.22. Illustration of variation in I-V curve of solar cell with change in (a) series resistance and (b) shunt resistance [3.34].

In this study, I–V characteristics of fabricated heterostructures were recorded at room temperature using Newport 91160 solar simulator from ESFM-IPN s shown in figure

3.23. This simulator has output equivalent to 1.96 sun (AM 1 global irradiation) and a filter is used to obtain intensity of light equivalent to one sun (100 mW/cm^2- AM 1.5 global irradiation).

Fig.3.23. Newport 91160 solar simulator.

References

3.1. J.S. Benjamin, “Dispersion strengthened super alloys by mechanical alloying”, Metallurgical Transactions 1 (1970) 2943-2951.

3.2. C.Suryanarayana, “Mechanical alloying and milling”, Progress in Material Science 46 (2001) 1-184.

3.3. C.C. Koch, O.B. Cavin, C.G. McKamey, J.O. Scarbrough, “Preparation of amorphous $Ni_{60}Nb_{40}$ by mechanical alloying” Applied Physics Letters 43 (1983) 1017-1019.

3.4. J.S. Benjamin, “Mechanical Alloying”, Scientific American 234 (1976) 40-49.

3.5. P.Y. Lee, J.L. Yang, H.M. Lin, “Amorphization behavior in mechanically alloyed Ni-Ta powders”, Journal of Materials Science 33 (1998) 235-239.

3.6. I. Repins, M.A. Contreras, B. Egaas, “19.9 % efficienct ZnO/CdS/CIGSe solar cells with 81.2% fill factor. Progress in photovoltaics: Reseach and applications 16 (2008) 235-239.

3.7. K. Wasa, I. Kanno, H. Kotera, “Handbook of sputter deposition technology: Principles, Technology and Application, (1991).

3.8. K. Seshan, “Ion Beam Deposition”, in Handbook of Thin Film Deposition Processes and Techniques, William Andrew, NY (2002).

3.9. H. Azimi, Y. Hou, C.J. Brade, “Towards low-cost, environmentally friendly printed chalcopyrite and kesterite solar cells”, Energy Environmental Science 7(2014)1829-1849.

3.10. A.O. Pudov, “Impact of secondary barriers on $CuIn_{1-x}Ga_xSe_2$ solar cell operation”, Dissertation (2005), Colorado State University, U.S.A.

3.11. J.B. Babu, “Deposition and characterization of TCO’s (AZO and ITO),i-ZnO and graded CIGS structure thin films for photovoltaic application using spray pyrolysis”, Dissertation (2012),CINVESTAV, Mexico.

3.12. J.H. Scofield, A. Duda, D. Albin, B.L. Ballard, P.K. Predecki, “Sputtered Molybdenum bilayer back contact for copper indium diselenide-based polycrystalline thin film solar cells”, Thin Solid Films 260 (1995) 26-31.

3.13. P. Jackson, D. Hariskos, E. Lotter, S. Paetel, R. Wuerz, R. Menner, W. Wischmann, M. Powalla, “New world record efficiency for $Cu(In,Ga)Se_2$ thin film

solar cells beyond 20%", Progress in Photovoltaics :Research and Applications 19 (2011) 894-897.

3.14. I. Repins, S. Glynn, J. Duenow, T.J. Coutts, W. Metzger and M.A. Contreras, " Required Materials properties for high-efficiency CIGS modules", Conference paper, NREL/CP-520-46235 (2009).

3.15. M.A. Contreras, M.J. Romero, B. To, F. Hasoon, R. Noufi, S. Ward, K. Ramanathan, "Optimization of CBD CdS process in high-efficiency Cu(In,Ga)Se_2-based solar cells", Thin Solid Films 403-404 (2002) 204-211.

3.16. A. Carrillo-Castillo, R.C. Ambrosio Lazaro, E.M. Lira Ojeda, C.A. Martinez Perez, M.A. Quevedo-Lopez, F.S. Aguirre-Tostado, "Characterization of CdS thin films deposited by chemical bath deposition using novel complexing agents", Chalcogenide Letters 10 (2013) 421-425.

3.17. J.S. Cruz, R.C. Perez, G.T. Delgado, O.Z. Angel, "CdS thin films doped with metal-organic salts using chemical bath deposition", Thin Solid Films 518 (2010) 1791-1795.

3.18. F.A. Pulgarin Agudelo, "Desarrollo de celdas solares de calcopirita mediante nuevas rutas basadas en tecnicas de impression de nanoparticulas", Dissertation (2013), Institute of Renewable Energy-UNAM, Mexico.

3.19. B.D. Cullity, "Elements of X-ray diffraction" Addison-Wesley (1956).

3.20. G.S. Bumbrah, R.M. Sharma, "Raman spectroscopy- basic principle, instrumentation and selected applications for the characterization of drug of abuse ", Egyptian Journal of Forensic Sciences, in press, corrected proof (2015).

3.21. J. Lazewski, H. Neumann, K. Parlinski, G. Lippold, B. J. Stanbery, "Lattice dynamics of CuAu-ordered $CuInSe_2$", Physical Review B 68 (2003) 144108-1-144108-5.

3.22. D. Papadimitriou, N. Esser, C. Xue, "Structural properties of chalcopyrite thin films studied by Raman spectroscopy", Physica Status Solidi (b) 242 (2005) 2633-2643.

3.23. H. Yao, K. Kimura, "Field emission scanning microscopy for structural characterization of 3D gold nanoparticle super lattices", Modern Research and Educational Topics in Microscopy (2007) 568-575.

3.24. N. Jalili, K. Laxminarayana, "A review of atomic force microscopy imaging systems: application to molecular metrology and biological sciences", Mechatronics 14 (2004) 907-945.

3.25. A. Oudhia, “UV-VIS spectroscopy as a nondestructive and effective characterization tool for II-VI compounds”, Recent Research in Science and Technology 4 (2012) 109-111.

3.26. L. J. Van der Pauw, “A Method of Measuring the Resistivity and Hall Coefficient on Lamellae of Arbitrary Shape”, Philips Technical Review 20 (1958) 220-224.

3.27. A.A. Ramdan, R.D. Gould, A. Ashour, “On the Van der Pauw method of resistivity measurements”, Thin Solid Films 239 (1994) 272-275.

3.28. The Hall Effect, https://www.nist.gov/pml/engineering-physics-division/hall-effect

3.29. C. Kittel, “Introduction to Solid State Physics”, John Willey & Sons, Inc. USA, 7th edition: (1995) 164.

3.30. M. A. Green, “Solar cells operating principles, technology, and system applications”, Prentice Hall, Inc.: (1982).

3.31. A.G. Milnes, D.L. Feucht, “Heterojunctions and metal-semiconductor junctions”, Academic Press, Inc.: (1972)

3.32. B.L. Sharma, R.K. Purohit, “Semiconductor heterojunctions”, Pergamon Press, (1974).

3.33. J. Nelson, “The Physics of solar cells”, Imperial college press: (2003).

3.34. Part II-Photovoltaic cell I-V characterization theory and lab view analysis code, http://www.ni.com/white-paper/7230/en/

CHAPTER - 4

DEPOSITION OF $Cu(In,Ga)Se_2$ FILM USING MECHANOCHEMICALLY SYNTHESIZED $Cu(In,Ga)Se_2$ POWDER

In this chapter, we discuss the mechanochemical synthesis of $Cu(In,Ga)Se_2$ (CIGSe) powder, where we study the effect of milling parameters such as milling time, ball to powder ratio and milling speed. CIGSe powder prepared by optimised condition is used for film deposition. Then the structural, compositional and morphological studies of deposited films have been carried out. Electrical properties of selected sample are also studied.

4.1. Mechanochemical synthesis of $Cu(In_{0.5},Ga_{0.5})Se_2$ powder

$Cu(In_{0.5},Ga_{0.5})Se_2$ powder has been synthesized mechanochemically by optimising the most important milling parameters such as milling time, BPR and milling speed. The prime objective of the optimization process is to synthesize single-phase $Cu(In_{0.5},Ga_{0.5})Se_2$ powder with the shortest possible time to reduce the synthesis time and thus the energy of the process. It was achieved by varying milling parameters as given in Chapter 3, table 3.1.

4.1.1. Effect of milling time

Milling time is the first milling parameter to be investigated and for that milling time is varied from 0.5 h to 6 h keeping BPR as 15:1 and milling speed at 400 rpm. Figure 4.1 shows XRD patterns of $Cu(In_{0.5},Ga_{0.5})Se_2$ powder milled from 30 min to 6 h and many diffraction peaks corresponding to various compounds can be identified. In the case of 30 min milled powder, according to the Joint Committee of Powder Diffraction Standard (JCPDS), binary compounds such as In_6Se_7 (JCPDS # 00-025-0385), β CuSe (JCPDS # 27-0184), Ga_2Se_3 (JCPDS # 33-0568), β In_2Se_3 (JCPDS # 20-0494), α Cu_2Se (JCPDS # 27-1131) and InSe (JCPDS # 42-0919) are detected at 2θ values 23.46º, 29.68º, 32.96º, 36.28º, 39.18º, 43.34º, 50.42º and 54.48º respectively. Also, 3 peaks related to (112), (220)/(204) and (312)/(116) chalcopyrite phase of

$Cu(In_{0.5},Ga_{0.5})Se_2$ (JCPDS # 40-1488) is detected at 2θ values of 27.14º, 45.18º and 53.4º respectively. The diffraction peak of In_6Se_7 and β In_2Se_3 diminishes significantly after 1 h of milling. Simultaneously, the peak intensity of three chalcopyrite $CuIn_{0.5}Ga_{0.5}Se_2$ phase increases. The peak corresponding to β CuSe vanishes completely after 2 h of milling. The 4 h milled powder shows very small intense peaks of Ga_2Se_3, α Cu_2Se and InSe with dominant peaks of $Cu(In_{0.5},Ga_{0.5})Se_2$. The powder milled for 6 h presents peaks related to single chalcopyrite phase $Cu(In_{0.5},Ga_{0.5})Se_2$. Additionally, a shift in peak position to lower 2θ value can be noticed with increasing milling time. Vidhya et.al [4.1] attributed this shift to the internal stress induced by milling. This induced stress alters the lattice parameter and thus results in a shift in XRD peak position.

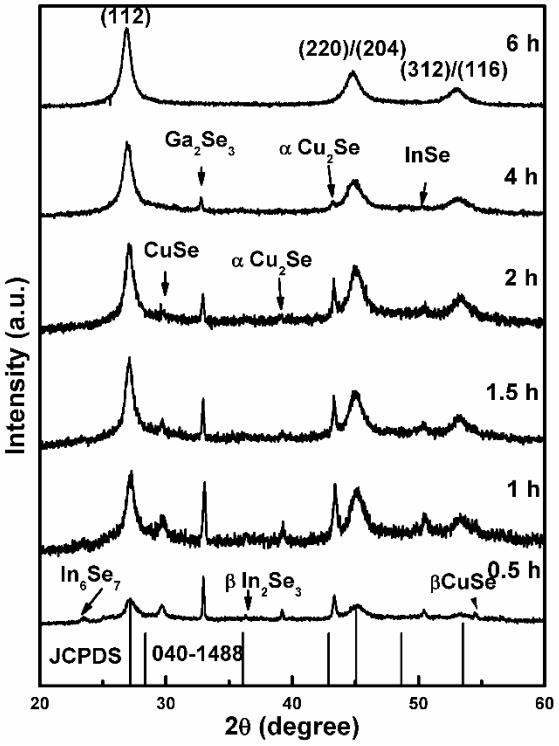

Fig.4.1. X-ray diffraction patterns of the $Cu(In_{0.5},Ga_{0.5})Se_2$ powder prepared at different milling time: (a) 30 min; (b) 1 h; (c) 1 h 30 min; (d) 2 h; (e) 4 h and (f) 6 h.

The possible formation mechanism of $Cu(In_{0.5},Ga_{0.5})Se_2$ powder during mechanical milling can be explained based on previous literature study [4.2] and the secondary phases present in the powder prior to the formation of single phase $Cu(In_{0.5},Ga_{0.5})Se_2$. The melting point of elemental Cu, In, Ga and Se used in this study are 1083, 160,

29.8 and 220º C respectively. The three elements In, Ga and Se have low melting point whereas the element Cu has high melting point. Whereas, Zhang et.al [4.3] has reported that the maximum temperature attained during mechanical impacts is less than 350º C. The nature of heat generation during ball to ball collision is explained by Kwon et.al [4.4]. According to Kwon et.al, the impact of ball to ball collision lasts for a very short time. Therefore, the powder trapped between the balls during ball to ball collision heat up very fast for a short time and cools down after the impact. In the case of milling Cu, In, Ga and Se; the low melting point elements In, Ga and Se melts locally in the powder as the kinetic energy of balls convert to heat after the collision. Subsequently the chemical reaction between elemental Cu with In, Ga and Se will take place. Contrary to the long hours of milling necessary for the formation of alloy in particular cases [4.5], here $Cu(In_{0.5},Ga_{0.5})Se_2$ powder phase forms along with the metastable phases in 30 minutes of milling. Since in this case, elemental powders go through solid chemical reaction leading to the formation of metastable binary phases. Then, $CuIn_{0.5}Ga_{0.5}Se_2$ alloy formation take place due to the shortened solid state diffusion distance and increased density of defects together with heating process occurred during milling process [4.5-4.7]. The metastable phase formed during ball milling depends on their standard Gibbs free energy. The Gibbs free energy of In_2Se_3, Ga_2Se_3, CuSe and Cu_2Se are -318 [4.8], -376 [4.9], -39.5 [4.10] and -65 kJ/mol respectively [4.11]. The formation energy for CISe and CGSe are -262 and -313 kJ/mol respectively [4.11]. From this data, it can be deduced that In_2Se_3 and Ga_2Se_3 phases form easily than Cu_2Se and CuSe phases. The possible reactions leading to the formation of $Cu(In_{0.5},Ga_{0.5})Se_2$ powder during milling process are listed below.

$$6\,In + 7\,Se \rightarrow In_6Se_7 \qquad \text{(Eq. : 4.1)}$$

$$Cu + Se \rightarrow CuSe \qquad \text{(Eq. : 4.2)}$$

$$2\,Ga + 3\,Se \rightarrow Ga_2Se_3 \qquad \text{(Eq. : 4.3)}$$

$$2\,In + 3\,Se \rightarrow In_2Se_3 \qquad \text{(Eq. : 4.4)}$$

$$2\,Cu + Se \rightarrow Cu_2Se \qquad \text{(Eq. : 4.5)}$$

$$In + Se \rightarrow InSe \qquad \text{(Eq. : 4.6)}$$

$$Cu + Se \rightarrow CuSe \quad \text{(Eq. : 4.7)}$$

$$InSe + CuSe \rightarrow CuInSe \quad \text{(Eq. : 4.8)}$$

$$Cu_2Se + In_2Se_3 \rightarrow 2CuInSe_2 \quad \text{(Eq. : 4.9)}$$

$$Cu_2Se + Ga_2Se_3 \rightarrow 2CuGaSe_2 \quad \text{(Eq. : 4.10)}$$

$$CuInSe_2 + CuGaSe_2 \rightarrow Cu(In, Ga)Se_2 \quad \text{(Eq. : 4.11)}$$

The crystallite size of milled $Cu(In_{0.5},Ga_{0.5})Se_2$ powders with respect to (112) peak are calculated using Scherrer-Debbey equation and plotted against milling time (figure 4.2). Here, it is important to mention that crystallite sizes are measured taking in to account only one XRD pattern of the respected sample. It is found that crystallite size increases from 17 to 19.58 nm with increase in milling time from 30 min to 1 h. The XRD peak in the 30 min milled powder is wider and smaller to the peak in 1 h milled powder. This can be due to amorphous nature of the milled powder. Except the sample milled for 30 min, the other milled powders show a tendency of decreasing crystallite size with increasing milling time. This behaviour has reported by Zuhailawati et.al [4.12]. It is explained based on the crystallite refinement through introduction of defects such as dislocations within a grain during mechanical alloying process [4.13]. This indicates that mechanochemical process is greatly effective in reducing crystallite size by increasing milling time.

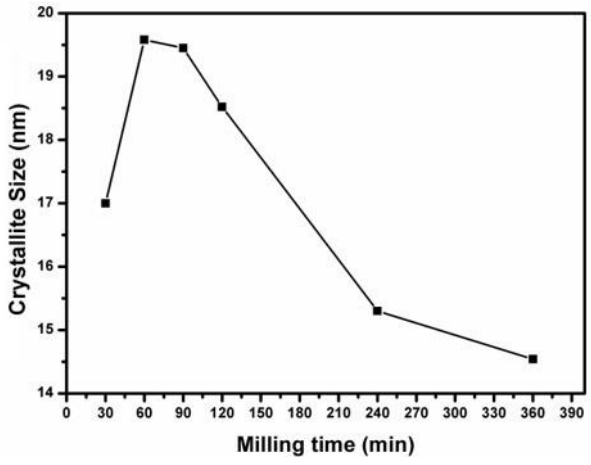

Fig.4.2. The crystallite size of $Cu(In_{0.5},Ga_{0.5})Se_2$ powder versus milling time.

The morphology observed by FESEM of $Cu(In_{0.5},Ga_{0.5})Se_2$ powder milled for 30 min, 1 h, 1 h 30 min, 2 h, 4 h and 6 h are shown in figure 4.3. It indicates that morphology of $CuIn_{0.5}Ga_{0.5}Se_2$ alloy changes with milling time. As mentioned in section 3.1.1, mechanical milling is a process of repeated flattening, cold welding, fracturing and rewelding of precursor powder particles [4.14]. In the case of mechanical milling of Cu, In, Ga and Se; Cu, In and Ga are ductile elements while Se is brittle. Hence it can be taken as milling of a ductile-brittle system.

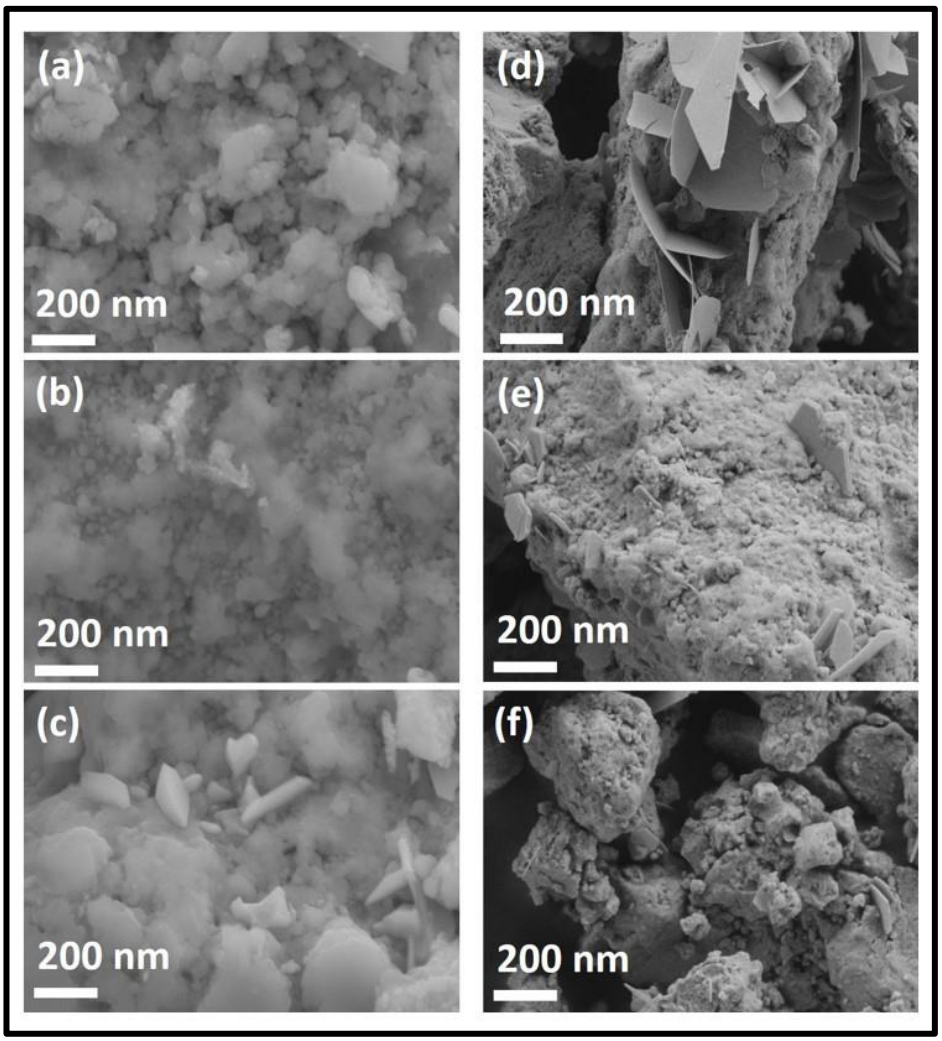

Fig.4.3. FESEM images of $Cu(In_{0.5},Ga_{0.5})Se_2$ powder milled for (a) 30 min; (b) 1 h; (c) 1 h 30 min; (d) 2 h; (e) 4 h and (f) 6 h.

Fogagnolo et.al [4.15] has presented a model to explain mechanical milling of a ductile-brittle system. According to that, ductile particles undergo deformation whilst brittle

particle undergoes fragmentation during the initial stage of milling. Subsequently, ductile particles start to weld, and brittle particle come between two or more ductile particles at the time of ball-ball collision. As a result, the brittle Se particles will be placed in the interfacial boundaries of welded Cu, In and Ga particles. One important fact to note in mechanical milling process is that, it is statistical in nature. Each particle experiences a unique processing history [4.16]. Different morphology of particles observed in the FESEM images can be related to statistical nature of the process. The 30 min and 1 h milled powder show similar FESEM images. The powder milled for 1 h 30 min shows rod-like structures. A thin flat-plate like structures are present in the powder milled for 2 h. Powder milled for 4 h exhibits broken pieces of flat plate-like structures which is taken into the bulk of the powder. Powder milled for 6 h observes as fractured pieces of powder milled for 4 h. Also, the synthesized $Cu(In_{0.5},Ga_{0.5})Se_2$ powder particles are heavily agglomerated. Agglomeration is an inherent property of mechanically milled particles. The tendency to agglomerate increases as fractured particles have gained high surface energy. High surface energy and cohesion among particles with decreasing particle size account for agglomeration. The fracturing and cold welding mechanisms continue as milling time prolongs [4.12].

Table 4.1: EDAX data of $Cu(In_{0.5},Ga_{0.5})Se_2$ powder milled for different milling time.

Sample	Atomic percentage of elements (at.%)				Cu/(In+Ga)	Ga/(In+Ga)
	Cu	In	Ga	Se		
30 min	22.12	14.31	14.77	48.80	0.76	0.51
1 h	20.86	7.19	14.72	57.24	0.95	0.67
1 h 30 min	21.08	8.49	10.32	60.12	1.12	0.55
2 h	24.01	10.08	13.42	52.49	1.02	0.57
4 h	25.73	12.40	12.86	49.02	1.02	0.51
6 h	25.97	12.31	12.78	48.95	1.03	0.51

The EDAX analysis of $Cu(In_{0.5},Ga_{0.5})Se_2$ powder milled for 30 min, 1 h, 1 h 30 min, 2 h, 4 h and 6 h is measured at operating voltage of 20 kV and is given in table 4.1. It shows uneven variation in the atomic percentage of elements (table 4.1). Since milling

time is short, the distribution of elements in the powder is not homogenous. But as the milling time progress, the elements alloys well homogenously. The powder milled for 4 and 6 h present similar EDAX composition data. The composition of the $Cu(In_{0.5},Ga_{0.5})Se_2$ powder milled for 4 and 6 h are $Cu_{1.03}(In_{0.49},Ga_{0.51})Se_{1.96}$ and $Cu_{1.04}(In_{0.49},Ga_{0.51})Se_{1.96}$ respectively. Hence it is clear that milling time has an influence on the homogeneity of milled powder.

4.1.2. Effect of Ball to Powder Ratio

Using BPR of 15:1 and milling speed of 400 rpm, single-phase $Cu(In_{0.5},Ga_{0.5})Se_2$ formation takes place after milling for 6 h. The next milling parameter to be investigated is BPR as a means to reduce milling time.

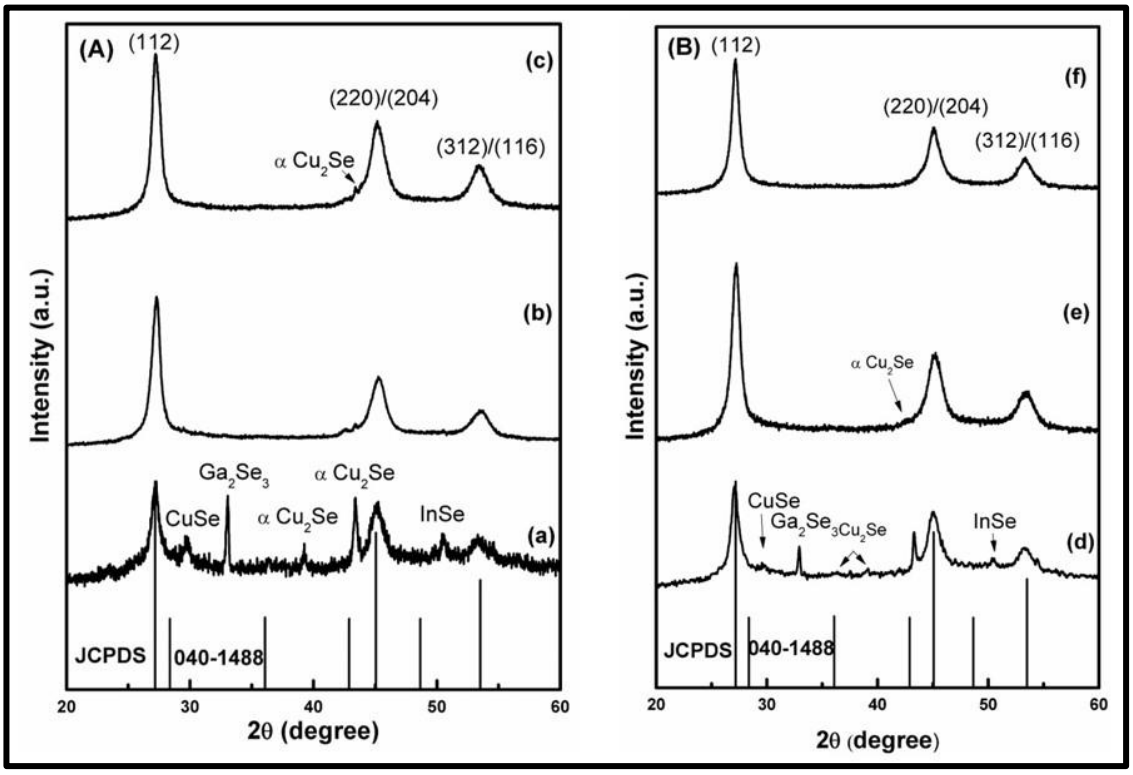

Fig.4.4. X-ray diffraction patterns of the $Cu(In_{0.5},Ga_{0.5})Se_2$ powder synthesized at (a) 15:1-1 h; (b) 20:1-1 h; (c) 25:1-1 h; (d) 15:1-2 h; (e) 20:1-2 h and (f) 25:1-2 h.

Figure 4.4 represents XRD pattern of $Cu(In_{0.5},Ga_{0.5})Se_2$ powder milled with BPR of 15:1, 20:1 and 25:1 for 1 h and 2 h with a milling speed of 400 rpm. In the case of powder milled for 2 h, it exhibits that as BPR increase from 15:1 to 20:1, the binary metastable phases except Cu_2Se disappear and subsequent increase of BPR to 25:1 results in the formation of single chalcopyrite phase of $Cu(In_{0.5},Ga_{0.5})Se_2$. In the case of powder milled for 1 h with BPR of 15:1, 20:1 and 25:1, the powder with BPR of 25:1 shows a very small intensity peak related to Cu_2Se. However, it is very clear that higher BPR helps to reduce the time required to form single-phase $Cu(In_{0.5},Ga_{0.5})Se_2$. BPR is the ratio of the total mass of balls to the total mass of reactants. In the case of balls of equal mass, higher BPR indicates higher number of balls. When the number of balls increased, the collision frequency increased i.e. there will be an increased number of contacts between the balls and the powder. Moreover, the total energy input to the powder increases with increase in the number of collision [4.17]. Hence $Cu(In_{0.5},Ga_{0.5})Se_2$ powder forms in shorter milling time. Also, it is evident that milling time is dependent on BPR. Suryanarayana et al [4.5] have reported similar dependency of BPR on milling time.

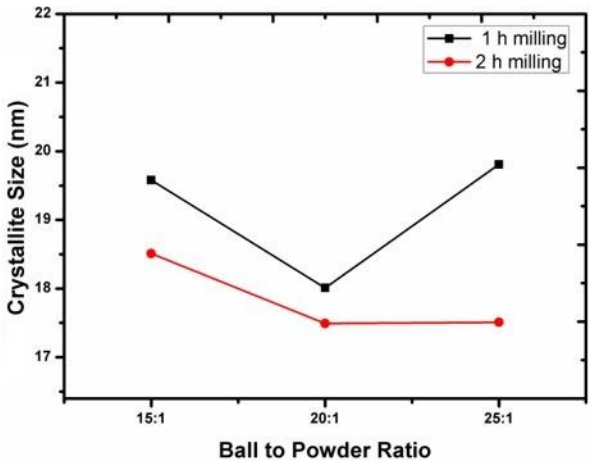

Fig.4.5. The crystallite size of $Cu(In_{0.5},Ga_{0.5})Se_2$ powder versus BPR.

Variation in the crystallite size of $Cu(In_{0.5},Ga_{0.5})Se_2$ powder milled for 1 h and 2 h with BPR calculated from XRD pattern given in figure 4.4 are shown in figure 4.5. In the case of powder milled for 1 h with BPR of 15:1, 20:1 and 25:1, the crystallite size is calculated as 19.58, 18.05 and 19.81 nm respectively. The 2 h milled powder with BPR

of 15:1,20:1 and 25:1showed crystallite size 18.51,17.49 and 17.51 nm respectively. i.e crystallite size changes randomly with the ball to powder ratio. At the same time, it is worth to note that powder milled for 2 h have lower crystallite size to powder milled for 1 h.

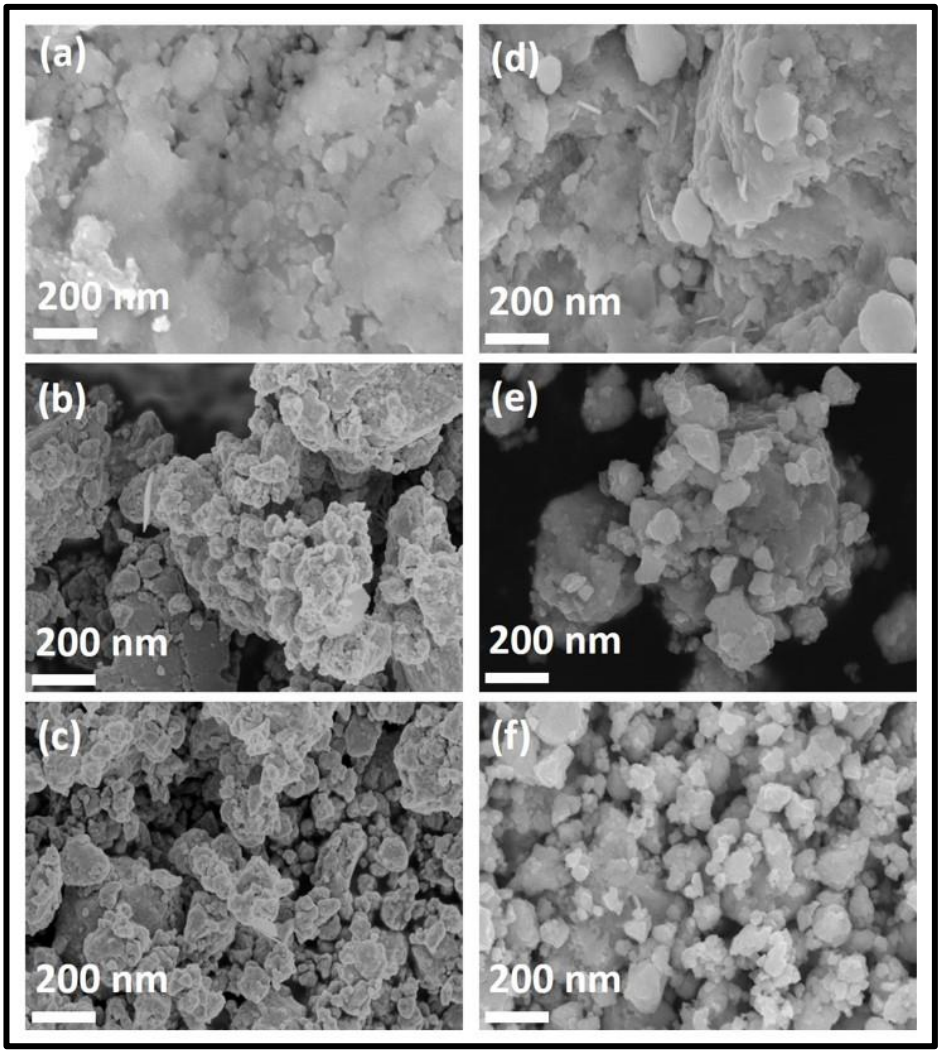

Fig.4.6. FESEM images of the $Cu(In_{0.5},Ga_{0.5})Se_2$ powder synthesized at different BPR for 1 and 2 h: (a) 15:1-1 h; (b) 20:1-1 h; (c) 25:1-1 h; (d) 15:1-2 h; (e) 20:1-2 h and (f) 25:1-2 h.

FESEM images of $CuIn_{0.5}Ga_{0.5}Se_2$ powder milled with BPR of 15:1, 20:1 and 25:1 for 1 and 2 h are shown in figure 4.6. It can be observed that $CuIn_{0.5}Ga_{0.5}Se_2$ powder milled at BPR of 15:1 for 1 and 2 h consists of highly cold welded structures. Individual agglomerated spherical structures over the cold-welded powder can be seen in the

powder milled at BPR of 15:1 for 2 h. while, powder milled with BPR of 20:1 shows cold welded structures which are smaller as compared to powder milled with BPR of 15:1. The subsequent increase of BPR to 25:1 resulted in structures which are smaller in size as compared to powder milled with lower BPR. The similar tendency of changes in morphology can be observed for powder milled at higher BPR with milling time of 2 h. The decrease in size of particles with an increase in BPR can be explained as fracturing process take over cold welding process. With increasing BPR, the frequency of collisions rises and mean free path between two collisions declines [4.17]. From the morphology of powders, it can be deduced that higher BPR favours fracturing process over welding process. The $Cu(In_{0.5},Ga_{0.5})Se_2$ powder synthesized with BPR of 25:1, milling speed of 400 rpm and milling time of 2 h showed less agglomerations compared to remaining milling conditions.

Table 4.2. EDAX composition analysis of $Cu(In_{0.5},Ga_{0.5})Se_2$ powder synthesized at different BPR for 1 and 2 h of milling time.

Sample	Atomic percentage of elements (%)				Cu/(In+Ga)	Ga/(In+Ga)
	Cu	In	Ga	Se		
15:1-1h	20.86	7.19	14.72	57.24	0.95	0.67
20:1-1h	26.73	10.85	13.90	48.51	1.07	0.56
25:1-1h	25.26	12.61	11.86	50.25	1.03	0.48
15:1-2h	24.01	10.08	13.42	52.49	1.02	0.57
20:1-2h	27.77	10.14	13.50	48.66	1.18	0.57
25:1-2h	27.55	11.40	12.65	48.40	1.14	0.52

EDAX composition analysis of $Cu(In_{0.5},Ga_{0.5})Se_2$ powder synthesized with BPR of 15:1, 20:1 and 25:1 for 1 and 2 h are measured at operating voltage of 20 kV and is given in table 4.2. Results show the influence of BPR on determining the composition of final product. The atomic percentage of Cu is found to rise from 20.86 to 26. 73 and 24.01 to 27.32 with increasing BPR from 15:1 to 20:1 for 1 and 2 h milled powder. While Se atomic percentage decreases from 57.24 to 50.25 and 52.49 to 48.89 for 1 and 2 h milled samples as a function of BPR. Whereas an increase in the atomic

percentage of In is observed with changing BPR from 20:1 to 25:1. The results indicate that higher BPR favours incorporation of Cu and In, while it would lead to loss of Se due to higher heat energy developed with high BPR. The sample milled with 25:1 showed Ga/(In+Ga) closely matching to the initial precursor stoichiometry $Cu(In_{0.5},Ga_{0.5})Se_2$. As single-phase and less agglomerated $Cu(In_{0.5},Ga_{0.5})Se_2$ particles were obtained with BPR of 25:1, we fixed 25:1 as optimum BPR for further experiments.

4.1.3. Effect of milling speed

Figure 4.7 shows the XRD pattern of $Cu(In_{0.5},Ga_{0.5})Se_2$ powder prepared at different milling speed. XRD pattern of powder milled at 200 rpm shows a small intense peak at 29.68º, in addition to the peak corresponding to $Cu(In_{0.5},Ga_{0.5})Se_2$ phase, which is assigned to In_6Se_7 binary phase according to JCPDS 00-025-0385. The powder milled at 250,300,350 and 400 rpm shows peaks related to single chalcopyrite phase of $Cu(In_{0.5},Ga_{0.5})Se_2$.

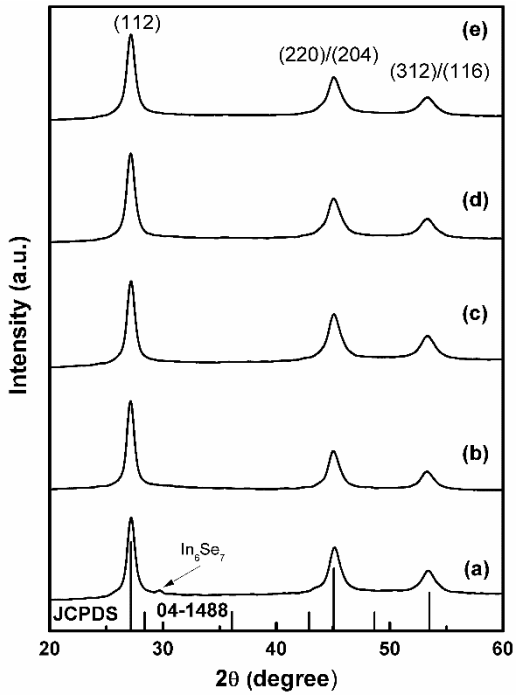

Fig.4.7. X-ray diffraction patterns of the $Cu(In_{0.5},Ga_{0.5})Se_2$ powder prepared at different milling speed: (a) 200 rpm; (b) 250 rpm; (c) 300 rpm; (d) 350 rpm and (e) 400 rpm.

As the milling speed increases, the energy input to the milling increases. Based on the model developed by Abdellaoui and Gaffet [4.18], the collision and kinetic energy of balls in the milling are obtained by

$$\|V_c\|^2 = (R\Omega)^2 + (r - r_b)^2\omega^2(1 + \frac{2\omega}{\Omega}) \quad \text{(Eq. : 4.12)}$$

$$E_k = \frac{1}{2}m\|V_c\|^2 \quad \text{(Eq. : 4.13)}$$

Where R is the distance between disc center and the vial center, r is the vial radius, r_b is the ball radius, Ω is the disc rotation speed, ω is the vial rotation speed and m is the ball mass. From this as the milling speed increases, the energy input into the powder increases. Since the energy input increases with increasing milling speed from 200 to 250 rpm, pure single phase of chalcopyrite $Cu(In_{0.5},Ga_{0.5})Se_2$ formation take place.

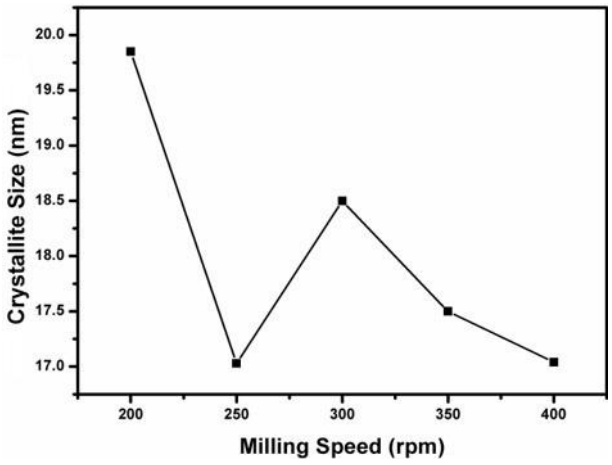

Fig.4.8. The crystallite size of $Cu(In_{0.5},Ga_{0.5})Se_2$ powder versus milling speed.

The crystallite size of the milled powder with respect to (112) plane is calculated from the XRD pattern given in figure 4.8 and is found to decrease from 19.8 to 17.03 nm by increasing milling speed from 200 to 250 rpm. Then, the crystallite size increases to 18.49 nm and subsequently decrease to 17.49 and 17.03 nm upon increasing milling speed to 300, 350 and 400 rpm. A similar change in crystallite size with milling speed has reported by Gheisari et.al. [4.19].

FESEM images of $Cu(In_{0.5},Ga_{0.5})Se_2$ particles obtained after milling for 2 h with BPR of 25:1 at 200, 250, 300, 350 and 400 rpm are shown in figure 4.9. The sample obtained with 200 rpm reveals spherical and plate-like structures. The plate-like structures could be due to flattening of materials during milling. The structures are strongly welded. $CuIn_{0.5}Ga_{0.5}Se_2$ particles milled with 250, 300 and 350 rpm show similar morphology. Relative to figure 4.9(c), the size of cold welded grains is found to be larger in figure 4.9(d). The disappearance of plate-like structures is observed with increasing milling speed. Sample milled with 400 rpm shows more defined spherical particles along with bigger aggregates of cold welded grains.

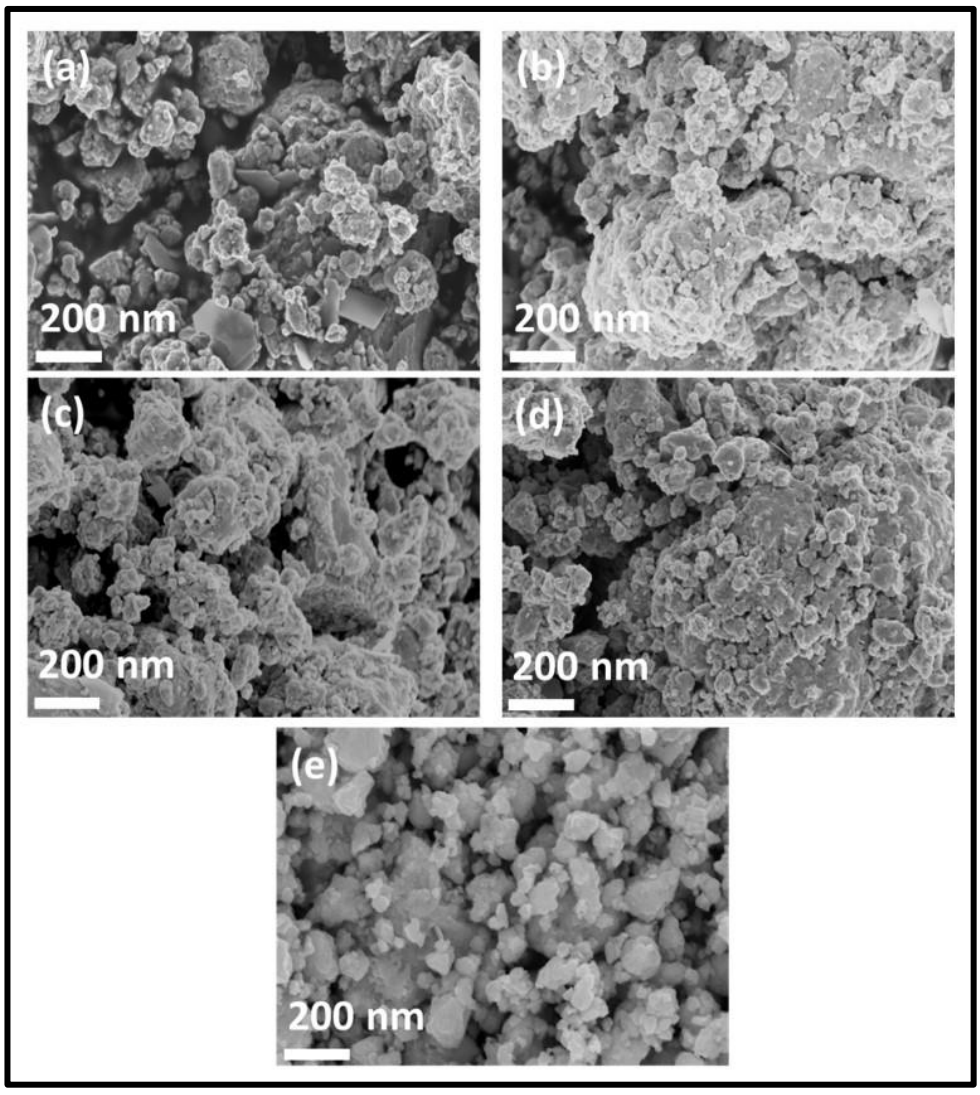

Fig.4.9. FESEM images of the $Cu(In_{0.5},Ga_{0.5})Se_2$ powder synthesized at different milling speed: (a) 200 rpm; (b) 250 rpm; (c) 300 rpm; (d) 350 rpm and (e) 400 rpm.

Table 4.3. EDAX composition analysis of $Cu(In_{0.5},Ga_{0.5})Se_2$ powder synthesized at different milling speed.

Sample	Atomic percentage of elements (at.%)				Cu/(In+Ga)	Ga/(In+Ga)
	Cu	In	Ga	Se		
200 rpm	27.23	10.42	13.99	48.36	1.11	0.57
250 rpm	27.94	9.90	13.15	49.01	1.21	0.57
300 rpm	27.47	10.84	12.93	48.76	1.15	0.54
350 rpm	28.04	11.54	12.71	47.71	1.16	0.52
400 rpm	27.55	11.40	12.65	48.40	1.14	0.52

The EDAX composition analysis (table 4.3) of the milled powders are analysed at operating voltage of 20 kV, and shows a difference in the value of Ga/(In+Ga) and Cu/(In+Ga) with changing milling speed. A non-linear variation in the atomic percentage of In with milling speed varying from 200 to 300 rpm could be due to the non-homogenous distribution of elements in the sample. Increasing milling speed seems to have no effect on controlling atomic percentage of the Cu and Se as compared to milling time and BPR while an increase in atomic percentage of In and decreasing atomic percentages of Ga are observed with increasing milling speed.

Hence by considering the structural, morphological and compositional properties, BPR of 25:1, milling time of 2 h and milling speed of 400 rpm is confirmed as the optimum conditions to synthesize $Cu(In_{0.5},Ga_{0.5})Se_2$ powder.

4.2. Mechanochemical Synthesis of $Cu(In_{0.7},Ga_{0.3})Se_2$ powder

It is reported that high efficiency CIGSe-based solar cell consists of Ga/(In+Ga) =0.3 [4.20,4.21]. Therefore, $Cu(In_{0.7},Ga_{0.3})Se_2$ alloy powder is prepared using the optimized milling condition i.e. BPR-25:1, milling speed- 400 rpm and milling time- 2 h.

Figure 4.10 represents the XRD pattern of $Cu(In_{0.7},Ga_{0.3})Se_2$ and $Cu(In_{0.5},Ga_{0.5})Se_2$ powder. The peak position of (112), (220)/(204) and (312)/(116) planes are shifted to

lower 2θ value with decreasing Ga/(In+Ga) to 0.3 from 0.5. In other words, it can be said as XRD peak position shift towards higher 2θ with increasing Ga content. It is explained based on the ionic radius of In and Ga. The ionic radius of In and Ga are 0.81 and 0.62 Å respectively. Hence the substitution of larger In atoms by smaller Ga atoms cause a decrease in lattice spacing [4.22]. It can be seen clearly from the figure 4.10 (B).

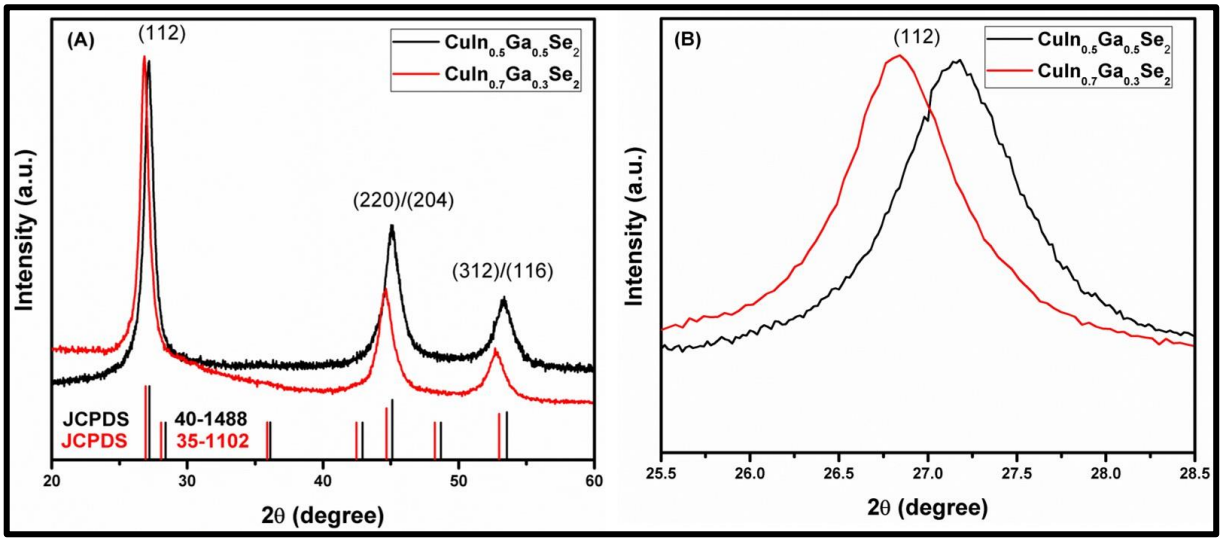

Fig.4.10. (A) XRD pattern of $Cu(In_{0.7},Ga_{0.3})Se_2$ and $Cu(In_{0.5},Ga_{0.5})Se_2$ powder and (B) magnified (112) peak of $Cu(In_{0.7},Ga_{0.3})Se_2$ and $Cu(In_{0.5},Ga_{0.5})Se_2$ powder.

The stoichiometry of Ga/(In+Ga) can be deduced using Vagard's law. Vagard's law is an empirical rule to determine unit cell parameters of a solid solution series in an alloy. According to Vagard's law, unit cell parameters decrease linearly as more Ga replaces In [4.23]. The plot of variation in lattice parameter with Ga/(In+Ga) is shown in figure 4.11. The unit cell parameter a and c for $Cu(In_{0.7},Ga_{0.3})Se_2$ and $Cu(In_{0.5},Ga_{0.5})Se_2$ are calculated as a= 5.74; c= 11.589 Å and a= 5.69 c= 11.305 Å respectively.

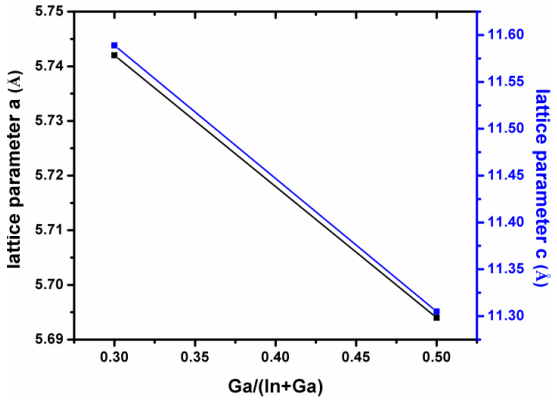

Fig.4.11. Lattice parameters "a" and "c" as a function of Ga/(In+Ga) in CIGSe powder.

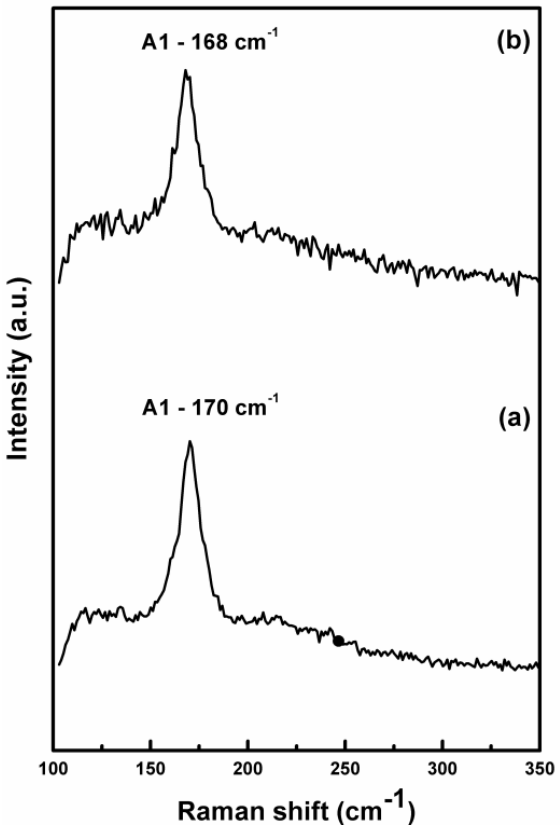

Fig.4.12. Raman spectra of (a) $Cu(In_{0.5},Ga_{0.5})Se_2$ and (b) $Cu(In_{0.7},Ga_{0.3})Se_2$ powder.

Raman spectra (figure 4.12) exhibit intense line at 170 and 168 cm^{-1} for the powders $Cu(In_{0.5},Ga_{0.5})Se_2$ and $Cu(In_{0.7},Ga_{0.3})Se_2$ respectively. It is evidently due to A1 phonon vibrational mode as it is the strongest vibrational mode observed in CIGSe-chalcopyrite compounds. As discussed earlier, this vibrational mode results from the motion of Se atom with Cu and In/Ga atoms remaining at rest [4.24]. This shift

observed in Raman peak position to higher wavenumber with an increase in Ga content is in good agreement with Papadimitriou et.al [4.25].

FESEM image of $Cu(In_{0.7},Ga_{0.3})Se_2$ powder is presented in figure 4.13, and it shows agglomerated spherical particles and non-spherical structures. Particles have inhomogeneous size distribution. EDAX analysis shows the composition of Cu, In, Ga and Se as 26.02, 16.7, 9.2 and 47.6 at % respectively resulting in the formation of $Cu_1(In_{0.67},Ga_{0.33})Se_{1.9}$ which is close to $Cu(In_{0.7},Ga_{0.3})Se_2$. The band gap of $Cu(In_{0.7},Ga_{0.3})Se_2$ powder was determined from the measured absorbance (A) using the formula.

$$\alpha = A\,(h\vartheta - Eg)^{1/2} \qquad \text{(Eq. : 4.14)}$$

Where α is the absorption coefficient, A is a constant, Eg is the energy band gap and *hv* is the incident photon energy. Figure 4.13 (B) shows the plot of $(\alpha hv)^2$ as a function of incident photon energy for $Cu(In_{0.7},Ga_{0.3})Se_2$ powder. The estimated direct optical band gap is obtained by extrapolation of the $(\alpha hv)^2$ versus *hv* plot at $\alpha=0$. The estimated optical band gap of $Cu(In_{0.7},Ga_{0.3})Se_2$ powder is consistent with the reported values in the literature 1.1-1.2 eV [4.26]. However, the curve obtained by plotting $(\alpha hv)^2$ versus *hv* indicates the existence of defect states in the synthesized $Cu(In_{0.7},Ga_{0.3})Se_2$ powder.

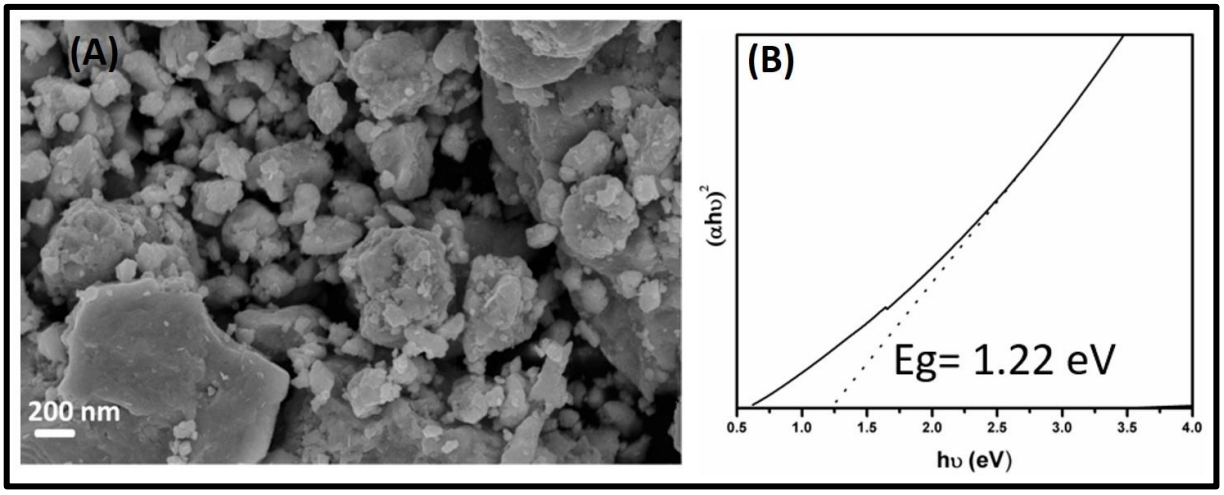

Fig.4.13. (A) FESEM image and (B) UV-Visible absorption spectrum of $Cu(In_{0.7},Ga_{0.3})Se_2$ powder.

4.3. Formulation of $Cu(In_{0.7},Ga_{0.3})Se_2$ particle- based ink

As-synthesized $Cu(In_{0.7},Ga_{0.3})Se_2$ particles are ultrasonicated in Ethanol for 1 h to break the agglomerates. The $Cu(In_{0.7},Ga_{0.3})Se_2$ particles in Ethanol settles down fast as the dispersion is unstable. The instability of dispersion mainly comes from the strongly agglomerate nature of mechanically synthesized particles. There are different methods such as electrostatic, steric and electro-steric stabilization mechanisms to form stable dispersions [4.27]. A long-term stability of dispersion is necessary for the industrial feasibility of methods. Steric stabilization method is availed in this work to improve the stability of $Cu(In_{0.7},Ga_{0.3})Se_2$ particle dispersions and ink is prepared as described in section 3.2. A Terpineol-Ethyl cellulose mixture is used as dispersing agent and binder respectively. The ink stability is analyzed with varying Ethyl Cellulose and Terpineol content which is shown in Figure.4.14.

Fig.4.14. The variation in stability of $Cu(In_{0.7},Ga_{0.3})Se_2$ ink formulated with EC and Terpineol, a,b,c,d,e: 40 wt% of Terpineol with EC wt %-0,1,2,3 and 4 respectively; f,g,h,i,j: 2 wt % of EC with Terpineol wt% -0,10,20,30 and 40 respectively.

It is observed that dispersion stability increased with Ethyl Cellulose content. Ink formulated without Ethyl Cellulose shows poor stability and particles settle down within a few hours. While, ink formulated using 2, 3 and 4 wt% of EC with 40 wt % of Terpineol is stable. So that 2 wt% of EC is used for further ink formulation. Also, it is observed that viscosity of the ink increases with Ethyl Cellulose content. Here Ethyl Cellulose acts as a binder, which provides improved wetting, delay in sedimentation and increase in viscosity [4.28]. On the other hand, the stability of ink suspension is found to be unaffected with the amount of Terpineol added. But the viscosity of ink is observed to be decreasing with increasing terpineol from 0 to 40 wt %. We assume that it can be due to breakage of large EC lattice by terpineol thus reducing viscosity of the ink. The role of Terpineol as a dispersing agent can be understood clearly from the AFM images of thin films from ink formulated with different Terpineol content (Fig.4.15). The dispersion of $Cu(In_{0.7},Ga_{0.3})Se_2$ particles is improved with increasing Terpineol content. The thin film deposited using ink with 40 wt% of Terpineol shows well-dispersed particles. Hence for further experiments, $Cu(In_{0.7},Ga_{0.3})Se_2$ ink is formulated using 2wt% EC and 40 wt % of Terpineol.

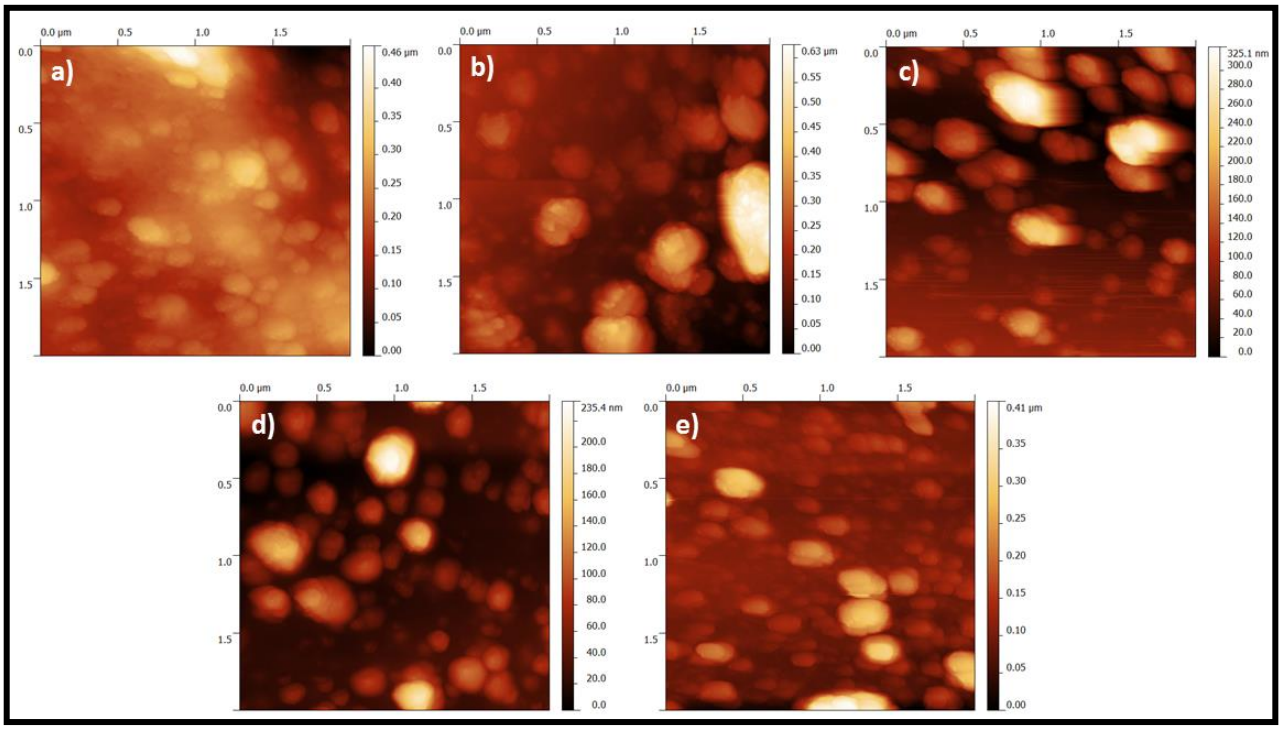

Fig.4.15. AFM topographic image of $Cu(In_{0.7},Ga_{0.3})Se_2$ thin film with Terpineol varying from a) 0 wt%, b) 10 wt%, c) 20 wt%, d) 30 wt% and e) 40 wt%.

4.4. Properties of $Cu(In_{0.7},Ga_{0.3})Se_2$ films

$Cu(In_{0.7},Ga_{0.3})Se_2$ films are deposited on a glass substrate using the ink formulated by adding 2 wt% of Ethyl Cellulose and 40 wt % of Terpineol to 1.5 g of $Cu(In_{0.7},Ga_{0.3})Se_2$ powder. The properties of as-deposited, air-annealed and selenized films are described in this section.

4.4.1. As- deposited $Cu(In_{0.7},Ga_{0.3})Se_2$ films

$Cu(In_{0.7},Ga_{0.3})Se_2$ film is deposited on glass substrate by doctor blade deposition as described in section 3.3.3. Film is dried at 80 ^{0}C for 30 minutes to evaporate Ethanol. These films are named as “as-deposited film”.

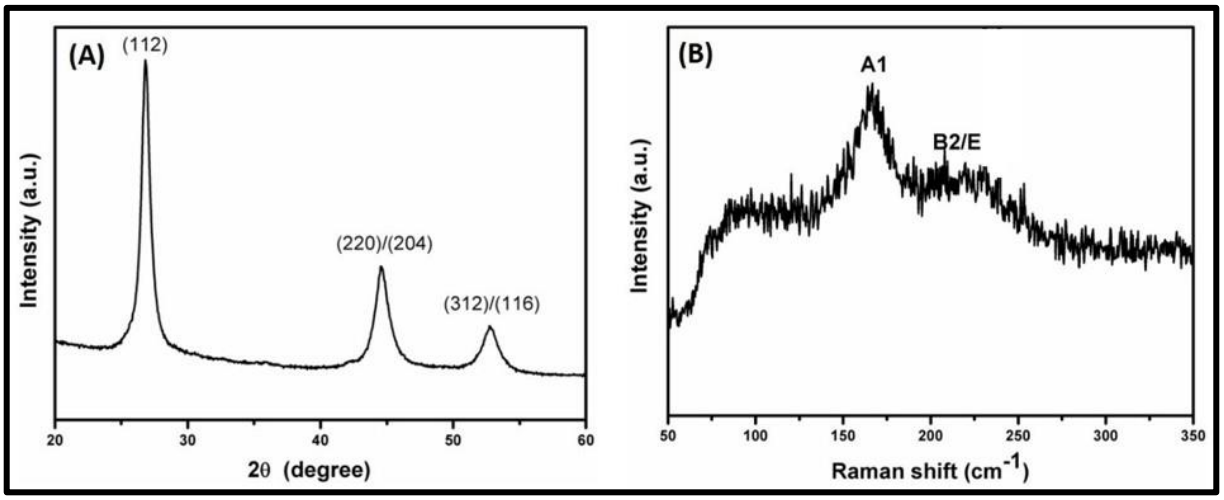

Fig.4.16. (A) XRD pattern and (B) Raman spectrum of as-deposited $Cu(In_{0.7},Ga_{0.3})Se_2$ film.

XRD pattern of as-deposited $Cu(In_{0.7},Ga_{0.3})Se_2$ film is shown in figure 4.16 (A). It reflects (112), (220)/(204) and (312)/(116) planes of chalcopyrite phase of $Cu(In_{0.7},Ga_{0.3})Se_2$ as observed in the synthesized powder. It indicates that crystalline properties of $Cu(In_{0.7},Ga_{0.3})Se_2$ powder are transferred to the film successfully. The absence of additional diffraction peaks or shift in peak position compared to precursor material also give light to the fact that the composition of precursor material is

preserved in the film too. This is one of the advantages of using particles based non-vacuum deposition of $Cu(In_{0.7},Ga_{0.3})Se_2$ films [4.29]. Raman analysis of $Cu(In_{0.7},Ga_{0.3})Se_2$ film is shown in Figure 4 .16 (B). It shows peaks at 168 and 230 cm^{-1} which correspond to A1 and E/B2 phonon vibrational mode of chalcopyrite phase of $Cu(In_{0.7},Ga_{0.3})Se_2$.

Figure 4.17 shows the cross-sectional morphology of as-deposited $Cu(In_{0.7},Ga_{0.3})Se_2$ film. It shows how the mechanochemically synthesized $Cu(In_{0.7},Ga_{0.3})Se_2$ powder are covered with the organic additives while forming film. Through the cross-section FESEM analysis shown in figure 4.17, film consists of smaller and bigger particles. Also, the as-deposited film contains a greater amount of organic additives as marked by the red circles. These organic additives must be removed as it hinders the grain growth during annealing and affects the performance of photovoltaic device [4.30]. The thickness of as-deposited film is found to be 15 µm. The composition of this sample was not measured due to charging up of the film during EDAX analysis because of organic additives present in the film.

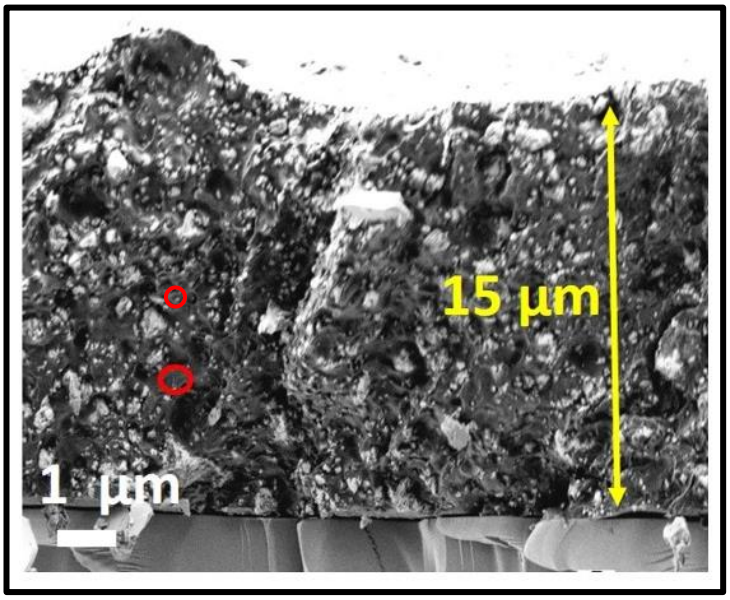

Fig.4.17. Cross-sectional FESEM image of as-deposited $Cu(In_{0.7},Ga_{0.3})Se_2$ film.

4.4.2. Annealing of $Cu(In_{0.7},Ga_{0.3})Se_2$ films

The as-deposited $Cu(In_{0.7},Ga_{0.3})Se_2$ films are annealed in ambient atmosphere to remove the organic additives added during ink preparation. Annealing temperatures are chosen as 300 and 400 ºC for 1 h. EDAX composition analysis is carried out at operating voltage of 20 kV and is used to identify the amount of Carbon content in the annealed $Cu(In_{0.7},Ga_{0.3})Se_2$ films (table 4.4).

Table 4.4. EDAX composition data of $Cu(In_{0.7},Ga_{0.3})Se_2$ films annealed at 300 and 400˚C.

Film annealed at	Atomic percentage of elements (at.%)					Ga/ (In+Ga)	Cu/ (In+Ga)	Cu/Se
	C	Cu	In	Ga	Se			
300˚C	40	25.17	20.14	7.41	47.28	0.27	0.91	0.53
400˚C	32	33.25	29.11	9.13	28.51	0.24	0.86	1.16

From table 4.4, it is found that annealing at 400 ˚C is beneficial for removing C content from the as-deposited $Cu(In_{0.7},Ga_{0.3})Se_2$ films. However, atomic percentage of Se is reduced from 47.6 at.% in the mechanochemically synthesized powder to 28.51 at % after annealing at 400 ˚C. While film annealed at 300 ˚C retains the Se content as 47.28 at %. It indicates the occurrence of loss of Se during annealing at 400 ˚C. Also, film annealed at 400 ˚C is Cu-rich with Cu/Se ratio of 1.16. It is well known that CIGSe film with Cu-rich composition has poor photovoltaic performance due to the presence of residual $Cu_{2-x}Se$ phase [4.31].

XRD pattern of films annealed at 300 and 400 ˚C are shown in figure 4.18 (A). Film annealed at 300 ˚C exhibits crystalline structure similar to the as-deposited $CuIn_{0.7}Ga_{0.3}Se_2$ film, whose diffraction peak appeared at (112), (220)/(204), (312)/(116) planes of chalcopyrite $Cu(In_{0.7},Ga_{0.3})Se_2$.These peaks are narrower with FWHM of (112) plane as 0.53 and sharp for the as- deposited $Cu(In_{0.7},Ga_{0.3})Se_2$ films. However, the film annealed at 400 ˚C presents peaks related to binary phases Cu_2Se,Ga_2Se_3,InSe,CuSe,$CuSe_2$ and CISe in addition to (112) plane of CIGSe. The occurence of binary phases is due to decomposition of $Cu(In_{0.7},Ga_{0.3})Se_2$ arising from

the loss of selenium which is evidenced from EDAX data. The FWHM of (112) plane is calculated to be 0.31 which is narrower than the film annealed at 300 ˚C.

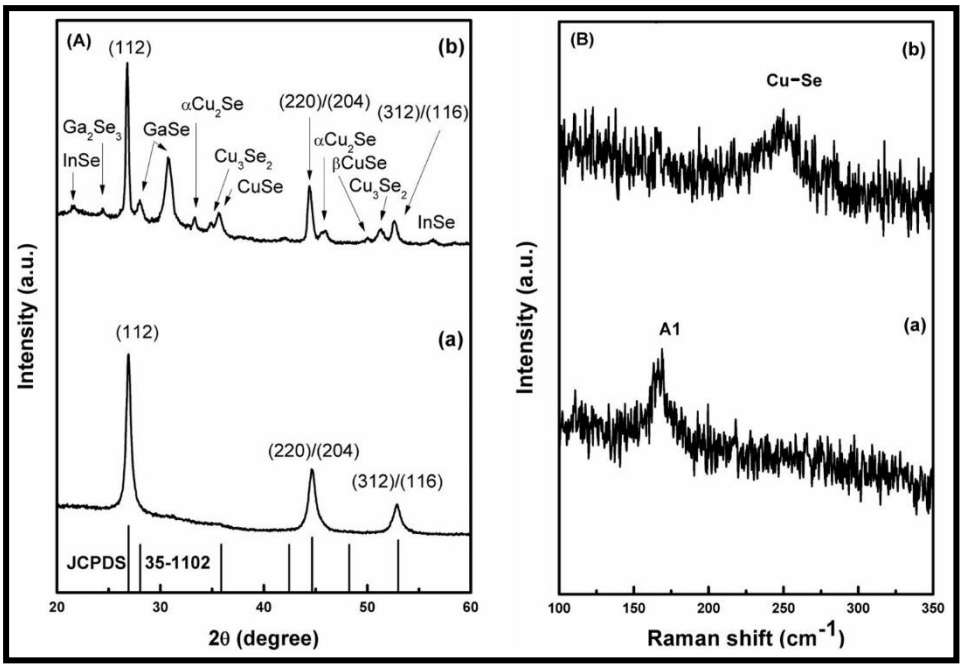

Fig.4.18. (A) XRD pattern and (B) Raman spectra of $Cu(In_{0.7},Ga_{0.3})Se_2$ film annealed at (a) 300 and (b) 400 ˚C.

The figure 4.18.(B) shows Raman spectra of annealed $Cu(In_{0.7},Ga_{0.3})Se_2$ films. Film annealed at 300 ˚C shows Raman shift at 168 cm^{-1} which is at the same position as observed in the as-deposited film. While the film annealed at 400 ˚C shows a peak at 259 cm^{-1} indicating presence of Cu-Se phase in the sample. Also, Raman spectra do not exhibit peak related to $Cu(In_{0.7},Ga_{0.3})Se_2$ phase, which is in contrast to the $Cu(In_{0.7},Ga_{0.3})Se_2$ peaks observed in the XRD. It could be inferred that during annealing, Se loss occurs primarily from the film surface so that $Cu(In_{0.7},Ga_{0.3})Se_2$ in the upper part of the film was decomposed and became Copper-rich. As Raman analysis is a surface characterization technique,peak related to Cu-Se phase was only detected.

The planar and cross-sectional FESEM image of the sample annealed at 300 and 400 ˚C are presented in figure 4.19. Both the films show similar surface morphology in the planar view. The thickness of films is 7.7 and 7µm for films annealed at 300 and 400 ˚C respectively which are half of the thickness of the as-deposited film.The reduction in thickness is due to the removal of organic additives from the film during annealing.

Film annealed at 300 ˚C is found to be compact and dense with bigger grains relative to film annealed at 400 ˚C. It is important here to note that, the cross-sectional image of annealed film is quite different from the as-deposited film. The organic additives observed in the as-deposited film is lessend/unable to view after the annealing treatment.

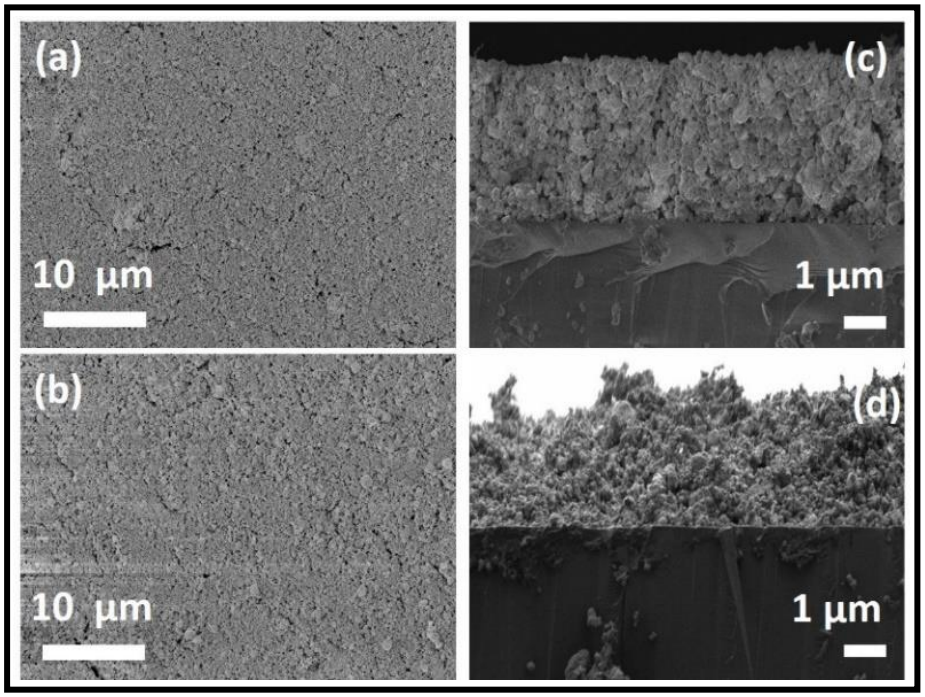

Fig.4.19. Planar (left) and cross-sectional (right) FESEM images of $Cu(In_{0.7},Ga_{0.3})Se_2$ films annealed at 300 ˚C (a and c) and 400 ˚C (b and d).

4.4.3. Selenization of $Cu(In_{0.7},Ga_{0.3})Se_2$ film

Films annealed at 300 and 400 ˚C are heat treated at 550 ˚C in Se atmosphere. The experimental conditions are same as discussed in section 3.4.Selenized films are named as Film 300-Se and Film 400-Se respectively. XRD pattern of Film 300-Se and Film 400-Se are given in figure 4.20 (A). The Film 300-Se exhibits reflections from (112), (220)/(204), (312)/(116) planes of chalcopyrite $Cu(In_{0.7},Ga_{0.3})Se_2$ as observed in the annealed films (Figure .4.18) in addition to the small peaks corresponding to (103), (211), (213)/(105) and (301) planes of $Cu(In_{0.7},Ga_{0.3})Se_2$.

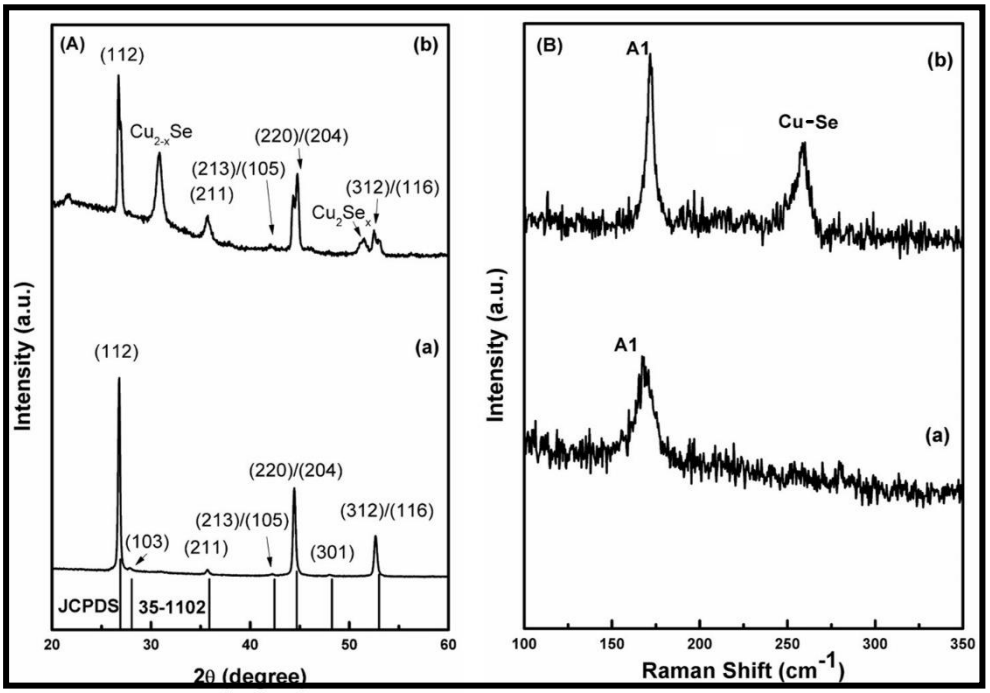

Fig.4.20. (A) XRD pattern and (B) Raman spectra of (a) Film 300-Se and (b) Film 400-Se.

These planes were absent in the powder, as-deposited film and annealed film. However, the peak position of (112),(220)/(204) and (312)/(116) planes are shifted from 26.92˚, 44.68˚ and 52.87˚ to 26.8˚, 44.4˚ and 52.64˚. The XRD peaks become narrow and sharp after selenization.FWHM of (112) plane in the selenized film is found to be 0.24 which is half that of annealed films (0.53).This indicates improvement in the crystalline quality of films after selenization [4.32]. While XRD pattern of Film 400-Se exhibits diffraction peaks related to (112), (220)/(204) and (312)/(116) planes of $Cu(In_{0.7},Ga_{0.3})Se_2$ and planes related to Cu-Se phases. The other secondary phases appeared due to air annealing at 400 ˚C is disappeared. It notifies that reaction occurs among In-Se, Ga-Se, Cu-Se and CISe compounds and leads to the formation of $Cu(In_{0.7},Ga_{0.3})Se_2$ during selenization. The peaks are narrower and sharp with FWHM of (112) plane equal to 0.17 which is smaller than that for Film 300-Se. The peaks for (112), (220)/(204) and (312)/(116) planes are found as splitted. Kaigawa et.al [4.33] has explained the observed XRD peak splitting in $CuIn_{0.7}Ga_{0.3}Se_2$ films on the basis of Ga gradient present throughout the film with the evidence from SIMS studies. Raman spectroscopy shown in figure .4.20 (B) indicates chalcopyrite phase of $Cu(In_{0.7},Ga_{0.3})Se_2$ film by giving a peak at 168 and 171 cm^{-1} for Film 300-Se and Film

400-Se respectively. The A1 phonon mode peak is narrower in the Film 400-Se compared to Film 300-Se. This again indicates that annealing at 400 ˚C helps to improve the crystalline quality of selenized films [4.34]. However, an intense peak at 259 cm^{-1} is also present in the Film 400-Se. This peak is assigned to Cu-Se phases [4.35].

Table 4.5. EDAX composition data of Film 300-Se and Film 400-Se.

Film	Atomic percentage of elements (at.%)					Ga/ (In+Ga)	Cu/ (In+Ga)	Cu/Se
	C	Cu	In	Ga	Se			
300-Se	30.73	24.40	17.82	8.35	49.43	0.31	0.93	0.49
400-Se	27.81	35.15	25.84	11.62	27.39	0.31	0.93	1.28

The EDAX analysis of selenized films are carried out at operating voltage of 20 kV, and the obtained data is given in table 4.5. It is worth to note that the Carbon content in the annealed films are reduced to 30.7 and 27.8 at.% from 40 and 32 at.% after selenization.The difference in Carbon content between Film 300-Se and Film 400-Se are negligible. Se content in the Film 300-Se is increased to 49.43 from 47.28 at % making Cu/Se equal to 0.5. The Ga/(In+Ga) is found as 0.31 which is exactly same as in the mechanochemically synthesized $Cu(In_{0.7},Ga_{0.3})Se_2$ powder. In the case of Film 400-Se, selenization didn't help to compensate the Se loss occurred during annealing at 400 ˚C. The atomic percentage of Se remained as 27 % making the selenized film Cu-rich with Cu/Se=1.28. The Cu-rich composition lead to the formation of Cu-Se phases which is confirmed by XRD and Raman analyses. The Ga/(In+Ga) and Cu/(In+Ga) are 0.31 and 0.93 respectively which are as same as the selenized film annealed at 300 ˚C. From this, we can elucidate that, Ga or In is not evaporated from the sample during annealing at 400 ˚C. However, as $Cu(In_{0.7},Ga_{0.3})Se_2$ was decomposed to binary selenides during annealing at 400 ˚C and an inhomogeneity in Ga distribution was developed which leads to the development of Ga gradient during selenization.

The planar and cross-sectional FESEM images of Film 300-Se and Film 400-Se are shown in figure 4.21. The Film 300-Se shows dense surface morphology with small cracks. Whilst, Film 400-Se shows porous and irregular surface morphology. Also, it shows poor adherence to the substrate. Both Film 300-Se and Film 400-Se shows thickness of 10 µm. Cross-sectional images of Film 300-Se and Film 400-Se shows particles resembling the mechanochemically synthesized particles without showing grain growth. The poor grain growth shown by $Cu(In_{0.7},Ga_{0.3})Se_2$ particle-based film has been reported by many [4.36,4.37]. It can be attributed to the high covalent nature of CIGSe alloy.

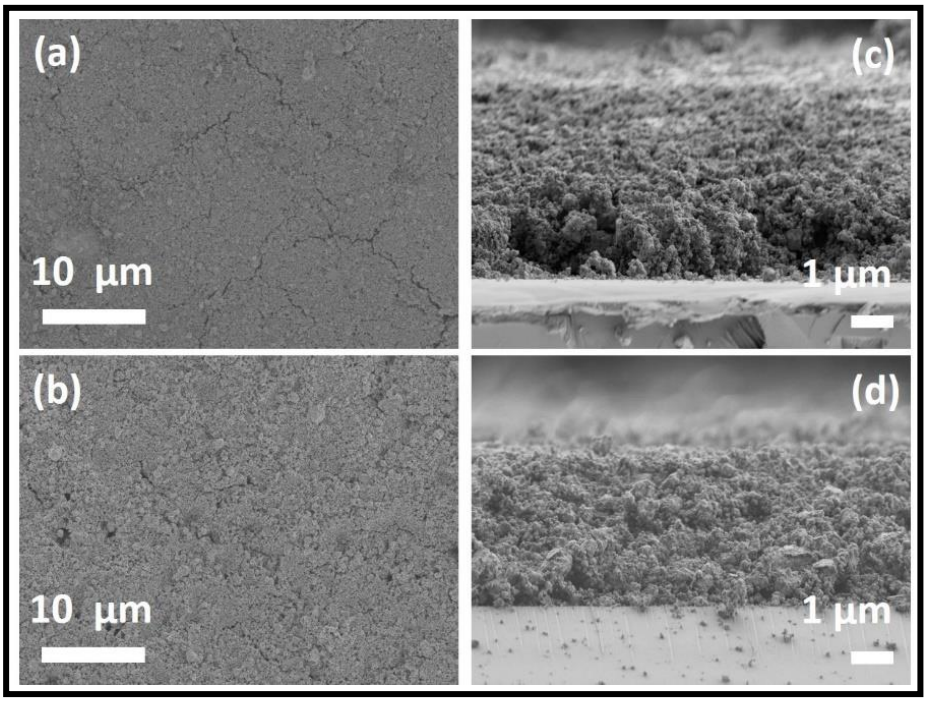

Fig.4.21. Planar (right) and cross-sectional (left) FESEM images of Film 300-Se (a and c) and (b and d) Film 400-Se.

Since Film 300-Se shows superior structural and compositional properties with good adhesion to the substrate, it is chosen for further characterizations.

4.4.4. The electrical properties of $Cu(In_{0.7},Ga_{0.3})Se_2$ film

The conductivity type, carrier concentration, mobility and resistivity of Film 300-Se is given in table 4.6. It shows that $Cu(In_{0.7},Ga_{0.3})Se_2$ film has p-type conductivity with carrier concentration (holes) of 5.5 X 10^{17} cm^{-3}, mobility of 0.0368 cm^2/Vs, and resistivity of $3.066X10^2$ Ωcm. As discussed in chapter 2, section 2.2.3, the electrical properties of CIGSe films are very much dependent on the deposition process and the composition.The reported values for carrier concentration, mobility, and resistivity of CIGSe films are given in table 2.1. It is important to mention here that there are very few reports available on the electrical properties of CIGSe film deposited by the non-vacuum process, especially by particle-based ink coating method. B.Vidhya [4.38] deposited CIGSe film by screen printing of mechanochemically synthesized CIGSe particle-based ink and reported the electrical properties based on Hall studies (table 2.1). Compared to the result of B.Vidhya [4.38], the films in this study exhibited an enhancement in carrier concentration (10^{17} cm^{-3}) and reduction in film resistivity. However, the film studied in this work has low mobility. Jo et.al [4.39] studied the effect of substrate temperature on the electrical properties and found that carrier concentration increases while mobility and resistivity decrease with increasing temperature from 30 to 500 ˚C. Similarly, the increased carrier concentration, lower mobility, and resistivity compared to the values reported by B. Vidhya [4.38] can be attributed to the effect of selenization process carried out at 550 ˚C in this work. Selenization process helps to attain enhanced crystallization which results in improved carrier concentration and lowers the resistivity. Compared to the values reported for CIGSe films deposited by vacuum methods (table 2.1), the Film 300-Se shows inferior electrical properties. It has to be noted that, films deposited by vacuum process are dense and non-porous with large grains. As a result, the height of the potential barrier for the charge carriers during electrical transport is very low, and the charge carriers have to cross a minimum number of grain boundaries [4.40]. Hence, the resistivity of the films is less. From the cross-sectional FESEM images shown in figure 4.21, it can be seen that Film 300-Se consists of smaller grains which contribute higher density of grain boundaries that act as a barrier to the flow of charge carriers. This leads to higher resistivity and lower mobility of charge carriers [4.41].

Table 4.6. Conductivity type, carrier concentration,mobility and resistivity of $Cu(In_{0.7},Ga_{0.3})Se_2$ film (Film 300-Se).

Film	Type of conductivity	Carrier concentration (cm^{-3})	Mobility (cm^2/Vs)	Resistivity (Ωcm)
300-Se	p	5.505×10^{17}	0.0368	3.066×10^2

The type of conductivity and resistivity can also be explained on the basis of the composition of CIGSe. The composition of constituent elements in the CIGSe has a crucial role in determining the conductivity type and resistivity of the film. Deviation from the stoichiometric composition can result in the formation of native defects such as vacancies and interstitials. A defect type of cation vacancies or anion interstitials is responsible for p-type conductivity. The general way of controlling carrier type and concentration in CIGSe is by adjusting the Cu concentration since Cu vacancies have a vital role in determining the p-type conductivity of CIGSe.Cu-vacancy act as an acceptor.Excess of Cu can lead to an n-type conductivity of CIGSe, since excess Cu either goes to interstitial positions or could promote Se vacancies. Cu at interstitial position and vacancy of Se act as donors. A systematic investigation was carried out by R.Noufi et.al [4.42] to correlate stoichiometry of CISe to the electrical properties with respect to the carrier concentration and reported that Cu vacancy is most responsible for the p-type conductivity of CISe. According to their results, If Se/(Cu+In) is lesser than 1 and Cu/In is smaller than 1, the CISe film exhibits p-type conductivity with high resistivity.Also,it has to be taken into account that introduction of Ga to the CISe makes it more p-type, since CGSe has more holes and less compensating electrons than CISe. From the EDAX data for the Film 300-Se given in table 4.5, Se/(Cu+In+Ga) is 0.97 and Cu/(In+Ga) is 0.93. Comparing with the observation of Noufi et.al, Film 300-Se should have p-type conductivity and high resistivity which is in good agreement with the results obtained from the Hall measurements.

The photoresponse behaviour of CIGSe Film 300-Se is studied to examine it's potential as an absorber layer for photovoltaic applications. I-V characteristic of Film 300-Se is measured under dark as well as under illumination as described in section 3.6.8. Au contacts in the circular shape of 0.1 cm diameter is deposited on the film. The I-V measurements were carried out between two contacts separated by 0.2 cm.

The average thickness of Film 300-Se is 10 µm. A voltage of 10 V is applied across the two Au contacts as shown in figure 4.22. The resulting current flowing across the film between two contacts are measured. Followingly, the experiment is repeated under a light source of 300 W. The obtained I-V characteristic of Film 300-Se under dark and illumination is presented in Figure 4.23.

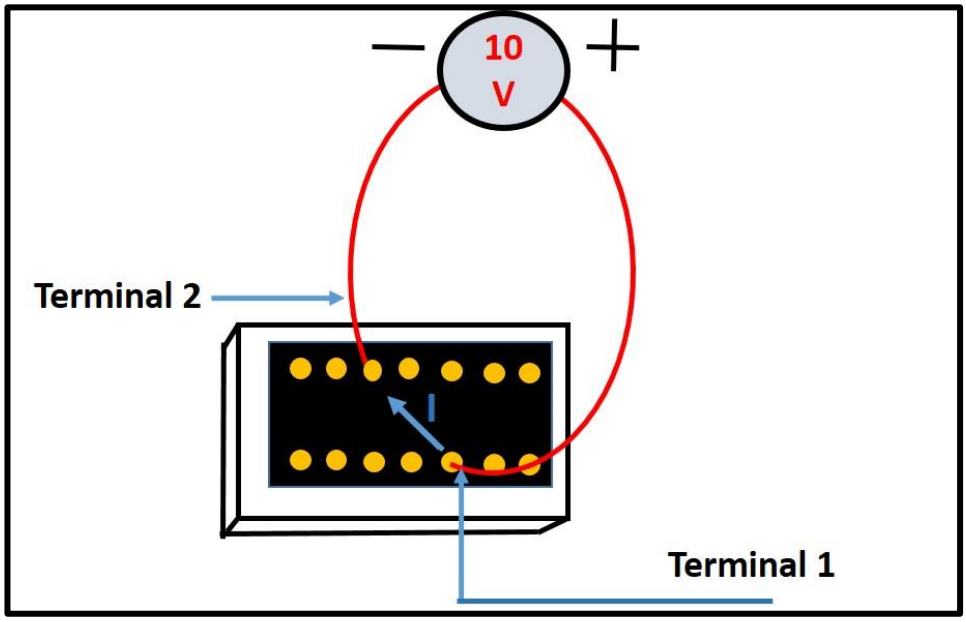

Fig.4.22. Schematic of I-V characterization measurement.

The Film 300-Se exhibits nearly linear current-voltage curve that is symmetric about the origin. The increase in current with voltage shows the ohmic behaviour of the contact. Upon illumination, current increases 1.11 times that of current under dark which is similar to the value reported for other semiconductor particle-based films [4.43,4.44]. This indicates the applicability of Film 300-Se for photovoltaic application. The resistivity of the film is calculated from the I-V measurements and it is found to be 1.63×10^2 and 1.38×10^2 Ωcm under dark and illumination, respectively which are in the same order with the value obtained from the Hall measurements. The two probe I-V measurement gives an approximate value of resistivity. Since the resistance of the film is high, the resistivity of the film obtained from two-probe I-V measurement can have variation from the value obtained from the Hall measurement. Upon illumination, the electrons in the valance band receive energy and excite to conduction band. The excitation of electrons increases the holes in the $Cu(In_{0.7},Ga_{0.3})Se_2$ film and thus enhances the conductivity (or reduces the resistivity).

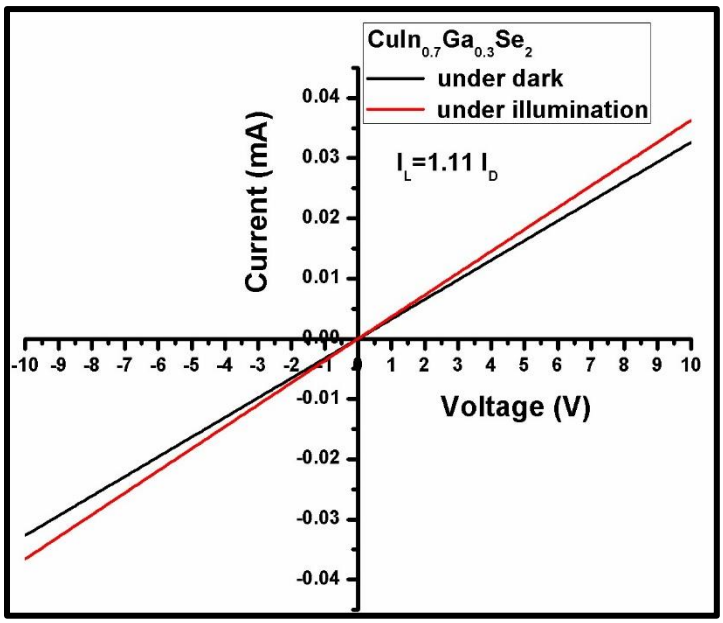

Fig.4.23. I-V characterisitc of Film 300-Se under dark and under illumination**.**

4.5. Summary

- ✓ $Cu(In_{0.5},Ga_{0.5})Se_2$ powder have been prepared mechanochemically using elemental Cu,In,Ga and Se as precursor materials. The effect of milling parameters such as milling time, ball to powder ratio and milling speed on the formation of single phase chalcopyrite $Cu(In_{0.5},Ga_{0.5})Se_2$ powder have been studied.
- ✓ Firstly, $Cu(In_{0.5},Ga_{0.5})Se_2$ powder have been prepared by keeping BPR as 15:1, milling speed as 400 rpm and milling time varies as 30 min, 1h, 1.5 h , 2 h, 4 h and 6 h. It is found that milling time of 6 h is required to form single-phase $Cu(In_{0.5},Ga_{0.5})Se_2$ powder. A shift in XRD peak position to lower 2 θ angles has been observed possibly due to stress induced during the milling process. The crystallite size of the particle is found to be decreased with increasing milling time. FESEM analysis shows changes in morphology of milled powder with milling time. The synthesized $Cu(In_{0.5},Ga_{0.5})Se_2$ powder particle are heavily agglomerated. EDAX analysis shows that higher milling time favours homogeneity in composition. The $Cu(In_{0.5},Ga_{0.5})Se_2$ powder obtained after 6 h of milling has a composition of $Cu_{1.04}(In_{0.49},Ga_{0.51})Se_{1.96}$.
- ✓ Further to reduce milling time, BPR has been increased to 20:1 and 25:1 and milling process is carried out for 2 and 1 h keeping milling speed as 400 rpm. It

is found that increasing BPR reduces the time required to form single-phase $Cu(In_{0.5},Ga_{0.5})Se_2$ as the energy input to the milling increases with increasing BPR. Single-phase $Cu(In_{0.5},Ga_{0.5})Se_2$ powder is mechanochemically synthesized in 2 h with BPR of 25:1 and milling speed of 400 rpm. The crystallite size varies non-linearly with BPR. Morphology of powder changes with milling time and shows that higher BPR favours fracturing process over welding process. From the EDAX results, it has been observed that with higher BPR, the atomic percentage of Cu and In increases while Se decreases slightly.

- ✓ Milling speed is the next process parameter to be taken for study. For this, $Cu(In_{0.5},Ga_{0.5})Se_2$ powder has been prepared by keeping BPR as 25:1, milling time as 2 h with milling speed vary as 200,250,300,350 and 400 rpm. Single phase chalcopyrite is found to form with milling speed of 250 rpm. The crystallite size varies nonlinearly with milling speed. However, $Cu(In_{0.5},Ga_{0.5})Se_2$ powder milled at 400 rpm showed less agglomerated morphology. Hence, the optimum parameter for mechanochemical synthesize of $Cu(In_{0.5},Ga_{0.5})Se_2$ is fixed as BPR of 25:1, milling speed of 400 rpm and milling time of 2 h.
- ✓ Further, $Cu(In_{0.7},Ga_{0.3})Se_2$ powder has been prepared using the optimum milling parameters. Increase in lattice constant a and c has been observed with reducing Ga content. Raman spectra show a shift in A1 vibrational mode to lower wavenumber with respect to reducing Ga. The composition of $Cu(In_{0.7},Ga_{0.3})Se_2$ powder is confirmed from the EDAX analysis. The synthesized $Cu(In_{0.7},Ga_{0.3})Se_2$ powder shows a bandgap of 1.2 eV.
- ✓ Later, mechanochemically synthesized $Cu(In_{0.7},Ga_{0.3})Se_2$ powder has been used for film preparation. Therefore, $Cu(In_{0.7},Ga_{0.3})Se_2$ particle-based ink has been formulated using Ethyl Cellulose and Terpineol as organic additives and Ethanol as solvent. The influence of the concentration of additives on the ink properties has been studied. It is found that Ethyl Cellulose serves as binder while Terpineol acts as dispersing agent. $Cu(In_{0.7},Ga_{0.3})Se_2$ ink with 2 wt % of EC and 40 wt% of Terpineol has been found as optimum for dispersing particles well with the minimum amount of organic additives.
- ✓ The properties of as-deposited films have been studied using XRD, RAMAN and FESEM analyses and found that as-deposited film preserves the structural properties of synthesized $Cu(In_{0.7},Ga_{0.3})Se_2$ powder. FESEM image shows that

as-deposited film consists of huge amount of organic additives which is detrimental to the performance of a photovoltaic device.

- ✓ The as-deposited films have been annealed at 300 and 400 ˚C in air for 1 h to eliminate the Carbon content, and structural, morphological and compositional properties of annealed films have been studied. It is found that annealing at 400 ˚C is beneficial for removal of Carbon. However, annealing at 400 ˚C causes loss of selenium which in turn results in decomposition of $Cu(In_{0.7},Ga_{0.3})Se_2$ phase into binary compounds. The film annealed at 300 ˚C has not shown Se deficiency, and it maintains the single chalcopyrite phase of $Cu(In_{0.7},Ga_{0.3})Se_2$.
- ✓ The films annealed at 300 and 400 ˚C are further heat treated under Se atmosphere at 550 ˚C. Selenized films showed improved crystalline properties compared to annealed films. Comparing selenized films which were previously annealed at 300 and 400 ˚C, film annealed at 300 ˚C showed superior structural, compositional, and morphological properties. Even though both films do not exhibit any grain growth due to the strong covalent bond character of $Cu(In_{0.7},Ga_{0.3})Se_2$ compound.
- ✓ The Hall effect study of $Cu(In_{0.7},Ga_{0.3})Se_2$ film (annealed at 300 ˚C after selenization) reveals carrier concentration of 10^{17} cm^{-3}, hole mobility of 0.0368 cm^2/Vs and resistivity of 3.06 $\times 10^2$ Ωcm. Lower mobility and higher resistivity of $Cu(In_{0.7},Ga_{0.3})Se_2$ film is attributed to higher density of grain boundaries which act as a barrier for the flow of charge carriers. Also, it exhibits photoconductivity which make it suitable for photovoltaic application.

References

4.1. B. Vidhya, S. Velumani, R. Asomoza, “Effect of milling time and heat treatment on the composition of $CuIn_{0.75}Ga_{0.25}Se_2$ nanoparticle precursors and films”, Journal of Nanoparticle Research 13 (2011) 3033-3042.

4.2. H.H. Sheu, M.E. Liu, Y.L. Tsai, “Phase evolution of $CuIn_{0.7}Ga_{0.3}Se_2$ compound powder prepared using high energy ball milling”, Powder Technology 269 (2015) 345-350.

4.3. D.L. Zhang, D.Y. Ying, “Solid state reactions in nanometer scaled diffusion couples prepared using high energy ball milling”, Material Science Engineering A 301 (2001) 216-221.

4.4. Y.S. Kwon, P.P. Choi, J.S. Kim, D.H. Kwon, K.B. Gerasimov, “Steady state products in the Fe-Ge system produced by mechanical alloying”, Journal of alloys and compounds 353 (2003)194-199.

4.5. C. Suryanarayana, “Mechanical alloying and milling”, Progress in Material Science 46 (2001) 1-184.

4.6. A.Y. Badmos, H.K.D.H Bhadeshia, “The evolution of solutions: a thermodynamic analysis of mechanical alloying”, Metallurgical and Material Trasactions A 28 (1997) 2189-2194.

4.7. E.R. Baek, V. Astini, A. Tirta, B. Kim, “Phase evolution of CIGS alloyed compound synthesis by direct melting method”, Current Applied Physics 11 (2011) s76-s80.

4.8. K.A. Sharifov, T.K. Azizov, A.S. Abbasov, F.M. Mustafayev, “Investigation of the thermodynamic properties of copper selenides”, Izv. Akad. Nauk Az. SSR, Ser. Fiz.-Tekh. Mat. Nauk. 1976 (1976) 137-139.

4.9. G.K. Efendiev, Z.S. Karaev, “Synthesis and study of rare earth sulfo selenogallates”, Khalkogenidy 1 (1965) 133-140.

4.10. G. Gattow, A. Schneider, “Standard enthalpies of formation of gallium and indium selenides (Ga_2Se_3 and In_2Se_3)”, Russian Journal of Physical Chemistry 41 (1967)645-646.

4.11. O. Knacke, O. Kubaschewski, K. Hesselmann, “Thermochemical properties of inorganic substances” Springer(1991).

4.12. H. Zuhailawati, Y. Mahani, “Effects of milling time on hardness and electrical conductivity of in situ Cu–NbC composite produced by mechanical alloying,” Journal of Alloys and Compounds, 476 (2009) 142-146.

4.13. Z. Xiao, Z. Li, M. Fang, S. Xiong, X. Sheng, M. Zhou, “Effect of processing of mechanical alloying and powder metallurgy on microstructure and properties of Cu-Al-Ni-Mn alloy”, Material Science Engineering A 488 (2008) 266-272.

4.14. L. Lu, M.O. Lai, S. Zhang, “Modeling of the mechanical–alloying process”, Journal of Materials Processing Technology 52 (1995) 539-546.

4.15. J.B. Fogagnolo, F. Velasco, M.H. Robert, J.M. Torralba, “Effect of mechanical alloying on the morphology, microstructure and properties of aluminium matrix composite powders”, Materials Science and Engineering A 342 (2003) 131-143.

4.16. B.J.M Aikin, T.H. Courtney, “The kinetics of composite particle formation during mechanical alloying”, Metallurgical Transactions A 24A (1993) 647-657.

4.17. M. Zakeria, M. Amezanib, A. Nazaric, “Effect of ball to powder ratio on the mechanochemical synthesis of $MoSi_2$-TiC nanocomposite powder”, Material Research 15(2012) 891-897.

4.18. M. Abdellaoui, E. Gaffet, “A mathematical and experimental dynamical phase diagram for ball-milled $Ni_{10}Zr_7$”, Journal of Alloys and Compound 209 (1994) 351-361.

4.19. Kh. Gheisari, S. Javadpour, J.T. Oh, M. Ghaffari, “The effect of milling speed on the structural properties of mechanically alloyed Fe-45%Ni powders”, Journal of Alloys and Compounds 472 (2009) 416-420.

4.20. M.A. Contreras, B. Egaas, K. Ramanathan, J. Hiltner, A. Swartzlander, F. Hasoon, R. Noufi, “Progress toward 20% efficiency in Cu(In,Ga)Se_2 polycrystalline thin-film solar cells”, Progress in Photovoltaics Research and Applications**7**(1999)311-316.

4.21. F.S. Hasoon, Y. Yan, H. Althani, K.M. Jones, H.R. Moutinho, J. Alleman, M.M. Al-Jassim, R. Noufi, “Microstructural properties of Cu(In,Ga)Se_2 thin films used in high-efficiency devices” Thin Solid Films 387(2001)1-5.

4.22. M.R. Balboul, H.W. Schock, S.A. Fayak, A. Abdel El-Aal, J.H. Werner, A.A. Ramadan, “Correlation of structure parameters of absorber layer with efficiency of Cu (In,Ga)Se_2 solar cell”, Applied Physics A 92 (2008) 557-563.

4.23. B. Rehani, J.R. Ray, C.J. Panchal, H. Master, R.R. Desai, P.B. Patel, “Mechanochemically synthesized CIGS nanocrystalline powder for solar cell application”, Journal of Nano and Electronic Physics 5 (2013) 02007-02011.

4.24. C. Rincon, F.J. Ramirez, “Lattice vibrations of $CuInSe_2$ and $CuGaSe_2$ by Raman microspectrometry”, Journal of Applied Physics 72 (1992) 4321-4324.

4.25. D. Papadimitriou, N. Esser, C. Xue, “Structural properties of chalcopyrite thin films studied by Raman spectroscopy”, Physica Status Solidi B 242 (2005) 2633-2643.

4.26. M. Contreras, L. Mansfield, B. Egaas, J. Li, M. Romero, R. Noufi, “Improved energy conversion efficiency in wide-bandgap Cu(In,Ga)Se_2 solar cells” 37th IEEE Photovoltaic Specialists Conference (PVSC 37),2011.

4.27. N. Mandzy, E. Grulke, T. Druffel, “Breakage of TiO_2 agglomerates in electrostatically stabilized aqueous dispersions”, Powder Technology 160 (2005) 121-126.

4.28. S. Lee, U. Paik, “Dispersant-Ethyl cellulose binder interactions at the Ni particle-dihydroterpineol interface”, Journal of American Ceramic Society 89 (2006) 3050-3055.

4.29. D. Lee, K. Yong, “Non-vacuum deposition of CIGS absorber films for low-cost thin film solar cells”, Korean Journal of Chemical Engineering, 30 (2013) 1347-1358.

4.30. M. Buffiere, A.E. Zaghi, N. Lenaers, M. Batuk, S. Khelifi, J. Drijkoningen, “Effect of binder content in Cu-In-Se precursor ink on the physical and electrical properties of printed $CuInSe_2$ solar cells”, The Journal of Physical Chemistry C,118 (2014) 27201-27209.

4.31. T.P. Hsieh, C.C. Chuang, C.S. Wu, J.C. Chang, J.W. Guo, W.C. Chen, “Effect of residual copper selenide on CIGSe solar cells” Solid State Electronics, 56 (2011) 175-178.

4.32. Y. Liu, D. Kong, H. You, J. Brugger, “Fabrication of Cu(In,Ga)Se_2 thin films from nanoparticles by non-vacuum mechanochemical method and rapid thermal annealing process”, ECS Solid State Letters, 1 (2012) P26-P28.

4.33. R. Kaigawa, K. Ban, S. Mardes, T. Dittrich, R. Klenk, “In and Ga diffusion in Cu(In,Ga)Se_2 and Cu(In,Ga)S_2 films instantaneously prepared in a non-vacuum process”,Energy Procedia 10 (2011) 297-302.

4.34. J.H. Shi, Z.Q. Li, D.W. Zhang, Q.Q. Liu, A. Sun, S.M. Huang, “Fabrication of Cu(In,Ga)Se_2 thin films by sputtering from a single quaternary chalcogenide target”, Progress in Photovoltaics : Research and Applications, 19 (2011) 160-164.

4.35. G. Morell, R.S. Katiyar, S.Z. Weisz, T. Walter, H.W. Schock, I. Balberg, “Crystalline phases at the p to n- type transition in Cu-ternary semiconducting films”, Applied physics letters 69 (1996) 987-989.

4.36. S. Ahn, K.H. Kim, K.H. Yoon, “Cu(In,Ga)Se_2 thin film solar cells from nanoparticle precursors”, Current Applied Physics 8 (2008) 766-769.

4.37. C.P. Liu, C.L. Chuang, “Fabrication of CIGS nanoparticle-ink using ball milling technology for applied in CIGS thin films solar cell”, Powder Technology 229 (2012)78-83.

4.38. B. Vidhya, “Preparation and characterization of nanostructured $CuInGaSe_2$ and CdZnS thin films for photovoltaic applications” Dissertation, CINVESTAV (2010).

4.39. Y.H. Jo, B.C. Mohanty, Y.S. Cho, “Enhanced electrical properties of pulsed laser-deposited $CuIn_{0.7}Ga_{0.3}Se_2$ thin films via processing control”, Solar Energy 84 (2010) 2213-2218.

4.40. P.K. Mishra, V. Dave, R. Chandra, J.N. Prasad, A.K. Choudhary, “Effect of processing parameter on structural, optical and electrical properties of photovoltaic chalcogenide nanostructured RF magnetron sputtered thin absorbing films”, Material Science in Semiconductor Processing 25 (2014) 307-319.

4.41. D.Bhattacharya, S. Chaudhuri, A.K. Pal, “Electrical conduction at low temperatures in polycrystalline CdTe and ZnTe films”, Materials Chemistry and Physics 40 (1995) 44-49.

4.42. R. Noufi, R. Axton, C. Herrington, S.K. Deb, Electronic properties versus composition of thin films of $CuInSe_2$, Applied Physics letters 45 (1984) 668-670.

4.43. A.G. Kannan, T.E. Manjulavalli, J. Chandrasekaran, “Influence of solvent on the properties of CZTS nanoparticle”, Procedia Engineering 141 (2016) 15-22.

4.44. X. Zhang, G. Guo, C. Ji, K. Huang, C. Zha, Y. Wang, L. Shen, A. Gupta, N. Bao, “Efficient thermolysis route monodisperse Cu_2ZnSnS_4 nanocrystals with controlled shape and structure”, Scientific Reports 28 (2014) 1-8.

CHAPTER - 5

PREPARATION OF $Cu(In,Ga)Se_2$ FILM USING MECHANOCHEMICALLY SYNTHESIZED $Cu(In,Ga)Se_y$ POWDER

We have seen in chapter 4 that $Cu(In_{0.7},Ga_{0.3})Se_2$ film deposited using $Cu(In_{0.7},Ga_{0.3})Se_2$ particles do not show grain growth even after annealing at 550 ˚C. In this chapter, we study the influence of Se content in the mechanochemically synthesized $Cu(In_{0.7},Ga_{0.3})Se_y$ powder on recrystallization and grain growth upon selenization of $Cu(In_{0.7},Ga_{0.3})Se_y$ films. Here, we present the change in structural, morphological and compositional properties of $Cu(In_{0.7},Ga_{0.3})Se_y$ powder with respect to Se content and its reflectance on the structural, morphological and compositional properties of selenized films. Also, with respect to optimum Se content in the mechanochemically synthesized powder, Cu content has been varied and its influence on the properties of selenized films are explained.

5.1. Mechanochemical synthesis of $Cu(In_{0.7},Ga_{0.3})Se_y$ powder

$Cu(In_{0.7},Ga_{0.3})Se_y$ particles with y =2,1.5,1 and 0.5 are mechanochemically synthesized using BPR of 25:1, milling speed of 400 rpm and milling time of 2 h and XRD pattern of $Cu(In_{0.7},Ga_{0.3})Se_y$ powders are shown in figure 5.1. It demonstrates that $Cu(In_{0.7},Ga_{0.3})Se_2$ powder consists only of single chalcopyrite phases of CIGSe. Intensity of peaks related to (112), (220)/(204) and (312)/(116) planes of $Cu(In_{0.7},Ga_{0.3})Se_2$ decrease with decreasing Se content. Also, decreasing Se content leads to the formation of binary phases. $Cu(In_{0.7},Ga_{0.3})Se_{1.5}$ powder contains peak corresponding to In_6Se_7. Further reduction of Se content to $Cu(In_{0.7},Ga_{0.3})Se_1$ leads to the formation of binary compound $Cu_{16}In_9$ in addition to In_6Se_7 phase. While, $Cu(In_{0.7},Ga_{0.3})Se_{0.5}$ powder consists of binary phases such as In_4Se_3, $Cu_{11}In_9$, Cu_2Se and $Cu_{2-x}Se$ besides $Cu_{16}In_9$ and In_6Se_7 phases.

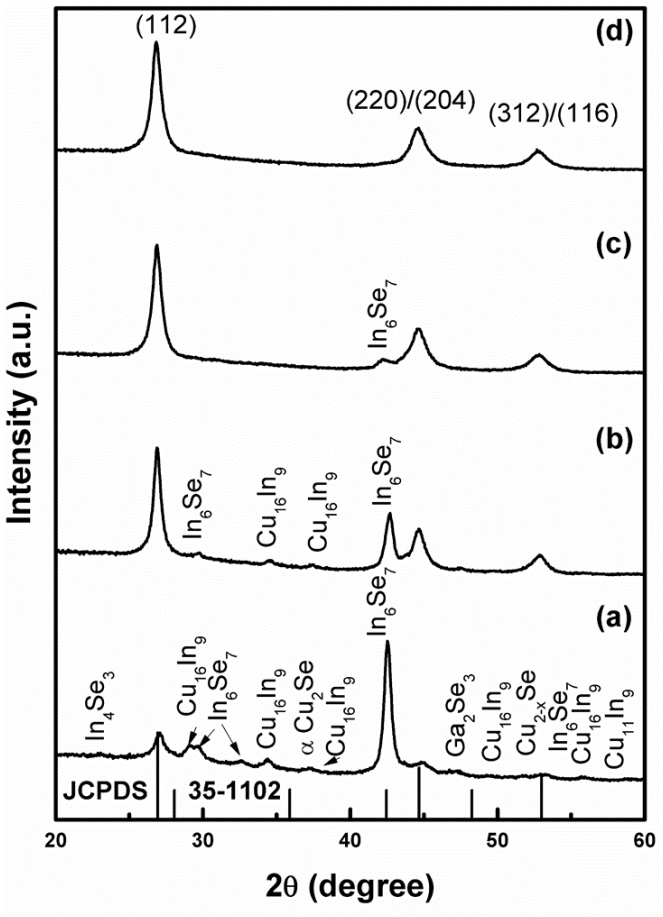

Fig.5.1. X-ray diffraction patterns of mechanochemically synthesized $Cu(In_{0.7},Ga_{0.3})Se_y$ powder: (a) $Cu(In_{0.7},Ga_{0.3})Se_{0.5}$; (b) $Cu(In_{0.7},Ga_{0.3})Se_1$; (c) $Cu(In_{0.7},Ga_{0.3})Se_{1.5}$ and (d) $Cu(In_{0.7},Ga_{0.3})Se_2$.

The phase diagram is a useful tool to explain the binary phase formation with the reduction in Se content. Figure 5.2 represents binary phase diagram of Cu-Se, In-Se, Ga-Se and Cu-In. From figure 5.2, the most probable phases to form with a decrement in Se atomic percentages are $Cu_{2-x}Se$, In_4Se_3, InSe, In_6Se_7, GaSe and Ga_2Se_3. However, the reaction of available Se with Cu, In and Ga to form the above- mentioned compounds depends on their enthalpy of formation. Hence, it is not accurate to assume that the available Se distribute evenly for reaction with Cu, In and Ga. Enthalpy of formation of compounds $Cu_{2-x}Se$, In_4Se_3, InSe, In_6Se_7, GaSe and Ga_2Se_3 are -59.3, -332.24, -117, -688.63, -159.09 and -316 KJ/ mol respectively. [5.1-5.3]. Hence In_6Se_7 is the most probable binary selenide to form first than In_4Se_3 and InSe. Considering GaSe and Ga_2Se_3, Ga_2Se_3 forms before GaSe. Also, In $Cu(In_{0.7},Ga_{0.3})Se_2$, reducing Se content without changing the atomic content of Cu

makes the $Cu(In_{0.7},Ga_{0.3})Se_y$ alloy Copper- rich. Hence a higher amount of Cu is available to react with In and Ga. So, from the Cu-In phase diagram shown in figure 5.2 (d), the most probable phases to form with higher Cu content are $Cu_{11}In_9$ and $Cu_{16}In_9$. Thus, In_4Se_3, $Cu_{11}In_9$, Cu_2Se, $Cu_{2-x}Se$, $Cu_{16}In_9$ and In_6Se_7 phases are observed in the $Cu(In_{0.7},Ga_{0.3})Se_{0.5}$ powder.

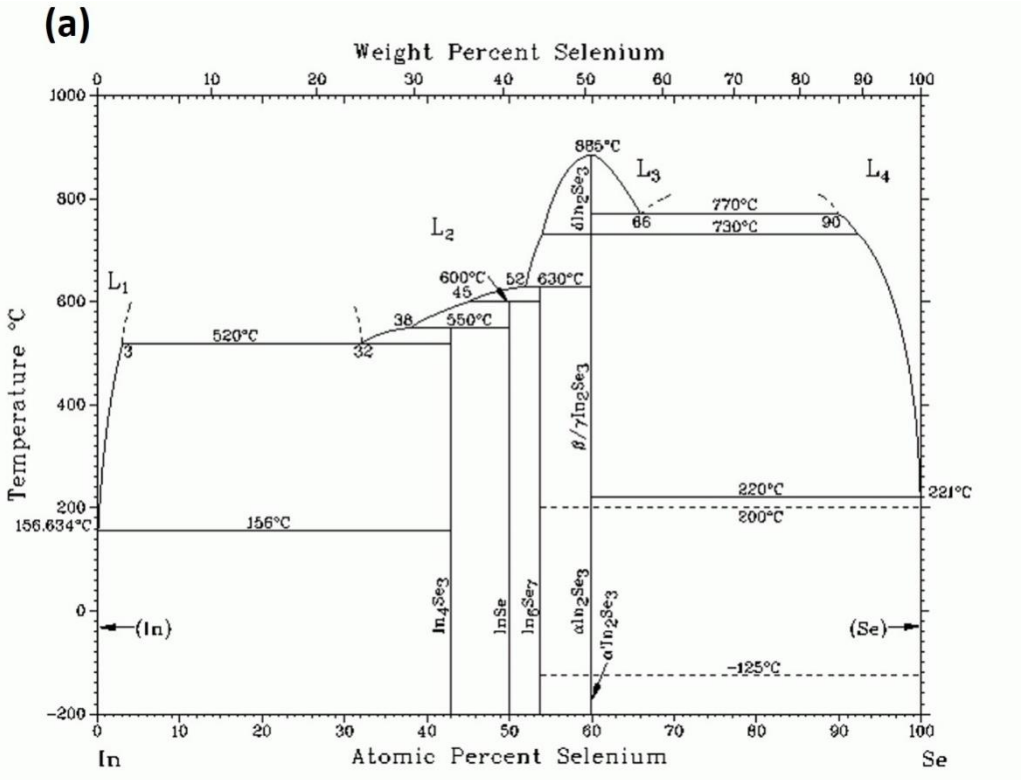

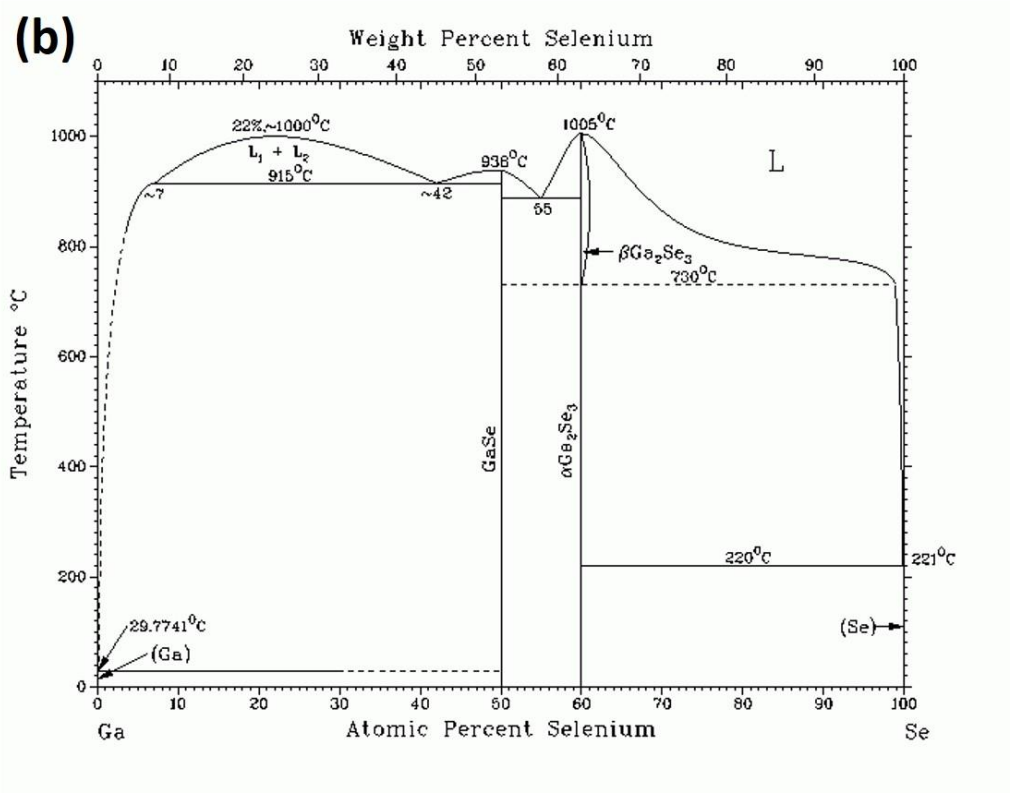
(b)
Weight Percent Selenium
Temperature °C
Atomic Percent Selenium
Ga
Se
22%,~1000°C
L1 + L2
915°C
~7
~42
936°C
1005°C
55
L
βGa2Se3
730°C
GaSe
αGa2Se3
220°C
221°C
29.7741°C
(Ga)
(Se)

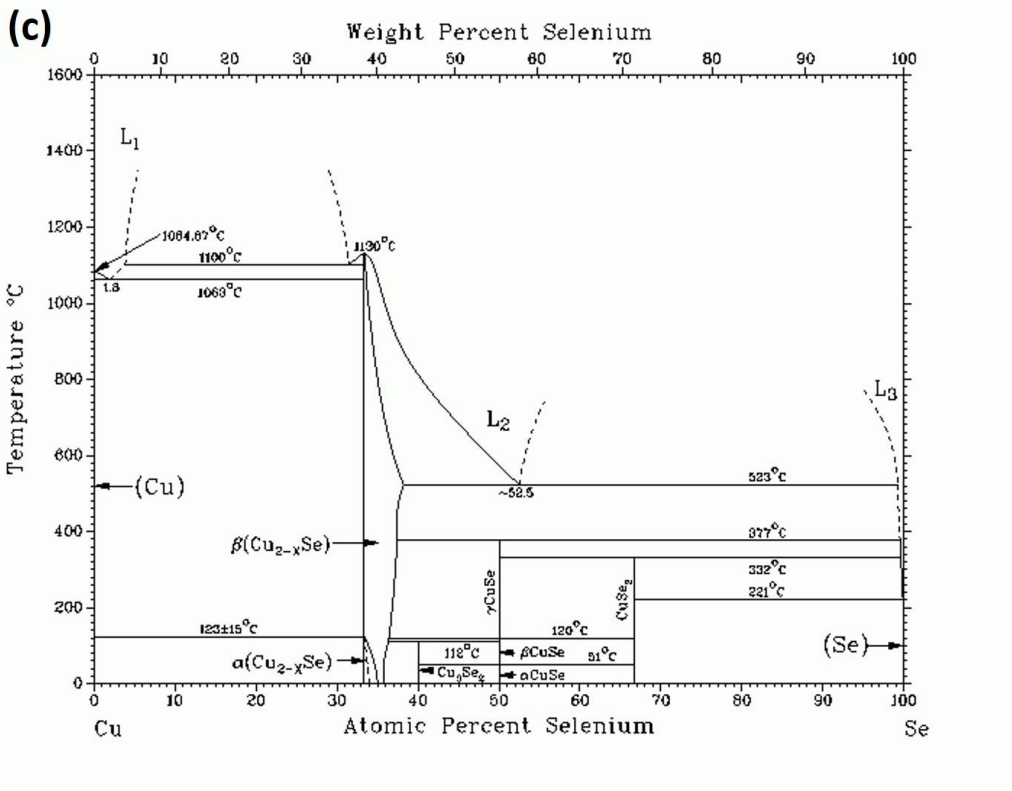
(c)
Weight Percent Selenium
Temperature °C
Atomic Percent Selenium
Cu
Se
L1
1084.87°C
1100°C
1.8
1069°C
1130°C
L2
L3
~52.5
523°C
(Cu)
β(Cu2-xSe)
377°C
γCuSe
CuSe2
332°C
221°C
123±15°C
120°C
118°C
βCuSe
51°C
Cu3Se2
αCuSe
α(Cu2-xSe)
(Se)

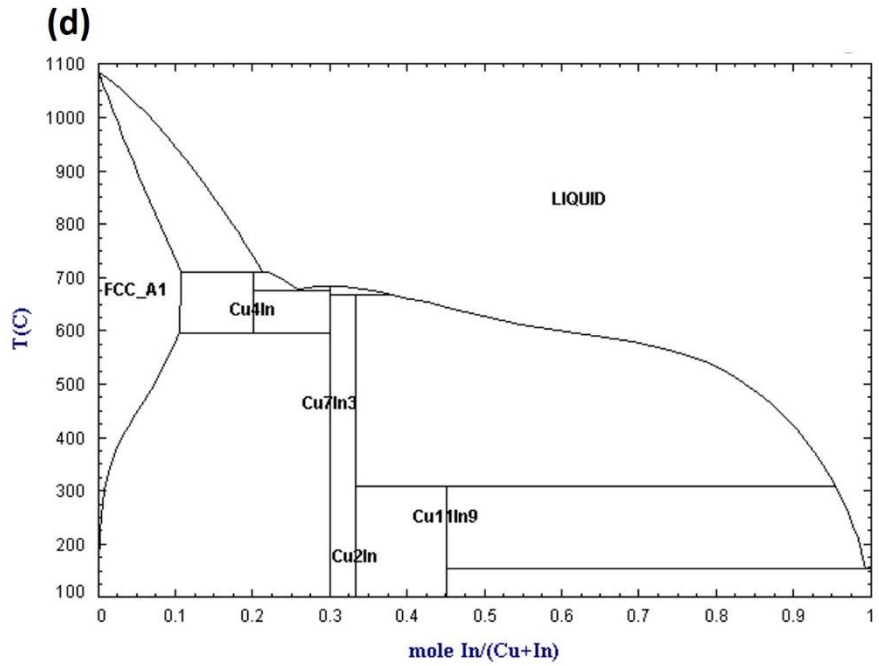

Fig.5.2. Binary phase diagram of (a) In-Se, (b) Ga-Se, (c) Cu-Se and (d) Cu-In systems [5.4-5.7].

Compositional data obtained from EDAX analysis (operating voltage 20 kV) is given in table 5.1. EDAX data shows that with reducing Se content in the ball milling powder mixture, the Cu/Se ratio increases as 0.55, 0.71, 1.1 and 1.6 for $Cu(In_{0.7},Ga_{0.3})Se_2$, $Cu(In_{0.7},Ga_{0.3})Se_{1.5}$, $Cu(In_{0.7},Ga_{0.3})Se_1$ and $Cu(In_{0.7},Ga_{0.3})Se_{0.5}$ respectively. Also, an uneven variation in Cu/(In+Ga) can be noticed with reducing Se content in the powder.

Table 5.1. EDAX compositional analysis for mechanochemically synthesized $Cu(In_{0.7},Ga_{0.3})Se_y$ powders.

Sample	Atomic percentage of elements (at.%)				Cu/ (In+Ga)	Ga/ (In+Ga)	Cu/Se
	Cu	In	Ga	Se			
$Cu(In_{0.7},Ga_{0.3})Se_2$	26.2	16.7	9.2	47.6	1.00	0.35	0.55
$Cu(In_{0.7},Ga_{0.3})Se_{1.5}$	30.3	25.6	8.5	42.4	0.88	0.25	0.71
$Cu(In_{0.7},Ga_{0.3})Se_1$	33.3	27.1	9.3	30.1	0.91	0.25	1.1
$Cu(In_{0.7},Ga_{0.3})Se_{0.5}$	35.7	31.8	11.0	21.8	0.84	0.26	1.6

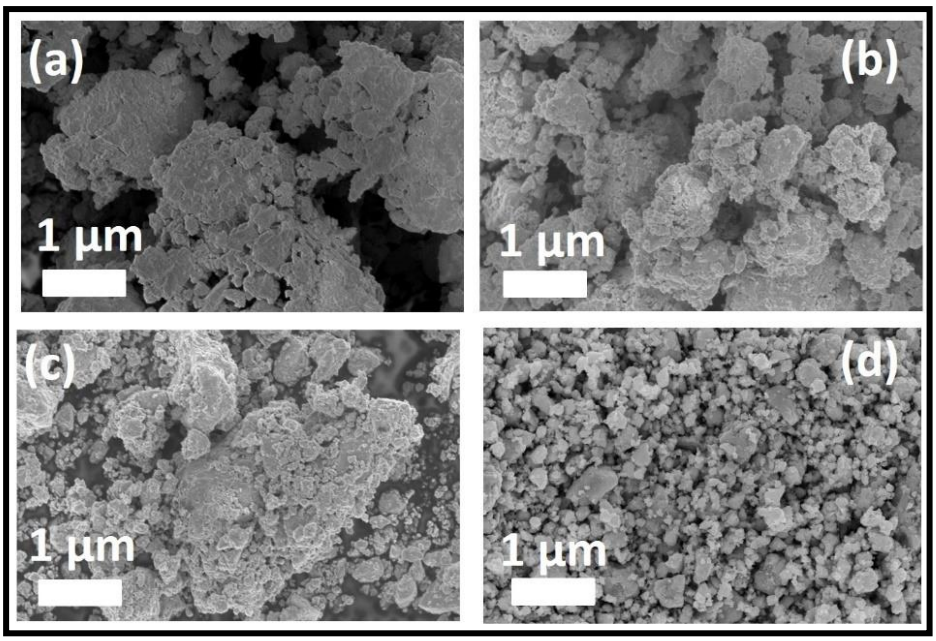

Fig.5.3. FESEM images of mechanochemically synthesized (a) $Cu(In_{0.7},Ga_{0.3})Se_{0.5}$, (b) $Cu(In_{0.7},Ga_{0.3})Se_1$, (c) $Cu(In_{0.7},Ga_{0.3})Se_{1.5,}$ and (d) $Cu(In_{0.7},Ga_{0.3})Se_2$ powder.

Morphology and microstructure of $Cu(In_{0.7},Ga_{0.3})Se_y$ powder with different Se content are shown in figure 5.3. The $Cu(In_{0.7},Ga_{0.3})Se_2$ powder (figure 5.3 (d)) consists of smaller particles with well-refined microstructure and equiaxed morphology. The interfacial boundaries are no longer visible in $Cu(In_{0.7},Ga_{0.3})Se_2$ powder. Upon decreasing Se atomic proportion to 1.5, a mixture of cold welded and fragmented particles is observed (figure 5.3 (c)). A predominance of bigger fragmented structures of flattened -cold welded particles can be seen in $Cu(In_{0.7},Ga_{0.3})Se_1$ powder (figure 5.3 (b)). Subsequent decrease of Se atomic proportion to 0.5, particles formed of welded and flattened laminar structures are observed (figure 5.3 (a)). Also, interfacial boundaries are visible in $Cu(In_{0.7},Ga_{0.3})Se_{0.5}$ and $Cu(In_{0.7},Ga_{0.3})Se_1$ powder. This observed change in morphology elucidates the importance of properties of precursor material on the milling process. As discussed in section 4.1.1, mechanochemical synthesis of $Cu(In_{0.7},Ga_{0.3})Se_2$ using elemental Cu, In, Ga and Se is coming under alloying of ductile-brittle system. Copper, Indium and Gallium are ductile elements whereas Se is brittle. Figure 5.4 shows the process involved in mechanical alloying of a ductile-brittle system schematized by Fogagnolo and Aikin [5.8]. According to that, at the first stage of milling, ductile particles undergo deformation while brittle particle undergoes fragmentation. During deformation process, ductile particle flattens. When

the ductile particle starts to weld during ball–particle-ball collision, fragments of brittle particle come between two or more ductile particles. The phenomena of deformation and welding, harden the material and accelerate fracture process. This leads to equiaxed morphology. At an equilibrium condition of welding and fracturing process, the alloy particle form with randomly oriented interfacial boundaries. Upon continuous milling, the alloy particle undergoes a refinement such that interfacial boundaries are no longer visible as in the SEM image of $Cu(In_{0.7},Ga_{0.3})Se_2$ powder. Upon decreasing Se content in the precursor material, the brittle content in the system decreases and the mechanism of alloying process turns out to be more as a ductile-ductile system.

Alloying of a ductile-ductile system is explained as follows: the first stage of particle deformation is followed by the welding stage in which particles took lamellar form. Subsequently, the welded particle became more equiaxed with an oriented morphology and later with random welding, particle took a random arrangement of several lamellar granules within a given particle (figure 5.5) [5.9]. Hence random arrangement of several lamellar granules can be observed within an agglomerated grain in the $Cu(In_{0.7},Ga_{0.3})Se_{0.5}$ powder.

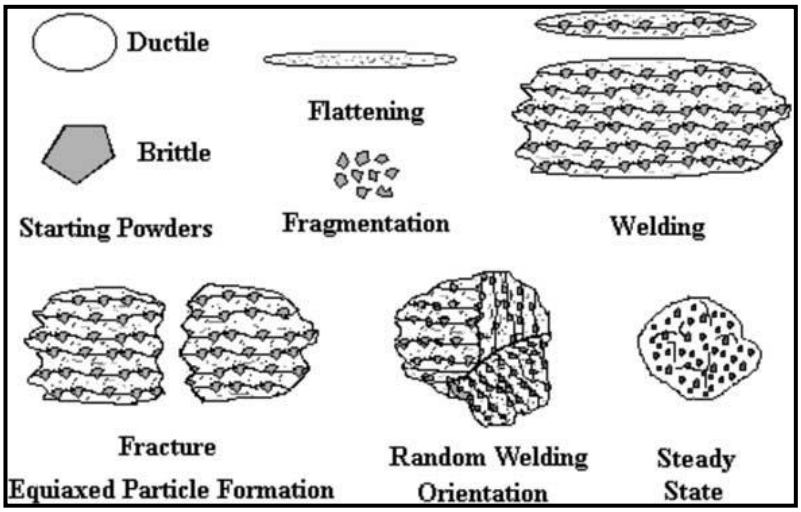

Fig. 5.4. Schematic of mechanochemical alloying of ductile-brittile system [5.8].

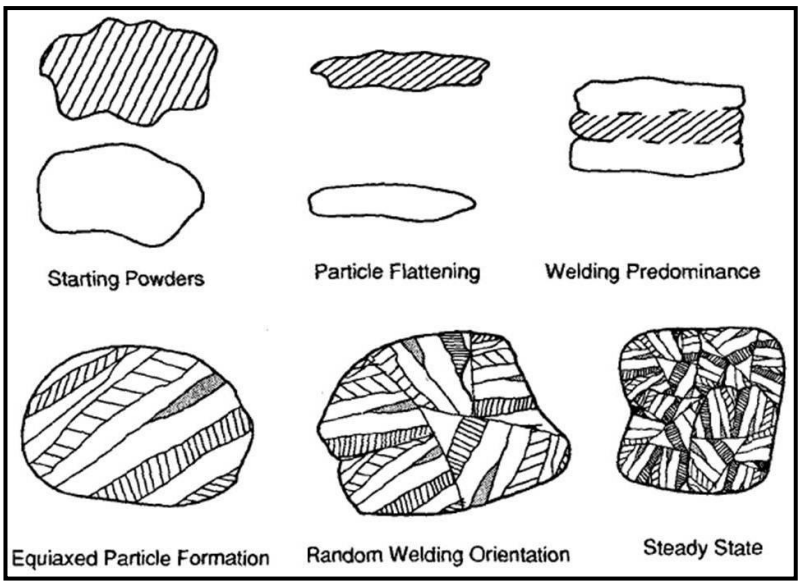

Fig.5.5. Schematic of mechanochemical alloying of ductile-ductile system [5.9].

Further, $Cu(In_{0.7},Ga_{0.3})Se_y$ particle-based ink is formulated as described in section 3.2 and $Cu(In_{0.7},Ga_{0.3})Se_y$ films are deposited on glass substrate by doctor blade method as described in section 3.3.3. The $Cu(In_{0.7},Ga_{0.3})Se_y$ films are annealed at 300 ˚C for 1 h in air to remove Carbon and then selenized at 550 ˚C as described in section 3.4. Properties of selenized films are explained in the following section.

5.2. Selenization of $Cu(In_{0.7},Ga_{0.3})Se_y$ Films

XRD pattern of $Cu(In_{0.7},Ga_{0.3})Se_2$ films obtained after selenization of films (a) $Cu(In_{0.7},Ga_{0.3})Se_{0.5}$, (b) $Cu(In_{0.7},Ga_{0.3})Se_1$, (c) $Cu(In_{0.7},Ga_{0.3})Se_{1.5}$ and (d) $Cu(In_{0.7},Ga_{0.3})Se_2$ are shown in figure 5.6. It exhibits the fact that, regardless of Se content in the initial $Cu(In_{0.7},Ga_{0.3})Se_y$ precursor, all films exhibit (112), (220)/(204), (312)/(116) planes of chalcopyrite phase of $Cu(In_{0.7},Ga_{0.3})Se_2$. In addition to these three characteristic peaks, selenized films show (103), (211) and (213)/(105) planes of chalcopyrite phase of $Cu(In_{0.7},Ga_{0.3})Se_2$. However, a peak appears at 2θ=30.01˚in the films (a), (b) and (c) is assigned to $Cu_{2-x}Se$ phase (JCPDS # 06-0680).

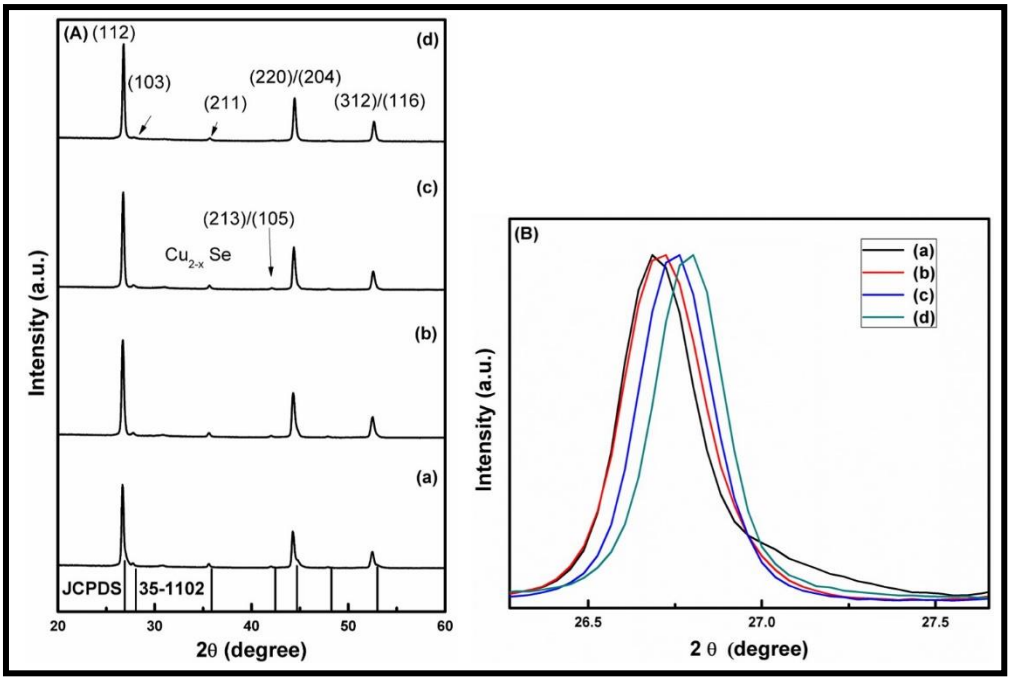

Fig.5.6. (A) XRD pattern of $Cu(In_{0.7},Ga_{0.3})Se_2$ films obtained after selenization of films (a) $Cu(In_{0.7},Ga_{0.3})Se_{0.5}$, (b) $Cu(In_{0.7},Ga_{0.3})Se_1$, (c) $Cu(In_{0.7},Ga_{0.3})Se_{1.5}$ and (d) $Cu(In_{0.7},Ga_{0.3})Se_2$ and (B) A Zoom- in look of (112) peaks from figure 5.6.(A).

it is found from figure 5.6 (B) that, as the Se content in the precursor film decreases, the peak position in the selenized films shift to lower 2θ values. Also, asymmetry in the peak shape increases. A gradient in Ga/(In+Ga) over the depth of film in the case of films obtained by selenization of metallic precursors has reported previously [5.10-5.12]. In our experiments, reducing Se content turns the $Cu(In_{0.7},Ga_{0.3})Se_y$ alloy metallic. Hence selenization of $Cu(In_{0.7},Ga_{0.3})Se_y$ film with lesser Se content could be considered similar to the selenization of metallic precursors. Metallic nature of precursor increases with decreasing Se content. Hence the observed increase in asymmetry of the peak shape could be due to increasing variation in the Ga/(In+Ga) throughout the film. Kaigawa et.al [5.13] has reported split in (112) peak as an indication of higher Ga content at the back and the front surface of the film with minimum Ga in the centre, and an asymmetry in peak shape without peak splitting as an indication of monotonous decrease in Ga content. Hence we could assume that Ga gradient in these samples varies monotonously. FWHM of XRD peak is calculated to be 0.24,0.24,0.24 and 0.19 for CIGSe films obtained from selenization of $Cu(In_{0.7},Ga_{0.3})Se_2$, $Cu(In_{0.7},Ga_{0.3})Se_{1.5}$, $Cu(In_{0.7},Ga_{0.3})Se_1$ and $Cu(In_{0.7},Ga_{0.3})Se_{0.5}$ films respectively. The reduction in FWHM of XRD peak indicates improved

crystallinity and or grain growth [5.15]. FESEM images given in figure 5.8 exhibits traces of recrystallization starting from $Cu(In_{0.7},Ga_{0.3})Se_2$ films obtained from $Cu(In_{0.7},Ga_{0.3})Se_{1.5}$ films. Grain growth can be observed from $Cu(In_{0.7},Ga_{0.3})Se_2$ films obtained from selenization of $Cu(In_{0.7},Ga_{0.3})Se_1$ films. Even though these two films do not show change in FWHM with respect to CIGSe films obtained from $Cu(In_{0.7},Ga_{0.3})Se_2$ film. It can be due to the inaccuracy in the FWHM value arises from asymmetric shape of the peak.

Raman spectra of $Cu(In_{0.7},Ga_{0.3})Se_2$ films obtained after selenization of films with different Se content, (a) $Cu(In_{0.7},Ga_{0.3})Se_{0.5}$, (b) $Cu(In_{0.7},Ga_{0.3})Se_1$, (c) $Cu(In_{0.7},Ga_{0.3})Se_{1.5}$ and (d) $Cu(In_{0.7},Ga_{0.3})Se_2$ is presented in figure 5.7. Only A1 vibrational mode of $Cu(In_{0.7},Ga_{0.3})Se_2$ is present in figure 5.7 (d). While a small intense peak corresponding to $Cu_{2-x}Se$ appears in figure 5.7 (c). The intensity of peak related to $Cu_{2-x}Se$ is found to be increasing gradually in figure 5.7 (b) and (a). FWHM of A1 vibrational mode is a demonstration of the crystalline quality of chalcopyrite phase. Smaller FWHM signs better crystalline quality [5.15]. FWHM of A1 mode for $Cu(In_{0.7},Ga_{0.3})Se_2$ films obtained after selenization of films with different Se content (a) $Cu(In_{0.7},Ga_{0.3})Se_{0.5}$, (b) $Cu(In_{0.7},Ga_{0.3})Se_1$, (c) $Cu(In_{0.7},Ga_{0.3})Se_{1.5}$ and (d) $Cu(In_{0.7},Ga_{0.3})Se_2$ is calculated to be 11.63, 9.88, 6.19 and 4.94 respectively. This decrement in FWHM indicates improvement in crystalline quality of $Cu(In_{0.7},Ga_{0.3})Se_2$ films. It also underlines that the crystalline quality of $Cu(In_{0.7},Ga_{0.3})Se_2$ film obtained by mechanochemically synthesized powder can be improved by using $Cu(In_{0.7},Ga_{0.3})Se_{0.5}$ as precursor powder. The intensity of peak related to $Cu_{2-x}Se$ is found to be increasing gradually in figure 5.7 (c), (b) and (a). Moreover, a shift in position of A1 mode vibrational peak to higher wavenumber is observed from figure 5.7 (d) to (a). This can be related to increase in Cu/(In+Ga), which is evident from the EDAX analysis given in table 5.2 [5.14].

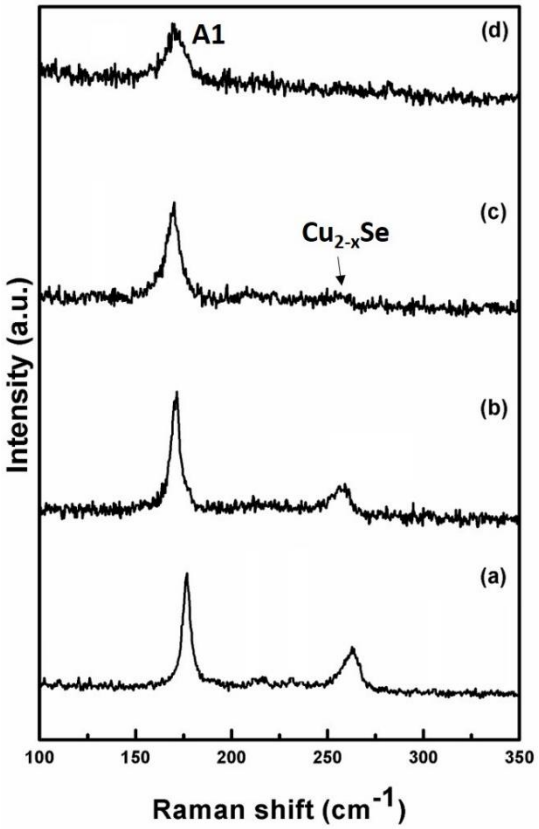

Fig.5.7. Raman spectra of $Cu(In_{0.7},Ga_{0.3})Se_2$ films obtained after selenization of films; (a) $Cu(In_{0.7},Ga_{0.3})Se_{0.5}$, (b) $Cu(In_{0.7},Ga_{0.3})Se_1$, (c) $Cu(In_{0.7},Ga_{0.3})Se_{1.5}$ and (d) $Cu(In_{0.7},Ga_{0.3})Se_2$.

EDAX data obtained from area analysis of selenized films at operating voltage of 20 kV is given in table 5.2. An increase in Se content subsequent to selenization of films can be easily seen from table 5.2. However, the increment in Se content in $Cu(In_{0.7},Ga_{0.3})Se_{1.5}$ was minimal. It could be due to change in reactivity of precursor material with Se content. It is assumed that reactivity of $Cu(In_{0.7},Ga_{0.3})Se_{1.5}$ during selenization is less compared to the metallic precursor material in $Cu(In_{0.7},Ga_{0.3})Se_1$ and $Cu(In_{0.7},Ga_{0.3})Se_{0.5}$. The Cu/(In+Ga) in selenized $Cu(In_{0.7},Ga_{0.3})Se_{1.5}$, $Cu(In_{0.7},Ga_{0.3})Se_1$ and $Cu(In_{0.7},Ga_{0.3})Se_{0.5}$ films are close to and greater than 1 making the samples Cu- rich. It is reported that Cu-Se binary phases will appear in the sample with Cu/(In+Ga) greater than 1. The small peak corresponding to $Cu_{2-x}Se$ phase appeared in XRD pattern and Raman spectra of $Cu(In_{0.7},Ga_{0.3})Se_2$ films obtained by selenization of $Cu(In_{0.7},Ga_{0.3})Se_{1.5}$, $Cu(In_{0.7},Ga_{0.3})Se_1$ and $Cu(In_{0.7},Ga_{0.3})Se_{0.5}$ films is due to Cu-rich composition. The Ga/(In+Ga) in all the samples shows that there is no loss of Ga and In from the samples during selenization. Hence, the shift in XRD peak

position to lower 2θ values along with asymmetry in the peak shape observed in the selenized samples is confirmed to be due to the development of Ga gradient in the sample [5.13].

Table 5.2. EDAX data from area analysis of $Cu(In_{0.7},Ga_{0.3})Se_2$ films obtained after selenization of $Cu(In_{0.7},Ga_{0.3})Se_y$ films.

$Cu(In_{0.7},Ga_{0.3})Se_2$ films obtained from	**Atomic percentage of elements (at. %)**				**Cu/ (In+Ga)**	**Ga/ (In+Ga)**	**Cu/Se**
	Cu	**In**	**Ga**	**Se**			
$Cu(In_{0.7},Ga_{0.3})Se_2$	24.40	17.82	8.35	49.43	0.93	0.32	0.49
$Cu(In_{0.7},Ga_{0.3})Se_{1.5}$	29.41	22.45	7.68	40.46	0.97	0.25	0.73
$Cu(In_{0.7},Ga_{0.3})Se_1$	28.36	16.56	8.80	46.27	1.12	0.35	0.61
$Cu(In_{0.7},Ga_{0.3})Se_{0.5}$	29.40	17.24	6.68	46.69	1.22	0.28	0.63

FESEM images of $Cu(In_{0.7},Ga_{0.3})Se_2$ films obtained by selenization of $Cu(In_{0.7},Ga_{0.3})Se_y$ precursor materials are given in figure 5.8. It shows that microstructure of the selenized film is strongly dependent on the initial Se content in the precursor material and associated homogeneity of the precursor $Cu(In_{0.7},Ga_{0.3})Se_y$ alloy powder. $Cu(In_{0.7},Ga_{0.3})Se_2$ precursor film does not show recrystallization and grain growth during selenization (figure 5.8 (d)). However, a tendency of recrystallization can be seen from selenized $Cu(In_{0.7},Ga_{0.3})Se_{1.5}$ precursor film (figure 5.8 (c)). Nevertheless, $Cu(In_{0.7},Ga_{0.3})Se_1$ precursor film showed clear recrystallization and grain growth during selenization (figure 5.8 (b)). However, $Cu(In_{0.7},Ga_{0.3})Se_{0.5}$ precursor film is found as most prone to recrystallization and grain growth during selenization (figure 5.8 (a)). The increase in grain growth observed in $Cu(In_{0.7},Ga_{0.3})Se_2$ films with reducing Se content in the precursor can be seen more vividly from the cross-sectional images given in figure 5.8. However, it should be noted that the occurred grain growth is in a non-uniform fashion such that it leads to the presence of bigger grains along with smaller grains in the selenized films.

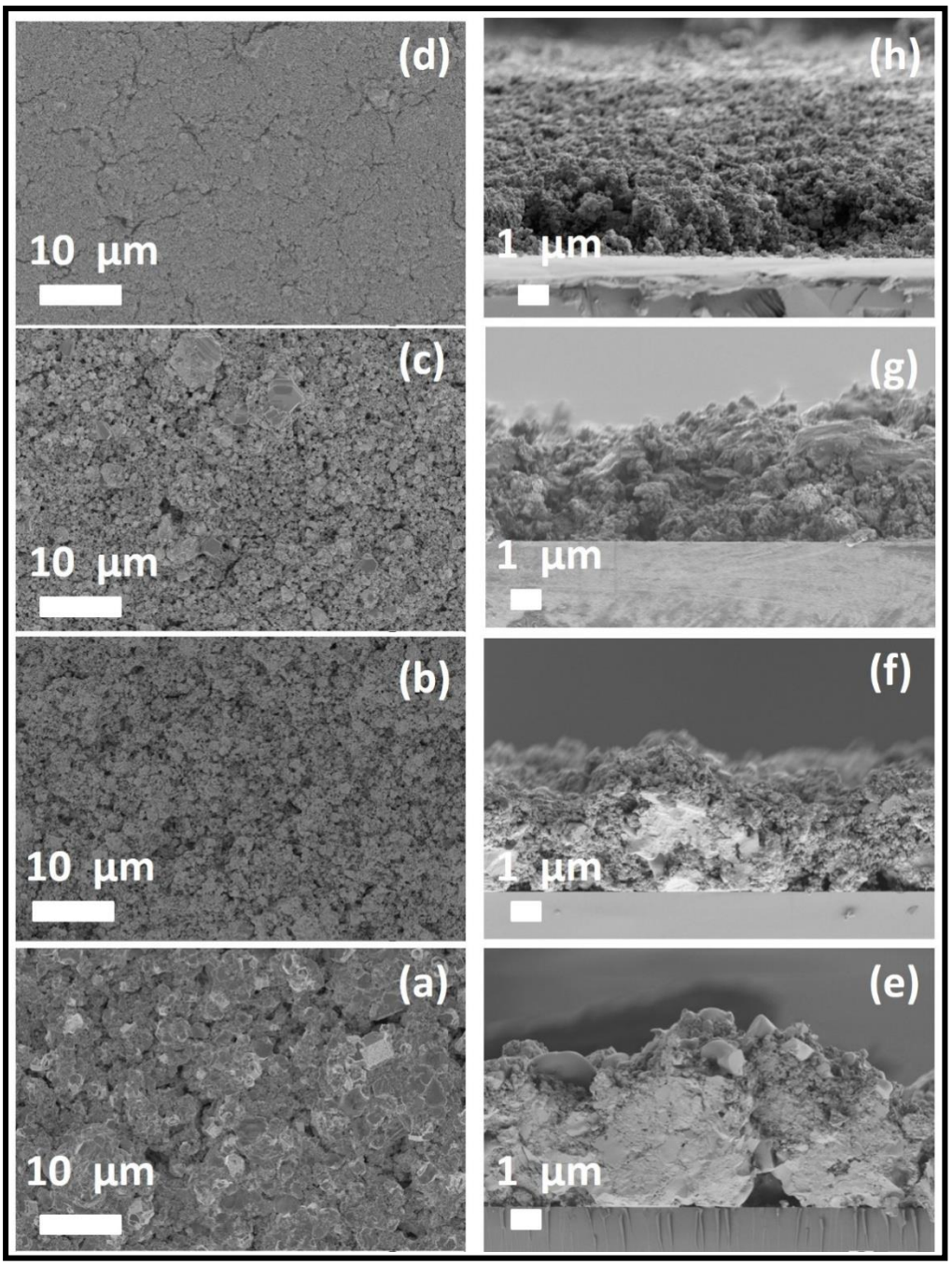

Fig.5.8. Planar (left) and cross- sectional (right) FESEM images of $Cu(In_{0.7},Ga_{0.3})Se_2$ films obtained after selenization of films with different Se content; (a and e) $Cu(In_{0.7},Ga_{0.3})Se_{0.5}$, (b and f) $Cu(In_{0.7},Ga_{0.3})Se_1$, (c and g) $Cu(In_{0.7},Ga_{0.3})Se_{1.5}$ and (d and h) $Cu(In_{0.7},Ga_{0.3})Se_2$.

Zhaghi et. al [5.16] explained the observed grain growth in CISe system with reducing Se content as “CuSe liquid phase assisted process”. A eutectic phase at 52 at % of Se with a melting point of 523 ˚C can be identified in the Cu-Se binary phase diagram (figure 5.2 (c)). From that it could be deduced that CuSe acting as a fluxing agent for

the grain growth of $Cu(In_{0.7},Ga_{0.3})Se_2$ at a temperature near and above the melting point of the binary. The CuSe phase initiates liquid phase sintering and densification through particle rearrangement due to capillary forces and fast grain growth due to solution-reprecipitation [5.16-5.18]. It is thought that amount of intermediate CuSe formed during selenization increases with decreasing Se content in the precursor film. It is considered as the reason for enhanced grain growth observed in $Cu(In_{0.7},Ga_{0.3})Se_{0.5}$ precursor film during selenization [5.16].

5.2.1. Influence of Copper Content

However, $Cu(In_{0.7},Ga_{0.3})Se_2$ film obtained from $Cu(In_{0.7},Ga_{0.3})Se_{0.5}$ powder consists of $Cu_{2-x}Se$ phase which is evident from XRD and Raman analysis as shown in figure 5.6 and 5.7. $Cu_{2-x}Se$ phases present $Cu(In_{0.7},Ga_{0.3})Se_2$ film can be removed using KCN etching [5.19]. But, great care and security measures must be assured before using KCN as it is highly poisonous. From the phase diagram shown in Chapter 2, figure 2.3, co-existence of $Cu_{2-x}Se$ phase results from the Cu-rich composition of $Cu(In_{0.7},Ga_{0.3})Se_2$. Hence, the $Cu_{2-x}Se$ formation and thereby KCN etching can be avoided by aiming to the formation of Cu-poor $Cu(In_{0.7},Ga_{0.3})Se_2$. Thereupon $Cu(In_{0.7},Ga_{0.3})Se_2$ powder with composition $Cu_{0.85}(In_{0.7},Ga_{0.3})Se_{0.5}$ has been synthesized and deposited film has been heat treated at 300 ˚C for 1 h in air and selenized. The figure 5.9 shows comparison of XRD pattern of CIGSe films obtained from selenization of $Cu(In_{0.7},Ga_{0.3})Se_{0.5}$ and $Cu_{0.85}(In_{0.7},Ga_{0.3})Se_{0.5}$ powder.

It can clearly notice that upon reducing Cu content in the initial $Cu(In_{0.7},Ga_{0.3})Se_{0.5}$ powder from 1 to 0.85, the peak at 30.8˚ related to $Cu_{2-x}Se$ appeared in figure 5.9 (a) is not observed in figure 5.9 (b). Moreover, the position of all the peaks has shifted slightly to higher 2θ values with reducing atomic proportion of Cu from 1 to 0.85. FWHM of (112) peaks is 0.19 and 0.229 respectively for CIGSe films obtained by selenization of $Cu(In_{0.7},Ga_{0.3})Se_{0.5}$ and $Cu_{0.85}(In_{0.7},Ga_{0.3})Se_{0.5}$ films. It indicates smaller grain size for CIGSe films obtained by selenization of $Cu_{0.85}(In_{0.7},Ga_{0.3})Se_{0.5}$ films which are in good agreement with the FESEM images given in figure 5.11.

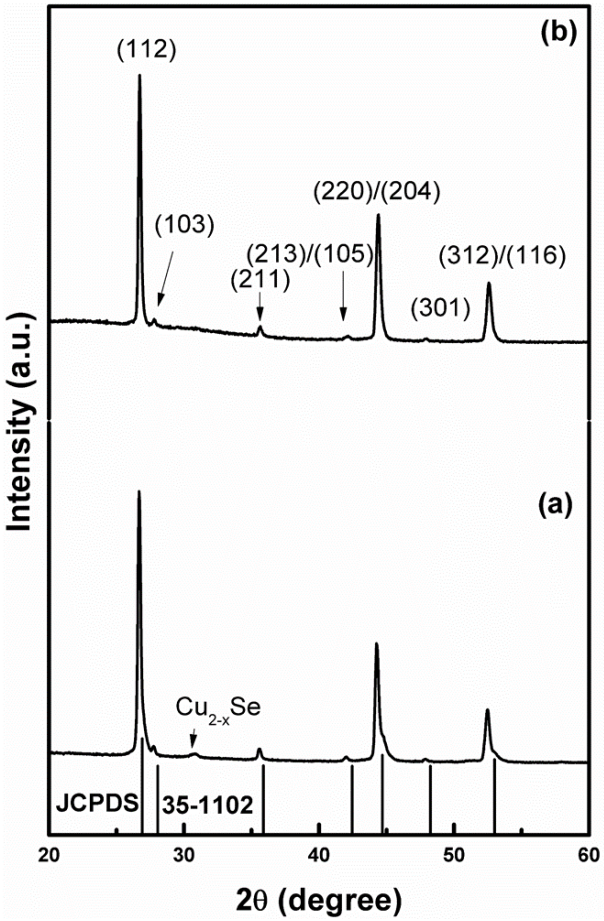

Fig.5.9. XRD pattern of CIGSe films obtained by selenization of (a) $CuIn_{0.7}Ga_{0.3}Se_{0.5}$ and (b) $Cu_{0.85}In_{0.7}Ga_{0.3}Se_{0.5}$ films.

Figure 5.10 shows Raman spectra of CIGSe films obtained from (a) $Cu(In_{0.7},Ga_{0.3})Se_{0.5}$ and (b) $Cu_{0.85}(In_{0.7},Ga_{0.3})Se_{0.5}$ precursor films. Figure 5.10 (a) shows two peaks, one at 176 cm^{-1} corresponding to A1 mode of $Cu(In_{0.7},Ga_{0.3})Se_2$ and other at 262 cm^{-1} indicating presence of $Cu_{2-x}Se$ phase. Figure 5.10 (b) shows a single peak around 172 cm^{-1} with FWHM of 5.52 which is slightly broader than A1 mode (FWHM=4.94) observed in figure 5.10(a). The shift in A1 mode vibration to lower wavenumber with decreasing Cu content is reported by Xu et.al [5.20, 5.21]. It is since as Cu content decreases, Copper vacancies (V_{cu}) increases and V_{cu} causes to relax the Se-cation bond stretching forces which induce redshift to the A1 phonon frequencies.

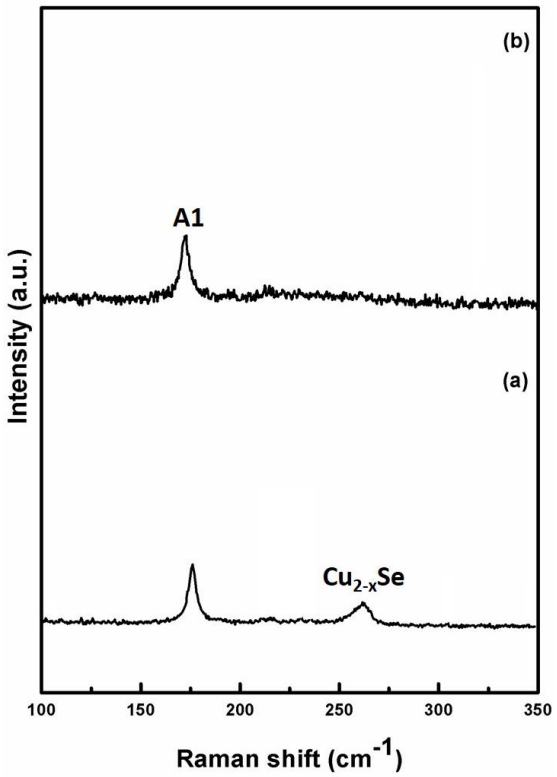

Fig.5.10. Raman spectra of CIGSe films obtained after selenization of (a) $Cu(In_{0.7},Ga_{0.3})Se_{0.5}$, and (b) $Cu_{0.85}(In_{0.7},Ga_{0.3})Se_{0.5}$ films.

Planar FESEM images of films with different Cu content are shown in figure 5.11. CIGSe films obtained by selenization of $Cu(In_{0.7},Ga_{0.3})Se_{0.5}$, and $Cu_{0.85}(In_{0.7},Ga_{0.3})Se_{0.5}$ films showed grain growth and recrystallization. Nevertheless, both films exhibit different surface morphology. The identified Cauliflower-shaped structure on the surface of CIGSe film (figure 5.11 (a)) is a $Cu_{2-X}Se$ phase, whereas they are absent in the Cu- poor CIGSe ($Cu_{0.85}(In0.7,Ga_{0.3})Se_2$) film (figure 5.11 (b)). Moreover, the surface of CIGSe film contains pores which are less in the Cu-poor film. The cross-sectional image exhibits well crystallised and dense film. It is important to note here that the pores observed on the surface of the film are not extended into the bulk (figure 5.11 (c)). While Cu-poor CIGSe film exhibits big and small grains. It indicates the role of Cu-Se in densification of CIGSe film. The film with Cu/(In+Ga)~ 0.85 has less Cu content so that less amount of CuSe is available to assist densification process during selenization.

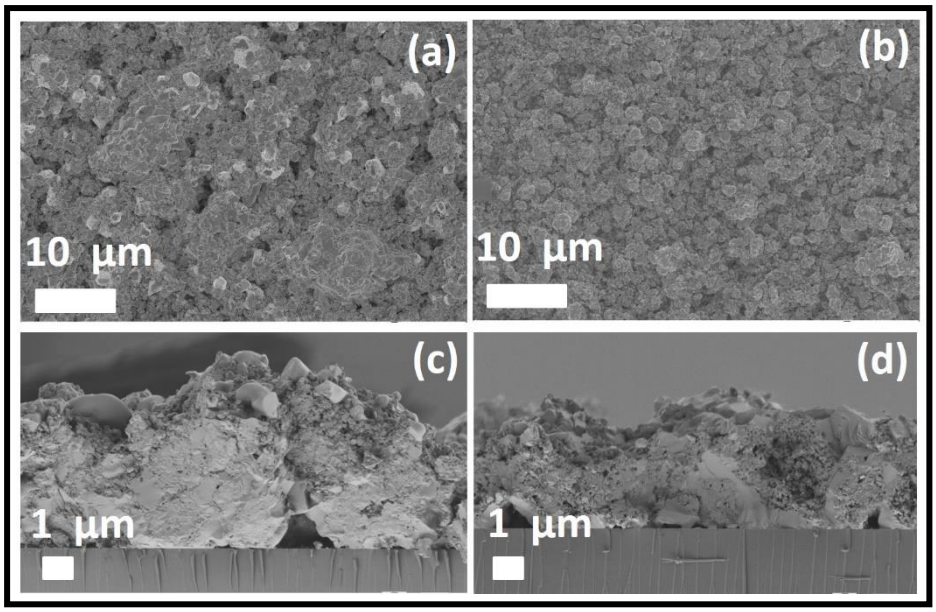

Fig.5.11. Planar (top) and cross- sectional (bottom) FESEM images of CIGSe films obtained after selenization of (a and c) $Cu(In_{0.7},Ga_{0.3})Se_{0.5}$ and (b and d) $Cu_{0.85}(In_{0.7},Ga_{0.3})Se_{0.5}$ films.

EDAX composition analysis of CIGSe films obtained after selenization of $Cu(In_{0.7},Ga_{0.3})Se_{0.5}$ and $Cu_{0.85}(In_{0.7},Ga_{0.3})Se_{0.5}$ films are given in table 5.3. EDAX analysis confirms that composition of Cu, In, Ga and Se in Copper-poor CIGSe film is in match to the targeted composition i.e $Cu_{0.85}(In_{0.7},Ga_{0.3})Se_2$.

Table 5.3. EDAX data of area analysis of CIGSe films obtained after selenization of $Cu(In_{0.7},Ga_{0.3})Se_{0.5}$ and $Cu_{0.85}(In_{0.7},Ga_{0.3})Se_{0.5}$ films.

CIGSe film obtained by selenization of	Atomic percentage of elements (at.%)				Cu/ (In+Ga)	Ga/ (In+Ga)	Cu/Se
	Cu	In	Ga	Se			
$Cu(In_{0.7},Ga_{0.3})Se_{0.5}$	29.40	17.24	6.68	46.69	1.22	0.28	0.63
$Cu_{0.85}(In_{0.7},Ga_{0.3})Se_{0.5}$	22.92	17.51	9.13	50.44	0.86	0.34	0.45

5.2.1.1 The electrical properties of $Cu(In_{0.7},Ga_{0.3})Se_{0.5}$ and $Cu_{0.85}(In_{0.7},Ga_{0.3})Se_{0.5}$ – based CIGSe films

The electrical properties of CIGSe films obtained by selenization of $Cu(In_{0.7},Ga_{0.3})Se_{0.5}$ and $Cu_{0.85}(In_{0.7},Ga_{0.3})Se_{0.5}$ films are investigated by Hall effect measurement. The carrier type, carrier concentration (p), mobility (μ) and resistivity (ρ) values obtained from Hall measurement are given in table 5.4.

Table 5.4. Carrier type, carrier concentration, mobility and resistivity of CIGSe films obtained by selenization of $Cu(In_{0.7},Ga_{0.3})Se_{0.5}$ and $Cu_{0.85}(In_{0.7},Ga_{0.3})Se_{0.5}$ films.

CIGSe film obtained by selenization of	**Carrier Type**	**Carrier concentration (p) (cm^{-3})**	**Mobility (μ) (cm^2/Vs)**	**Resistivity (ρ) (Ωcm)**
$Cu(In_{0.7},Ga_{0.3})Se_{0.5}$	P	1.99×10^{21}	0.0235	0.1327
$Cu_{0.85}(In_{0.7},Ga_{0.3})Se_{0.5}$	P	1.36×10^{19}	0.4267	1.0692

Both the CIGSe films show p-type conductivity. It is found that carrier concentration decreases 2 order of magnitude while resistivity of film increases 1 order of magnitude with decreasing Cu/(In+Ga) from 1 to 0.85. As discussed in Chapter 4, section 4.4.3, the composition of CIGSe has a major role in deciding the electrical properties of the film. From the EDAX data given in table 5.3, the film obtained from $Cu(In_{0.7},Ga_{0.3})Se_{0.5}$ particle has Se/(Cu+In+Ga) = 0.87 and Cu/(In+Ga) =1.22 Similarly, CIGSe film obtained from $Cu_{0.85}(In_{0.7},Ga_{0.3})Se_{0.5}$ particle has Se/(Cu+In+Ga) = 1.02 and Cu/(In+Ga) =0.86. According to the observation made by Noufi et.al, if Se/(Cu+In) is lesser than 1 and Cu/In is greater than 1, the film exhibits p-type conductivity with low resistivity, and if Se/(Cu+In) is greater than 1 and Cu/In is lesser than 1, the film exhibits p-type conductivity with intermediate resistivity [5.22]. Hence, $Cu(In_{0.7},Ga_{0.3})Se_{0.5}$ particles -based film can have p-type conductivity with low resistivity and $Cu_{0.85}(In_{0.7},Ga_{0.3})Se_{0.5}$ particle-based film has p-type conductivity with intermediate resistivity. The observed increase in carrier concentration and decrease in resistivity can also be attributed to the presence of $Cu_{2-x}Se$ phase in the Cu-rich

CIGSe film which is evident from the XRD and Raman analyses. $Cu_{2-x}Se$ is a highly conductive p- type material. It can produce large number of holes and thus decreases the resistivity of film. It should be noted that Cu- rich films with high carrier concentration cannot be used for device application [5.23].

Comparing the CIGSe films obtained from $Cu(In_{0.7},Ga_{0.3})Se_2$ particles, the hole concentration and mobility is increased while resistivity is decreased for the film obtained from $Cu_{0.85}(In_{0.7},Ga_{0.3})Se_{0.5}$ particles. The increase in carrier concentration can be due to the enhancement in grain size as observed from the FESEM images [5.24]. However, the carrier concentration of 10^{19} is little higher than the optimum value needed for good photovoltaic performance. It indicates the presence of defects, probably due to excess of Se (Se/(Cu+In+Ga)>1) and vacancy of Cu (Cu/(In+Ga)<1) that add to the carrier concentration of the CIGSe film [5.22,5.24]. The observed increase in mobility could be due to increasing crystallite size as observed from XRD, RAMAN and FESEM analyses. The increase in crystallite size reduces the grain boundary density and thus the grain boundary barrier. Hence the mobility of charge carrier increases [5.24, 5.25]. However, as mentioned in Chapter 2, table 2.1, the mobility is lesser than the reported values. The inhomogeneous size distribution of grains and voids in the film can be the reason for lower value of mobility.

Photoresponse behavior of CIGSe films obtained by selenization of $Cu(In_{0.7},Ga_{0.3})Se_{0.5}$ and $Cu_{0.85}(In_{0.7},Ga_{0.3})Se_{0.5}$ precursor films is studied by depositing Au contact over the films as noted in Chapter 3 and Chapter 4, and the I-V characteristics are shown in the figure 5.12. The average thickness of the CIGSe films obtained by selenization of $Cu(In_{0.7},Ga_{0.3})Se_{0.5}$ and $Cu_{0.85}(In_{0.7},Ga_{0.3})Se_{0.5}$ films are 9.4 µm and 7.1 µm respectively.

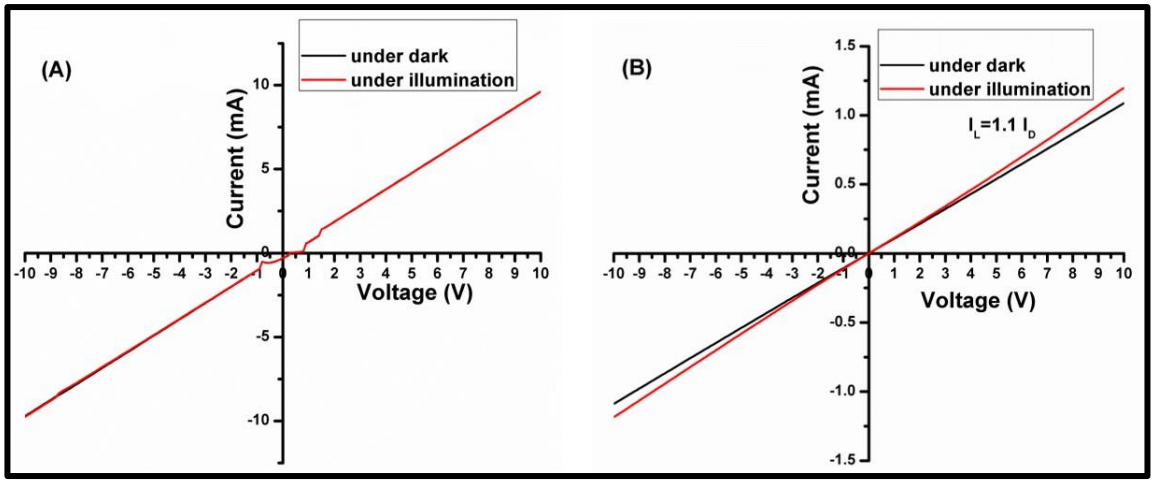

Fig.5.12. Dark and light I-V characteristics of CIGSe films obtained after selenization of (a) $Cu(In_{0.7},Ga_{0.3})Se_{0.5}$ and (b) $Cu_{0.85}(In_{0.7},Ga_{0.3})Se_{0.5}$ films.

Both the films exhibited nearly linear current-voltage curve that is symmetric about the origin. Current increases with voltage indicating ohmic nature of the contacts. CIGSe films obtained by selenization of $Cu(In_{0.7},Ga_{0.3})Se_{0.5}$ precursor film does not show enhancement in conductivity under illumination. While, an enhancement in conductivity under illumination is observed from CIGSe films obtained by selenization of $Cu_{0.85}(In_{0.7},Ga_{0.3})Se_{0.5}$ precursor film. Lack of enhancement of photoconductivity shown by CIGSe films obtained by selenization of $Cu(In_{0.7},Ga_{0.3})Se_{0.5}$ precursor film is related to its high carrier density. Since the hole density is high (close to metallic), the generation of carriers under illumination is not significant to provide an increment in the photoconductivity of the film.

The resistivity of films is calculated from the I-V curve showed in the figure 5.12 (A) and (B). The films showed in figure 5.12 (A) has a resistivity of 0.550 Ωcm under dark and illumination which is in match with the value obtained from the Hall measurements. The resistivity of the film does not change under illumination due to its metallic nature arising from the high carrier concentration. The calculated values of resistivity for the film presented in figure 5.12 (B) are 3.29 and 3.01 Ωcm under dark and illumination, respectively. These values are in the order of resistivity obtained from the Hall measurements (table 5.4).

5.3. Summary

- ✓ $Cu(In_{0.7},Ga_{0.3})Se_y$ powder with y=2,1.5,1 and 0.5 has been prepared by mechanochemical synthesis with BPR of 25:1 and milling speed of 400 rpm for a milling time of 2 h. From XRD analysis, it is found that decreasing Se content leads to the presence of secondary phases. The number of secondary phases increases with reducing Se content. $Cu(In_{0.7},Ga_{0.3})Se_y$ powder with the lowest selenium (y=0.5) consists of maximum secondary phases. EDAX analysis confirms the increase in Cu/Se ratio in proportion with reducing Se content. Morphology of $Cu(In_{0.7},Ga_{0.3})Se_y$ powder changes with reducing Se content. $Cu(In_{0.7},Ga_{0.3})Se_y$ powder with y=2 consists of smaller particles with well-refined microstructure and equiaxed morphology. While, $Cu(In_{0.7},Ga_{0.3})Se_y$ powder with y=0.5 exhibits welded, flattened lamellar structure.
- ✓ $Cu(In_{0.7},Ga_{0.3})Se_y$ particle- based ink is formulated and $Cu(In_{0.7},Ga_{0.3})Se_y$ films are deposited on glass substrate. As-deposited films are annealed at 300 $^{\circ}$C in the air and selenized in two steps. The structural properties of selenized films are studied using XRD and RAMAN analyses. Regardless of the secondary phases in the precursor films, the selenized film exhibits chalcopyrite $Cu(In_{0.7},Ga_{0.3})Se_2$ phase. XRD peak position in the selenized $Cu(In_{0.7},Ga_{0.3})Se_2$ film shift to lower 2θ value with a decrease in Se content in the precursor film. As the Se content lowers, higher is the Ga gradient presented in the selenized film. It is confirmed by the gradual increase in asymmetry in peak shape for selenized CIGSe film. However, CIGSe films obtained from $Cu(In_{0.7},Ga_{0.3})Se_{1.5,}$ $Cu(In_{0.7},Ga_{0.3})Se_1$ and $Cu(In_{0.7},Ga_{0.3})Se_{0.5}$ films consist of $Cu_{2-x}Se$ phase, which is further confirmed by Raman analysis. Moreover, an increase in grain size and crystalline quality of the film with reducing Se content in the precursor particle is observed from the Raman analysis. The composition of selenized films are studied by EDAX analysis and confirms the incorporation of Se content to the $Cu(In_{0.7},Ga_{0.3})Se_y$ film during selenization. FESEM analysis of the selenized $Cu(In_{0.7},Ga_{0.3})Se_y$ films shows that microstructure of selenized film strongly depends on the Se content in the precursor material. CIGSe film obtained from $Cu(In_{0.7},Ga_{0.3})Se_{0.5}$ particle exhibits pronounced recrystallization and grain growth, which is attributed to CuSe liquid phase assisted process.

- ✓ Further, $Cu_{0.85}(In_{0.7},Ga_{0.3})Se_{0.5}$ particles have been synthesized by mechanochemical process and $Cu_{0.85}(In_{0.7},Ga_{0.3})Se_{0.5}$ film is deposited on glass substrate. The as-deposited $Cu_{0.85}(In_{0.7},Ga_{0.3})Se_{0.5}$ film is annealed in air at 300 ˚C for 1 h and then selenized. The physical properties of CIGSe films obtained by selenization of $Cu_{0.85}(In_{0.7},Ga_{0.3})Se_{0.5}$ and $Cu(In_{0.7},Ga_{0.3})Se_{0.5}$ films have been compared. XRD and Raman analysis shows that $Cu_{2-x}Se$ phase is absent in the $Cu_{0.85}(In_{0.7},Ga_{0.3})Se_2$ films. Also, the existence of Ga gradient is reduced. Both $Cu_{0.85}(In_{0.7},Ga_{0.3})Se_2$ and $Cu(In_{0.7},Ga_{0.3})Se_2$ films exhibit recrystallization and grain growth with later exhibits better grain growth than former. $Cu_{0.85}(In_{0.7},Ga_{0.3})Se_2$ film consists of both larger grains and smaller grains. Both films show rough surface morphology with pores on the surface. EDAX analysis confirmed the copper- poor composition of $Cu_{0.85}(In_{0.7},Ga_{0.3})Se_2$ film.
- ✓ Hall effect studies have been carried out for $Cu_{0.85}(In_{0.7},Ga_{0.3})Se_2$ and $Cu(In_{0.7},Ga_{0.3})Se_2$ films and reveals the p- type conductivity of both films. The carrier concentration of $Cu(In_{0.7},Ga_{0.3})Se_2$ film is in the order of 10^{21} due to the presence of $Cu_{2-x}Se$ phase. While carrier concentration of $Cu_{0.85}(In_{0.7},Ga_{0.3})Se_2$ films found to be in the order of 10^{19}. Also, $Cu_{0.85}(In_{0.7},Ga_{0.3})Se_2$ film shows improved electrical properties than the $Cu(In_{0.7},Ga_{0.3})Se_2$ films obtained from $Cu(In_{0.7},Ga_{0.3})Se_2$ particles which are attributed to the increased grain size and better crystallinity.
- ✓ CIGSe films obtained from $Cu(In_{0.7},Ga_{0.3})Se_{0.5}$ particles do not show photoconductivity due to high carrier concentration. Whilst $Cu_{0.85}(In_{0.7},Ga_{0.3})Se_2$ films shows photoconductivity with current, I_L=1.1 I_D. It favors the use of $Cu_{0.85}(In_{0.7},Ga_{0.3})Se_2$ films for photovoltaic applications.

References

5.1. T.J. Anderson, O.D. Crisalle, S.S. Li, P.H. Holloway, “Future CIS manufacturing technology development”, NREL Report, 8 July 1998-17 October 2001.

5.2. K.C. Mills, “Thermodynamic Data for Inorganic Sulphides, Selenides and Tellurides”, Butterworth, London, 1974.

5.3. A. S. Abbasov, K. N. Mamedov, P. G. Rustamov, and P. K. Babaeva, “EMF study of the thermodynamic properties of gallium selenide Ga2Se3”, Chemical bonds in solids 3 (1972) 188-190.

5.4. H. Okamoto, “In-Se (Indium-Selenium)”, Journal of Phase Equilibria and Diffusion 25 (2004) 201-201.

5.5. S. Hiromichi, M. Ryoichi, “Phase study on binary system Ga-Se”, Japanese Journal of Applied Physics 13 (1974) 417-423.

5.6. D.J. Chakrabarti, D.E. Aughlin, “The Cu-Se (Copper-Selenium) system”, Bulletin of Alloy phase Diagrams 2 (1981) 305-315.

5.7. P.R. Subramanian, D.E. Laughlin, “The Cu-In (Copper-Indium) system”, Bulletin of Alloy phase Diagrams 10 (1989) 554-568.

5.8. J.B. Fogagnolo, F. Velasco, M.H. Robert, J.M. Torralba, “Effect of mechanical alloying on the morphology, microstructure and properties of aluminium matrix composite powders”, Material Science and Engineering A 342 (2003) 131-143.

5.9. B.J.M. Aikin, T.H. Courtney, “The kinetics of composite particle formation during mechanical alloying”, Metallurgical Transactions A, 24A (1993) 647-657.

5.10. T. Walter, H.W. Schock, “Crystal growth and diffusion in Cu(In,Ga)Se_2 chalcopyrite thin films”, Thin Solid Films 224 (1993) 74-81.

5.11. S. Nishiwaki, T. Satoh, Y. Hashimoto, T. Negami, T. Wada, “Preparation of Cu(In,Ga)Se_2 thin films at low substrate temperatures”, Journal of Material Research 16 (2001) 394-399.

5.12. A. Neisser, J. Alvarez-Garcia, L. Calvo Barrio, R. Klenk, T.W. Matthes, I. Luck ,“Cu(In,Ga)Se_2 phase formation from metallic Cu-In-Ga precursor stacks in rapid thermal processes”, Material Research Society Symposium Proceedings 668 (2001) H13.1-H13.6.

5.13. R. Kaigawa, K. Ban, S. Merdes, T. Dittrich, R. Klenk, “In and Ga diffusion in Cu(In,Ga)Se_2 and Cu(In,Ga)S_2 films instantaneously prepared in a non-vacuum process”, Energy Procedia 10 (2011) 297-302.

5.14. C.M. Xu, X.L. Xu, J. Xu, X.J. Yang, J. Zuo, N. Kong, W.H. Huang, H.T. Liu, “Composition dependence of the Raman A1 mode and additional mode in tetragonal Cu-In-Se thin films”, Semiconductor Science and Technology 19 (2004) 1201-1206.

5.15. A. Bhatia, H. Meadows, A. Crossay, P.J. Dale, M.A. Scarpulla, “Continuous wave solid phase laser annealing of single-pot electrodeposited $CuInSe_2$ thin films: Effects of Cu/In stoichiometry”, Journal of Applied Physics 114 (2013) 044904-1-044904-8.

5.16. A.E. Zaghi, M. Buffiere, J. Koo, G. Brammertz, M. Batuk, C. Verbist, J. Hadermann, W. K. Kim, M. Meuris, J. Poortmans, J. Vleugels, “Effect of selenium content of $CuInSe_x$ alloy nanopowder precursors on recrystallization of printed $CuInSe_2$ absorber layers during selenization heat treatment”, Thin Solid Films 582 (2015) 11-17.

5.17. H. Dong, A. Quintilla, M. Cemernjak, R. Popescu, D. Gerthsen, E. Ahlswede, C. Feldmann, “Colloidally stable selenium @copper selenide core @shell nanoparticles as selenium source for manufacturing of copper-indium-selenide solar cells”, Journal of Colloidal Interface Science 415 (2014) 103-110.

5.18. B. Walker, R. Agarwal, “Grain growth enhancement of selenide CIGSe nanoparticles to densified films using copper selenides”, 38th IEEE Photovoltaic Specialists Conference, IEEE (2012) 002654-002657.

5.19. M. Batuk, M. Buffiere, A.E. Zaghi, N. Lenaers, C. Verbist, S. Khelifi, J. Vleugels, M. Meuris, J. Hadermann, “Effect of the burn-out step on the microstructure of the solution-processed $Cu(In,Ga)Se_2$ solar cells”, Thin Solid Films 583 (2015) 142-150.

5.20. D. Lee, J.Y. Yang, Y.S. Kim, C.B. Mo, S. Park, B.J. Kim, D. Kim, J. Nam, Y. Kang, “Effects of the Cu/In+Ga ratio on the bulk and interface properties of $Cu(InGa)(SSe)_2$ solar cells”, Solar Energy Materials and Solar Cells 149 (2016) 195-203.

5.21. B.J. Babu, S. Velumani, A. Kassiba, R. Asomoza, J.A. Chavez-Carvayar, “Deposition and characterization of graded $Cu(In_{1-x}Ga_x)Se_2$ thin films by spray pyrolysis”, Material Chemistry and Physics 162 (2015) 59-68.

5.22. R. Noufi, R. Axton, C. Herrington, S.K. Deb, Electronic properties versus composition of thin films of $CuInSe_2$, Applied Physics letters 45 (1984) 668-670.

5.23. J. Liu, D.M. Zhuang, M.J. Cao, C.Y. Wang, M. Xie, X.L. Li, “Preparation and characterization of Cu(In,Ga)Se_2 thin films by selenization of $Cu_{0.8}Ga_{0.2}$ and In_2Se_3 precursor films”, International Journal of Photoenergy 2012 (2012) 1-7.

5.24. M.G. Tsai, H.T. Tung, I.G. Chen, C.C. Chen, Y.F. Wu, “Annealing effect on the properties of Cu($In_{0.7}$,$Ga_{0.3}$)Se_2 thin films grown by femtosecond pulsed laser deposition”,Journal of American Ceramic Society 96 (2013) 2419-2423.

5.25. Z. Seboui, A. Gassoumi, Y. Cuminal, N.K. Turki, “The post-growth effect on the properties of Cu_2ZnSnS_4 thin films”, Journal of Renewable and Sustainable Energy 7 (2015) 011203-1- 011203-10.

CHAPTER- 6

PROPERTIES OF Cu(In,Ga)Se_2/CdS HETEROJUNCTION

Cu(In,Ga)Se_2/CdS (CIGSe/CdS) heterojunction is fabricated as described in chapter 3 to test its performance in the heterostructure. Typical CIGSe solar cells consists of ZnO/Al: ZnO film over the CdS layer. ZnO/Al: ZnO acts as a heterojunction partner and as a window layer. In this work, we limit the CIGSe solar cell structure to Mo/CIGSe/CdS/Au. The aim of this work is to test whether diode formation has taken place between CIGSe and CdS films. The preliminary results on the I-V characteristics and morphology of the heterostructure are presented here.

6.1. Properties of Mo/CIGSe/CdS/Au heterojunction

The I-V characteristics of CIGSe/ CdS heterojunction under dark and illumination is presented in figure 6.1 and shows rectified curve. It indicates the diode formation between CIGSe and CdS interface. However, the I-V curve under illumination passes through zero, denoting no current is extracted from this structure. It should be noted here that the fabricated heterostructure is not a complete solar cell to expect photocurrent.

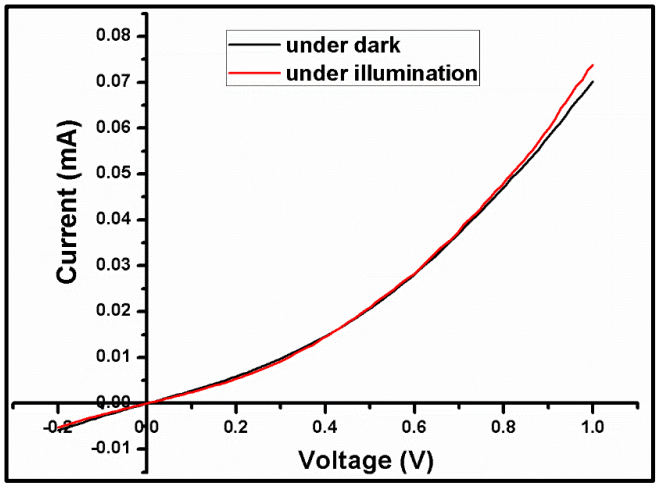

Fig.6.1. The I-V characteristics of CIGSe/CdS heterostructure under dark and illumination.

Considering the high voltage region in the I-V curve given in figure 6.1, the slope of the curve is found to be decreasing. It indicates high series resistance (Rs) present in the fabricated cell structure (Figure 3.22). Also, a small leakage current is observed showing low shunt resistance of the fabricated heterostructure (Figure 3.22). Series resistance is estimated to be 9.419 K Ω which is very high compared to Rs of high-efficiency solar cells. According to Repins et.al [6.1], the series resistance of highly efficient CIGSe solar cell is in the order of 0.25-1 Ω. A good photovoltaic device should have series resistance as low as possible since high value of series resistance reduces the I_{sc}. Photovoltaic device with high series resistance will act as a resistor [6.2].

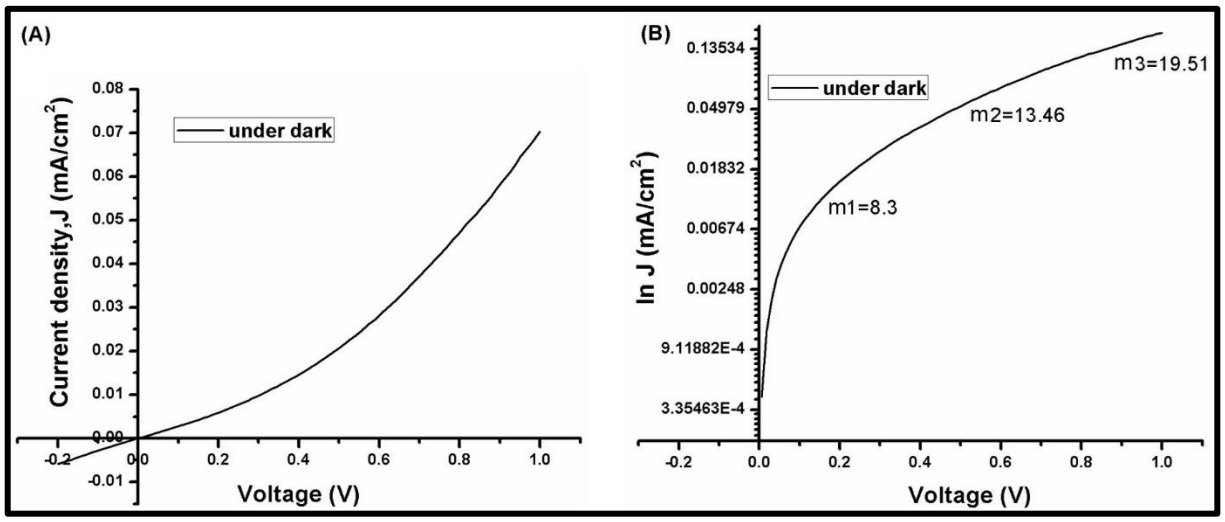

Fig.6.2. (A) The J-V and (B) semi ln J-V characteristics of CIGSe/CdS heterostructure under dark.

The J-V and semi ln J-V characteristics with calculated ideality factor of the fabricated heterostructure under dark are given in figure 6.2 (A) and (B). As discussed in Chapter 3, Ideality factor, m, defines how closely the diode follows ideal diode equation. Theoretically, m >2 indicates tunnelling mechanism occurring in the heterostructure and poor quality of the formed heterojunction [6.3].

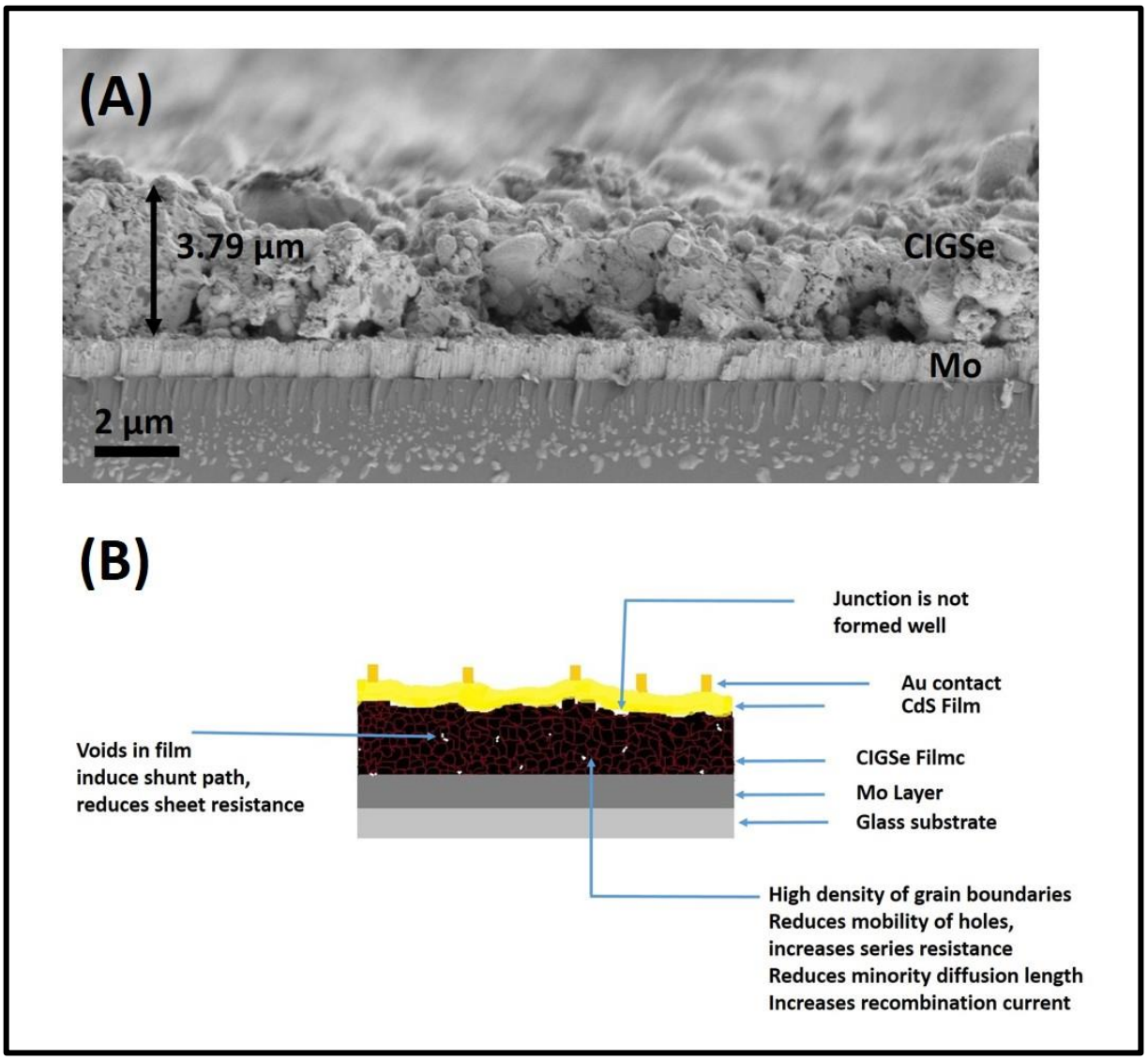

Fig.6.3. (A) Cross-sectional FESEM image of CIGSe/CdS heterostructure and (B) Schematic representation of possible factors effecting the photovoltaic performance of CIGSe/CdS heterostructure.

The cross-sectional FESEM image of the fabricated heterojunction in shown in figure 6.3.(A). CIGSe film contains voids and has rough surface morphology. Hence, the band diagram of the CIGSe-CdS interface will not be flat as that of an ideal CIGSe-based photovoltaic device (figure 3.7).

The possible factors that lead to high series resistance, poor junction qualities and performance of Mo/CIGSe/CdS/Au heterostructure are described below based on the

FESEM image and the schematic diagram of the heterostructure. (figure 6.3 (A) and (B)).

(i) The CIGSe layer consists of a large number of smaller particles. Each particle contains several grains. Hence the density of grain boundaries in the CIGSe is very high. Grain boundary may contain defects such as dislocations, interstitials, vacancies, distorted bond angles and bond distances. Also, the impurity atoms that contaminate the CIGSe film during deposition process will tend to concentrate on the grain boundaries. These defects may have energies within band gap thus, introduce extra electronic states (intra bandgap state) and tend to trap carriers depending on their energetic position relative to band position. Shallow defect close to conduction band tend to act as acceptors and trap electrons, and defect level close to valance band tend to act as donors and trap holes. Defect levels with energy at the centre of the bandgap (deep level defect) may trap either electrons or holes. Deep level defects act as recombination centres. In the case of CIGSe, a p-type material, the shallow defect levels, close to the valance band traps the holes (majority carriers) and give rise to a fixed plane of positive charge at the interface. A negatively charged depletion region forms around the positively charged grain boundary. Because of this, a potential barrier develops which opposes further migration of majority carriers. During the charge transport, when current flows across the grain boundary, the mobility of majority carrier will be slowed down by the potential barrier. While the potential well lead the minority carriers to the recombination centres at the grain boundary and there by reduces minority carrier diffusion length and life-time. The influence of grain boundaries in decreasing the majority carrier mobility may increase the series resistance of the heterostructure [6.4,6.5].

(ii) The reduced minority carrier diffusion length due to smaller grain size increases the recombination of minority carriers at the grain boundaries. It increases dark current [6.4,6.5]. Thus, in the fabricated CIGSe/CdS heterostructure of the present study, there is a high probability for the recombination of photogenerated electrons at the grain boundaries. A

similar result is reported by Vidhya [6.6]. According to Seto [6.7], charge transport in this type of film is mainly due to thermionic emission over grain boundaries. Under illumination, excess carriers will be generating in the CIGSe film. The photo-generated electrons may get trapped in the positively charged grain boundaries and neutralize them resulting in the reduction of barrier height and increasing photoconductivity. In the present study, an increase in photoconductivity is not observed which could be either because the generated electrons are not enough to neutralize the grain boundary barrier or series resistance offered by the structure is such that photogenerated charge collection is not taking place at the junction.

(iii) From the figure 6.3, it is seen that the CIGSe film has rough and irregular surface. The presence of structural defects at the top surface can act as a potential barrier thereby lead to a potential drop across this layer [6.8]. Also, the rough CIGSe top surface prevents the formation of a good heterojunction during the deposition of CdS by CBD process. It lowers the quality of CIGSe/CdS heterojunction thereby width of the space-charge region.

(iv) Figure 6.3 shows voids present in the CIGSe film. The voids act as shunt paths and reduces the shunt resistance of the heterostructure as reported by Jagadheesh [6.9]. Shunt resistance of heterostructure can also get affected by the orientation of grains as suggested by Das et.al [6.10]. Panthani et al [6.10] assigned the low shunt resistance observed in the cell to cracks and voids in the CISe film and to the CdS penetrated to the CISe during chemical bath deposition which could also be expected for the CIGSe/CdS heterostructure in this study.

(v) The difference in the electron affinity and bandgap of CIGSe and CdS materials results in a spike at the conduction band edge as mentioned in chapter 3. It opposes the collection of photogenerated carriers. This triangular barrier contributes to the recombination current by tunnelling of electrons to the interface defects in the CdS layer (figure 6.4). It results in

diode ideality factor greater than 2 in the dark J-V characteristics [6.4,6.12]. Hassant et.al [6.13] reported a CISe solar cell with weak output under illumination and a straight-line I-V characteristic which is assigned to a narrow space-charge region, thus a high band to band tunnelling probability. This could also be expected in the fabricated heterostructure in this study.

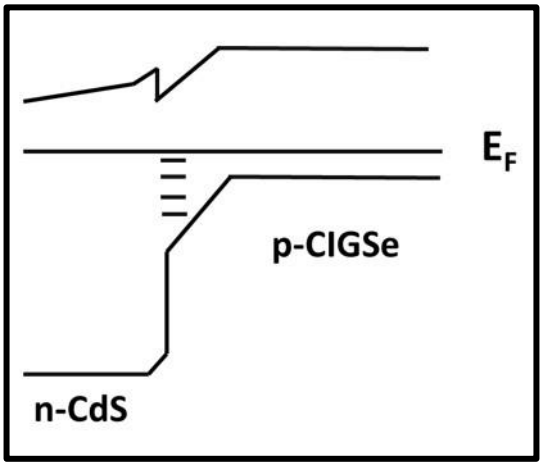

Fig.6.4. Band profile of CIGSe/CdS heterojunction [6.4].

It should be noted here that the formed heterojunction is not a complete solar cell. As described in Chapter 3, a standard CIGSe solar cell uses i-ZnO/Al: ZnO films over CdS. i-ZnO/Al: ZnO layer acts as a front contact and has a significant role in the transport of photogenerated current to the external circuit without too much resistive loss. Also, narrow aligned Ni-Al metal grids are used on the top of i-ZnO/Al: ZnO to reduce resistive losses [6.14]. Since CdS is highly resistive and the fabricated heterojunction employed in this study lacks i-ZnO/Al: ZnO layer, it can be another reason for high series resistance.

More studies should be carried out in the future to understand the role and type of defects present in the CIGSe films as well as the charge transport mechanism taking place in the CIGSe/CdS heterostructure.

6.2. Summary

The fabricated CIGSe/CdS heterojunction structure using CIGSe film obtained after selenization of $Cu_{0.85}(In_{0.7},Ga_{0.3})Se_{0.5}$ films showed characteristics of a rectifier under

dark. The structure showed high series resistance (9.419 KΩ) which is attributed to the high density of grain boundaries and lack of conductive front contact in this structure. Low shunt resistance of the heterostructure is evidenced by the presence of small leakage current. The voids present in the film, orientation of grains and the CdS penetrated to CIGSe film could be the origin of low shunt resistance.

References:

6.1. I. Repins, M.A. Contreras, B. Egaas, C. Dehart, J. Scharf, C.L. Perkins, B. To, R. Noufi, “19.9 % efficient ZnO/CdS/CIGSe solar cell with 81.2% fill factor”, Progress in Photovoltaics: Research and Applications 16 (2008) 235-239.

6.2. R. Singh, B. Bora, K. Yadav, O.S. Sastry, “Effect of series resistance on degradation of Isc, power output and fill factor of HIT technology”, 42nd Photovoltaic Specialist Conference (PVSC) (2015) 1-5.

6.3. A.G. Milnes, D.L. Feucht, “Heterojunctions and metal-semiconductor junctions”, Academic Press, Inc.: (1972)

6.4. J. Nelson, “The Physics of solar cells”, Imperial college press: (2003).

6.5. H. Azimi, Y. Hou, C.J. Brabec, “Towards low-cost, environmentally friendly printed chalcopyrite and kesterite solar cells”, Energy and Environmental Science 7 (2014) 1829-1849.

6.6. B. Vidhya, “Preparation and characterization of nanostructured $CuInGaSe_2$ and CdZnS thin films for photovoltaic applications” Dissertation, CINVESTAV (2010).

6.7. J.Y.W. Seto, “The electrical properties of polycrystalline Silicon films”, Journal of Applied Physics 46 (1975) 5247-5254.

6.8. Q. Cao, O. Gunawan, M. Copel, K.B. Reuter, S.J. Chey, V.R. Deline, D.B. Mitzi, “Defects in $Cu(In,Ga)Se_2$ chalcopyrite semiconductors : A comparative study of material properties,defect states and photovoltaic performance”, Advanced Energy Materials 1 (2011) 845-853.

6.9. J.B. Babu, “Deposition and characterization of TCO’s (AZO and ITO),i-ZnO and graded CIGS structure thin films for photovoltaic application using spray pyrolysis”, Dissertation (2012),CINVESTAV, Mexico.

6.10. V.D. Das, L. Damodare, “A study of band-bending and barrier height variation thin film n-$CdSe_{0.5}Te_{0.5}$ photoanode/polysulphide junctions”, Solid State Communications 99 (1996) 723-728.

6.11. M.G. Panthani, V. Akhavan, B. Goodfellow, J.P. Schmidtke, L. Dunn, A. Dodabalapur, P.F. Barbara, B.A. Korgel, “Synthesis of $CuInS_2$, $CuInSe_2$, and $Cu(In_xGa_{1-x})Se_2$ (CIGS) nanocrystal “inks” for printable photovoltaics”, Journal of American Chemical Society 130 (2008) 16770-16777.

6.12. U. Rau, H.W. Schock, “Cu(In,Ga)Se_2 solae cells” In Clean electricity from photovoltaics, Imperial collage press,London (2001).

6.13. G.E. Hassan, M.R.I. Ramadan, H. El-Labani, M.H. Badawi, S.A. Enein, R. Hill, “The performance of $CuInSe_2$/CdS solar cell fabricated by the sandwich structure technique”, Semiconductor Science and Technology 9 (1994) 1261-1264.

6.14. U.P. Singh, S.P. Patra, “Progress in polycrystalline thin film Cu(In,Ga)Se_2 solar cells”,International Journal of Photoenergy 2010 (2010) 1-19.

CHAPTER – 7
CONCLUSIONS

- This thesis is an effort towards optimization of mechanochemical synthesis process to synthesize single phase CIGSe particles for deposition of films using cost-effective deposition methods. The CIGSe film deposition is performed by doctor blade coating of $Cu(In_{0.7},Ga_{0.3})Se_2$ particle-based ink. Post-deposition heat treatments are provided to improve the physical properties of as-deposited films. $Cu(In_{0.7},Ga_{0.3})Se_2$ films exhibited unique chalcopyrite phase. CIGSe films are also deposited using mechanochemically synthesized $Cu(In_{0.7},Ga_{0.3})Se_y$ (y=1.5,1 and 0.5) as well as $Cu_{0.85}(In_{0.7},Ga_{0.3})Se_{0.5}$ particles-based ink to study the possibility of improvement in structural, morphological and electrical properties. $Cu(In_{0.7},Ga_{0.3})Se_2$ films obtained from heat treatment of $Cu_{0.85}(In_{0.7},Ga_{0.3})Se_{0.5}$ particle-based ink exhibited improved structural, morphological and electrical properties. Representative sample is tested for photovoltaic properties.

- One of the prime objectives of this thesis is mechanochemical synthesis of single phase chalcopyrite CIGSe particles. It is successfully achieved by parametric optimization of mechanochemical process. The properties of synthesized samples are investigated by XRD, FESEM and EDAX analyses to probe variation in structural, morphological and compositional properties with respect to milling parameters. It is found that higher BPR and milling speed promote the formation of single phase $CuIn_{0.5}Ga_{0.5}Se_2$ particles in shorter milling time and single phase $CuIn_{0.5}Ga_{0.5}Se_2$ particle is synthesized within 2 h using BPR of 25:1 and milling speed of 400 rpm. It is also found that $CuIn_{0.5}Ga_{0.5}Se_2$ particle obtained with higher milling speed and BPR are less agglomerated and possess composition close to targeted value.

- The second objective of this thesis is dedicated towards deposition of $Cu(In_{0.7},Ga_{0.3})Se_2$ film using mechanochemically synthesized $Cu(In_{0.7},Ga_{0.3})Se_2$ particles which is achieved successfully and physical

properties of films are investigated. The as-deposited $Cu(In_{0.7},Ga_{0.3})Se_2$ film retains the structural properties of mechanochemically synthesized $Cu(In_{0.7},Ga_{0.3})Se_2$ powder. The as-deposited films are subjected to heat treatments at 300 and 400 ˚C in ambient atmosphere to remove organic additives and heat treated at 550 ˚C in Se atmosphere (selenization) to achieve grain growth and improve the physical properties. Even though, annealing at 400 ˚C resulted in beneficial for removal of organic additives, it leads to loss of Se from the film and thus, decomposition of chalcopyrite CIGSe phase. While, film annealed at 300 ˚C retains the chalcopyrite phase of $Cu(In_{0.7},Ga_{0.3})Se_2$, removes organic additives and improves the crystalline quality of as-deposited films. Further selenization of films improves structural and compositional properties. Also, after selenization process, carbon content in the films annealed at 300 and 400 ˚C is further reduced to 30.73 and 27.81 at % respectively. Even though selenized films do not show expected grain growth, the film which was annealed at 300 ˚C prior to selenization process exhibit superior structural, morphological and compositional properties and presents carrier concentration of 10^{17} cm^{-3}, hole mobility of 0.0368 cm^2/Vs and resisitivity of 3.06 $\times 10^2$ Ωcm. Also, it shows photoconductivity.

- The third objective of this present work is to obtain grain growth in the film deposited using mechanochemically synthesized particles, which is one of the challanging issues of particle- based film deposition methods . It is achieved by preparing CIGSe film using mechanochemically synthesized $Cu(In_{0.7},Ga_{0.3})Se_y$ particles as precursors. The CIGSe film obtained by selenization of $Cu(In_{0.7},Ga_{0.3})Se_{0.5}$ film displayed enhanced recrystallization and grain growth. However, as a consequence of presence of $Cu_{2-x}Se$ binary phases, the obtained CIGSe film reveals carrier concentration of $1.99\times10^{21}/cm^3$ and does not show photoconductivity. This drawback is prevailed over by reducing atomic proportion of Cu in the precursor $Cu(In_{0.7},Ga_{0.3})Se_{0.5}$ particle to 0.85. The CIGSe film obtained by selenization of $Cu_{0.85}(In_{0.7},Ga_{0.3})Se_{0.5}$ film showed single chalcopyrite phase along with enhanced recrystallization, grain growth, improved electrical properties and photoconductivity. Besides, it proclaimed increase in mobility of charge carriers and decrease in resistivity with respect to CIGSe film obtained by selenization of $Cu(In_{0.7},Ga_{0.3})Se_2$ particle-based film.

- Subsequently,CIGSe films obtained by selenization of $Cu_{0.85}(In_{0.7},Ga_{0.3})Se_{0.5}$ particle-based film is tested for the formation of heterostructure. The CIGSe/CdS heterojunction shows rectifying characteristics under dark and illumination. Further deposition of i-ZnO/Al: ZnO front contact and improvement of quality of CIGSe film is necessary to obtain photovoltaic properties from the fabricated Mo/CIGSe/CdS/Au structure.

Main Contributions:

The present work satisfied all the prime goals of this thesis and contributed to the scientific research and technological field in the following:

I. Scientific Contribution

- The present work identified the role of milling parameters such as milling speed, milling time, and ball to powder ratio on the structural, morphological and compositional properties of mechanochemically synthesised CIGSe particles. The important results were discussed in "Parametric optimization of mechanochemical process for the synthesis of $Cu(In,Ga)Se_2$ nanoparticles, **M. Rohini**, P. Reyes, S. Velumani, M. Latha,Goldie Oza, I. Becerril Juarez, R. Azomosa, Material Science in semiconductor processing , 37(2015)151–158".
- The impact of air-annealing temperature on the the properties of selenized films is noted and must be taken into account for further future study.
- The use of mechanochemically synthesized quaternary $Cu(In,Ga)Se_2$ particle-based ink is the limiting constraint to facilitate grain growth in the CIGSe film.
- The single -phase CIGSe film having improved grain growth,recrystallization and electrical properties is obtained by using $Cu_{0.85}(In,Ga)Se_{0.5}$ particle-based ink, which we believe to be applied for the fabrication of cost-effective CIGSe-based solar cells.

II. Technological Contribution

- The mechanochemical synthesis process was optimised to obtain single phase CIGSe particle within 2 h , for the first time in the SEES,CINVESTAV.

- Influenze of selenization process on the properties of CIGSe film obtianed by particle-based ink was studied for the first time in our group through this work.

Scope for future work

The present work is mainly focused on the optimization of mechanochemical process to synthesize CIGSe particles, deposition of film and investigation of its physical properties with the aim of photovoltaic applications. On the basis of this study, the important issues such as (i) non-uniform size distribution and agglomeration of the CIGSe particles, (ii) presence of pores, and (iii) surface roughness of the film, should be considered carefully in the preparation of CIGSe film for photovoltaic application. The following technical facts could favor the improvement of the film properties.

1. Wet milling of mechanochemically synthesized $Cu_{0.85}(In_{0.7},Ga_{0.3})Se_{0.5}$ particles is adviced to obtain non-agglomerated CIGSe particles with uniform size distribution.
2. Further optimization of selenization process for $Cu_{0.85}(In_{0.7},Ga_{0.3})Se_{0.5}$ particle-based films to acquire CIGSe film with smooth surface morphology.
3. Chemical treatments using Bromine solution, Pottassium permanganate solution etc are recommended for film ethcing to enhance the surface properties.
4. Detailed study of charge transport mechanism in the CIGSe film.
5. Completion of CIGSe solar cell structure with deposition of iZnO-Al: ZnO layer is potentially important to transmit maximum light to the CIGSe absorber layer and to reduce the series resistance of the device.

Publications

a. Peer Reviewed Journals

i. Parametric optimization of mechanochemical process for the synthesis of Cu(In,Ga)Se_2 nanoparticles, **M.Rohini**,P.Reyes,S.Velumani,M.Latha,Goldie Oza,I.Becerril Juarez, R.Azomosa,Material Science in semiconductor processing , 37(2015)151–158.

ii. Synthesis of $CuIn_{1-x}Ga_xSe_2$ Nanoparticles by Thermal Decomposition Method with Tunable Ga Content, M. Latha, R. Aruna Devi, S. Velumani, Goldie Oza, P. Reyes-Figueroa, **M. Rohini**, I. G. Becerril-Juarez, and Junsin Yi, Journal of Nanoscience and Nanotechnology,15 (2015) 8388-8394.

iii. Synthesis and Characterization of Cadmium Sulfide Nanoparticles by Chemical Precipitation Method, R. Aruna Devi, M. Latha, S. Velumani, Goldie Oza, P. Reyes-Figueroa, **M. Rohini**, I. G. Becerril-Juarez, Jae-Hyeong Lee, and Junsin Yi, Journal of Nanoscience and Nanotechnology,15 (2015) 8434-8439.

b. Conference Publications

i. Effect of Milling Time on Mechanically Alloyed Cu(In,Ga)Se_2 Nanoparticles, M.Rohini, P.Reyes,S.Velumani and I.G.Becerril, 2014 11th International Conference on Electrical Engineering, Computing Science and Automatic Control (CCE), 10.1109/ICEEE.2014.6978309.